

FUNDAMENTAL ELECTROCHEMICAL STUDY ON NEODYMIUM MOLTEN
SALT ELECTROLYSIS IN FLUORIDE BATH

by

Fangyu Liu

A thesis submitted to the Faculty and the Board of Trustees of the Colorado School of Mines in partial fulfillment of the requirements for the degree of Doctor of Philosophy (Metallurgical and Materials Engineering).

Golden, Colorado

Date _____

Signed: _____
Fangyu Liu

Signed: _____
Dr. Patrick R. Taylor
Thesis advisor

Golden, Colorado

Date _____

Signed: _____
Dr. Angus Rockett
Professor and Department Head
Metallurgical and Materials Engineering

ABSTRACT

In the recent decades, the clean energy economy has been driving a rapidly increasing demand for rare earth materials with their applications in essential high technologies such as electric vehicles and wind turbines. The technologies for the winning of rare earth metals are developing. As the predominant winning technique, electrolysis of rare earth oxides in molten fluoride systems has been faced with two major problems: one is low energy efficiency and the other is high emissions of perfluorocarbons (PFCs). Therefore, there exists a need for the metallurgy community to address those problems both theoretically and practically, and to develop improved processes for reducing rare earth oxides. This thesis uses the example of neodymium winning to elucidate the fundamental electrochemical properties of the molten fluoride electrolytes and the mechanism of the electrolysis process, and provides a guide to economically win rare earth metals with elevated energy efficiency and decreased emissions for the process.

As for the property investigation, this research carried out measurements to determine the liquidus temperatures of the $\text{NdF}_3\text{-PrF}_3\text{-LiF}$ ternary salt system, the solubilities of Nd_2O_3 in the electrolytes, and the electrical conductivity of the $\text{NdF}_3\text{-LiF}$ salt. A conductance cell system was developed to investigate electrical conductivity and produce reliable data. The experimental results indicate that the electrical conductivities of the molten $\text{NdF}_3\text{-LiF}$ system between 70 wt% to 85 wt% NdF_3 within the range of temperature from 950 °C to 1050 °C range from $4.38 \text{ ohm}^{-1} \text{ cm}^{-1}$ to $6.08 \text{ ohm}^{-1} \text{ cm}^{-1}$. Furthermore, an empirical equation to estimate the value of the electrical conductivity for a specific molten salt is proposed.

A mathematical model regarding the voltage change against current in the molten $\text{Nd}_2\text{O}_3\text{-NdF}_3\text{-LiF}$ electrolysis is proposed based on the thermodynamics and kinetics study and validated

through experiments and literature observations. The model and the experimental results illustrate that the limiting current of the electrolysis cell increases with the increase of anode surface area, higher energy efficiency can be achieved with reduced electrode distance and more effectively, reduce the submerged depth ratio of anode to cathode. An effective technique to prevent the generation of PFCs is to design the cell conditions which allow the limiting current to be smaller than the critical current.

TABLE OF CONTENTS

ABSTRACT	iii
LIST OF FIGURES	x
LIST OF TABLES	xvi
ACKNOWLEDGEMENT	xviii
CHAPTER 1 INTRODUCTION.....	1
1.1 Rare earth elements (REEs)	1
1.1.1 What are REEs?	1
1.1.1 Applications of REEs.....	2
1.1.2 Geographic feature of REEs production	3
1.1.3 Criticality of REEs.....	4
1.2 Oxide-fluoride Molten Salt Electrolysis of Neodymium	5
1.3 Justification of research and research scope	6
1.4 Organization of dissertation	7
CHAPTER 2 FUNDAMENTAL STUDY ON RARE EARTH OXIDE-FLUORIDE MOLTEN SALT ELECTROLYSIS	9
2.1 Introduction	9
2.2 Density of NdF ₃ -LiF melt	9

2.3	Solubility and dissolution of rare earth oxide in the fluoride melt.....	12
2.4	Electrical conductivity of the electrolyte	14
2.5	Confusion on anode effect PFCs generation	18
2.6	Summary	19
CHAPTER 3	INVESTIGATION ON LIQUIDUS TEMPERATURE OF RARE EARTH FLUORIDE ELECTROLYTE AND THE SOLUBILITY OF NEODYMIUM OXIDE	20
3.1	Introduction	20
3.2	Methodology and experimental.....	20
3.2.1	Heat-flux differential scanning calorimetry (HF-DSC).....	20
3.2.2	Inductively coupled plasma mass spectroscopy (ICP-MS)	22
3.2.3	Determination of liquidus temperature of fluoride mixtures	22
3.2.4	Determination of solubilities using DSC	23
3.3	Results and discussion.....	23
3.3.1	Liquidus temperature measurement.....	23
3.3.2	Measurement on the solubility of Nd ₂ O ₃	26
3.4	Conclusion.....	30
CHAPTER 4	ELECTRICAL CONDUCTIVITY MEASUREMENT OF MOLTEN SALT NDF ₃ -LIF ELECTROLYTE	32
4.1	Introduction	32

4.2	Experimental setup.....	33
4.2.1	Conductance cell construction.....	33
4.2.2	EIS test circuit construction.....	41
4.3	Methodology and experimental procedures.....	44
4.4	Results and discussion.....	46
4.4.1	Equivalent circuit development.....	46
4.4.2	Calibration and validation.....	48
4.4.3	NdF ₃ -LiF electrical conductivity measurement results and discussion.....	51
4.5	Conclusion.....	75
CHAPTER 5	MATHEMATICAL MODEL DEVELOPMENT OF ND ₂ O ₃ -NDF ₃ -LiF MOLTEN SALT ELECTROLYSIS SYSTEM.....	77
5.1	Introduction.....	77
5.2	Problem establishment.....	77
5.3	Thermodynamics Considerations.....	80
5.4	Kinetics Considerations.....	89
5.5	Electrolysis Model Establishment.....	95
5.5.1	Voltage drop between the anode and the cathode.....	95
5.5.2	Discussion on ΔV_{ac}	98
5.5.3	Anode effect.....	105
5.5.4	$\Delta V_{ac} - i$ Diagram Development.....	105

5.6	Parameters	108
5.6.1	Operating temperature	108
5.6.2	Solubility of neodymium oxide	108
5.6.3	Density and viscosity	108
5.6.4	Electrical conductivity	109
5.6.5	Dissolution rate of neodymium oxide.....	109
5.6.6	Cell geometry.....	110
5.6.7	Heat Balance	110
5.6.8	PFCs Concentration in Offgas	110
5.7	Conclusion.....	111
CHAPTER 6	MATHEMATICAL MODEL VALIDATION AND ELECTROWINNING OF NEODYMIUM IN THE NDF ₃ -LIF SYSTEM.....	113
6.1	Introduction	113
6.2	Experimental setup.....	113
6.3	Experimental procedures.....	120
6.3.1	Sample preparation	120
6.3.2	Operational procedures	120
6.4	Experimental results and discussion	121
6.4.1	Scoping study for electrolysis tests.....	121
6.4.2	Impact of anode surface area on the electrolysis process	130

6.4.3	Impact of electrode distance on the electrolysis process	149
6.4.4	Electrolysis product characterization.....	156
6.5	Conclusion.....	159
CHAPTER 7 CONCLUSIONS.....		160
7.1	Thesis conclusions.....	160
7.1.1	Conclusions regarding the property study	160
7.1.2	Conclusions regarding the electrolysis process	162
7.2	Contributions to the knowledgebase	165
7.3	Recommendations for future work.....	166
REFERENCES CITED.....		167

LIST OF FIGURES

Figure 1-1 World mine production of rare-earth oxides, by country and year, from 1960 to 2012(Van Gosen, Verplanck et al. 2019).	4
Figure 2-1 Schematic view of density measurement cell used in Hu and coworkers' work	10
Figure 2-2 Density measurement data by Hu et al. (plotted based on the reported data)(Hu, Wang et al. 2010).....	11
Figure 2-3 Solubility of rare earth oxide in fluoride molten salts(Guo, Sun et al. 2016).....	13
Figure 2-4 Nd ₂ O ₃ solubility in fluoride melts with different NdF ₃ -LiF compositions and at different temperatures in Guo, et al' work.....	14
Figure 2-5 Keller's experimental setup to determine electrolyte conductivity(Keller and Larimer 1997)	15
Figure 2-6 Electrical conductivity measurement results by Zheng et al. (ZHENG, ZHU et al. 2013) (plotted based on the graphs in the paper): (83.5-89%)NdF ₃ -(10-12.5%)LiF salt system.....	16
Figure 2-7 Schematic of apparatus for electrical conductivity measurement in Kim's work (Keller and Larimer 1997).....	17
Figure 3-1 Fusion and crystallization temperature for polymeric materials (International 2018)	21
Figure 3-2 DSC results for NdF ₃ -PrF ₃ -LiF (60.5-24.5-15.0 wt%)	24
Figure 3-3 Ternary contour diagram of the liquidus temperature for the NdF ₃ -PrF ₃ -LiF system based on data from this research (red square dots in the diagram) and the reported data by Thoma (NdF ₃ -LiF and PrF ₃ -LiF phase diagrams)	26
Figure 3-4 DSC results for NdF ₃ -LiF (82.6-17.4 wt%) and its mixtures with Nd ₂ O ₃ (1.10, 1.77, 3.39 wt% of total fluoride mass).....	27
Figure 3-5 DSC results for NdF ₃ -PrF ₃ -LiF (36.0-8.7-55.3 wt%) and its mixtures with Nd ₂ O ₃ (1.78, 0.89, 0.66 wt% of total fluoride mass)	28

Figure 3-6 Solubility of Nd_2O_3 in the NdF_3 -LiF (82.6-17.4 wt%) and NdF_3 -PrF ₃ -LiF (36.0-8.7-55.3 wt%) salts (presented in wt% of the total mass of the fluorides)	29
Figure 3-7 Solubility of Nd_2O_3 in the NdF_3 -LiF (82.6-17.4 wt%) and NdF_3 -PrF ₃ -LiF (36.0-8.7-55.3 wt%) salts (presented in respective mole% of the total moles of the fluorides)	30
Figure 4-1 Schematic of conductance cell for electrical conductivity measurement	35
Figure 4-2 Tungsten coil tips of the electrodes for the conductance cell	36
Figure 4-3 Configuration of the cell lid for the conductance cell	37
Figure 4-4 Configuration of the conductance cell lid	38
Figure 4-5 Configuration of the conductance cell underneath the lid for EIS measurements	39
Figure 4-6 Illustration of the design for the change of electrode position for EIS tests	40
Figure 4-7 Conductance cell system for EIS measurement with glovebox	42
Figure 4-8 Conductance cell setup for EIS measurements	43
Figure 4-9 Equivalent circuit of the conductance cell: R series represents resistances, C series represents capacitors, and L series represents inductors.	46
Figure 4-10 Bode plot plot and fitted plot with the proposed equivalent circuit: LiF, 950 °C.....	47
Figure 4-11 Nyquist plot and fitted plot with the proposed equivalent circuit: LiF, 950 °C.....	48
Figure 4-12 Nyquist plot for calibration with LiF at 960 °C	49
Figure 4-13 The real part for the cell impedance determined when the imaginary part equals zero for LiF at 960 °C	50
Figure 4-14 Nyquist plot for the EIS results of NdF_3 -LiF with increasing interelectrode spacing: $c\text{NdF}_3=85\text{wt}\%$, 975°C	52

Figure 4-15 Linear relationship between $Z_{cell}(Z'' = 0)$ and the relative electrode distance: $cNdF_3=85wt\%$, $975^\circ C$	53
Figure 4-16 Temperature dependence of the specific electrical conductivity of molten fluorides (NdF_3-LiF): 70 wt% NdF_3 , 80 wt% NdF_3 and 85 wt% NdF_3	56
Figure 4-17 Relative deviations for calculated data by Equation (4.5) compared to the measured data	58
Figure 4-18 3D plot for the specific electrical conductivity of the NdF_3-LiF salt system with Equation (4.6)	59
Figure 4-19 Relative deviations for calculated data by Equation (4.6) compared to the measured data	60
Figure 4-20 Arrhenius form analysis for specific electrical conductivity of the NdF_3-LiF system: 70 wt% NdF_3 , 80 wt% NdF_3 and 85 wt% NdF_3	61
Figure 4-21 Relative deviations for calculated data by Equation (4.7) compared to the measured data	62
Figure 4-22 Molar electrical conductivity of NdF_3-LiF salts as a function of temperature: 70 wt% NdF_3 , 80 wt% NdF_3 and 85 wt% NdF_3	64
Figure 4-23 Arrhenius form analysis for the molar electrical conductivity of NdF_3-LiF salts: 70 wt% NdF_3 , 80 wt% NdF_3 and 85 wt% NdF_3	65
Figure 4-24 Analysis on the relationship between the molar electrical conductivity and the charge density for NdF_3-LiF salts: 70 wt% NdF_3 , 80 wt% NdF_3 and 85 wt% NdF_3 . 67	
Figure 4-25 Changes of coefficients α and β from Equation (4.11) with the increase of NdF_3 content in the NdF_3-LiF salt	70
Figure 4-26 Relative deviations for calculated data by Equation (4.6) compared to the measured data	71
Figure 4-27 Coefficient $\ln \kappa u$ changes with increasing molar masses for $NaCl$, KCl , $RbCl$ and $CsCl$	73
Figure 4-28 Coefficient β changes with increasing molar masses for $NaCl$, KCl , $RbCl$ and $CsCl$	74

Figure 5-1 Electrolytic process for the neodymium production in the molten fluoride electrolyte	78
Figure 5-2 Gibbs free energy minimization by HSC Chemistry 8.0	82
Figure 5-3 CO(g) percentage at equilibrium for the Boudouard Equation in the gas product	83
Figure 5-4 Thermodynamic calculation on the critical activity of NdF ₃ for Reaction (5.3) to take over at different Nd ₂ O ₃ activity level.....	86
Figure 5-5 Schematic of inter-electrode voltage drop (ΔVac) against current (i) in the Nd ₂ O ₃ -NdF ₃ -LiF electro-reduction system	106
Figure 6-1 Schematic of the electrolytic cell setup.....	114
Figure 6-2 Electrical circuit schematic for the electrolytic cell	116
Figure 6-3 Configuration of cell lid for electrolysis cell (distance between anode and cathode: 1.5 inches (3.81 cm); electrode diameter: 3/8 inch (0.9525 cm)	117
Figure 6-4 Setup of the electrolysis test system.....	118
Figure 6-5 Photograph of the configuration of the electrolytic cell.....	119
Figure 6-6 Cell voltage curve with increasing current (Exp. 1: two anodes, 2.8 cm submerged depth)	123
Figure 6-7 Cell voltage curve with increasing current (Exp. 2: 2 anodes, 3.8 cm submerged depth)	124
Figure 6-8 Cell voltage curve with increasing current (Exp. 3: 1 anodes, 2.8 cm submerged depth)	125
Figure 6-9 Current-voltage characteristics (Keller and Larimer 1997): Nd ₂ O ₃ fed into the NdF ₃ -CaF ₂ -LiF (60-20-20 wt%) salt for electrolysis, 920 °C	127
Figure 6-10 Analysis for the equilibrium current (Point b) with changing anode surface area..	129
Figure 6-11 The limiting currents for the scoping study electrolysis tests with changing anode surface area	130

Figure 6-12 Cell voltage change with the change of current (Exp. 9 – 15).....	132
Figure 6-13 Cell voltage at varying current density (Exp. 9 – 15)	133
Figure 6-14 Cell voltage with changing current (Exp. 15 vs. Exp. 16)	134
Figure 6-15 Limiting current changes with anode surface area.....	136
Figure 6-16 The comparison of the slopes for each case in the experiments between the calculated results using Equation (6.4) and the experimental results.	139
Figure 6-17 Limiting voltage changes with increasing anode surface area (Electrode distance: $l = l_0$ (3.81 cm))	142
Figure 6-18 Comparison on the limiting current with varying depth ratio of anode to cathode between the experimental results and the calculated results according to Equation (6.11).....	144
Figure 6-19 Comparison on the limiting current density with varying depth ratio of anode to cathode between the experimental results and the calculated results according to Equation (6.12)	145
Figure 6-20 Comparison on the theoretical limiting current energy efficiency with varying depth ratio of anode to cathode between the experimental results and the calculated results according to Equation (6.15) (6.11)	148
Figure 6-21 Limiting voltage changes with increasing anode surface area considering varying electrode distance.....	150
Figure 6-22 Theoretical limiting current energy efficiency changes with increasing anode surface area with varying electrode distance	151
Figure 6-23 Theoretical level-out energy efficiency and theoretical half depth energy efficiency as a function of electrode distance.....	153
Figure 6-24 Cell voltage changes with increasing current: Exp. 17, oxide particle size - 2mm+1mm.....	156
Figure 6-25 SEM image of the metal product from the electrolysis process: 1000X.....	157

Figure 6-26 EDX analysis result of metal product from the electrolysis process 158

Figure 7-1 Compilation of diagrams for the electrolysis process in molten fluoride based on the discussion in this thesis with assumption of thermally self-sustaining cell.
Bottom left: black full-line (with grey dash-lines) - line *abcd* represents the typical response of cell voltage to the change of current (from c_0 to $c_n + 1$, either increasing the maximum dissolution rate of oxide or increasing the maximum mass transfer rate of oxide in the melt); red full-line – the limiting cell voltage as a function of anode surface area, A , (from m_4 to m_0 , fitted in a Boltzmann equation); navy blue dash-lines – the cell voltage change against current with changing anode surface area and fixed electrode distance (from $\Sigma 1m_0$ to $\Sigma 1m_4$, anode surface area decreases linearly related to limiting current); green dash-lines – the cell voltage change against current with changing electrode distance and fixed anode surface area (from $\Sigma 1p_0$ to $\Sigma 1p_3$, the electrode distance decreases).
Top left: the change of the theoretical limiting current energy efficiency, μ_{max} , against the anode surface area, A , regarding various difference electrode distance, l .
Bottom right: the optimal theoretical energy efficiency, μ_{max0} , changes with increasing electrode distance. 163

LIST OF TABLES

Table 1-1 Rare earth elements (REEs) and their applications(Van Gosen, Verplanck et al. 2019)	3
Table 3-1 Comparison of measured data with the literature data by Thoma regarding NdF ₃ -LiF melt system	25
Table 3-2 List of results for liquidus temperatures for NdF ₃ -PrF ₃ -LiF salts by DSC	25
Table 4-1 Measured LiF electrical conductivity compared with the literature data for validation	50
Table 4-2 Investigated compositions and temperature ranges for NdF ₃ -LiF electrolytes	51
Table 4-3 Pertinent parameters for the NdF ₃ -LiF salt system	54
Table 4-4 Electrical conductivities of the NdF ₃ -LiF salts determined in this research	55
Table 4-5 Second order series analysis of the electrical conductivity data for the molten NdF ₃ -LiF system: 70 wt% NdF ₃ , 80 wt% NdF ₃ and 85 wt% NdF ₃	57
Table 4-6 Coefficient values for Equation (4.6) showing the specific electrical conductivity of NdF ₃ -LiF salts as a function of temperature and composition	60
Table 4-7 Coefficients and statistics analysis in Arrhenius form (Equation (4.7)) for the specific electrical conductivity of the NdF ₃ -LiF system: 70 wt% NdF ₃ , 80 wt% NdF ₃ and 85 wt% NdF ₃	62
Table 4-8 Coefficients and statistics analysis in the linear fit (Equation (4.8)) for the molar electrical conductivity of the NdF ₃ -LiF system: 70 wt% NdF ₃ , 80 wt% NdF ₃ and 85 wt% NdF ₃	65
Table 4-9 Coefficients and statistics analysis for Arrhenius form equations (Equation (4.9)) in terms of the molar electrical conductivity of NdF ₃ -LiF salts: 70 wt% NdF ₃ , 80 wt% NdF ₃ and 85 wt% NdF ₃	66
Table 4-10 Coefficients and statistics analysis for the fitted equations (Equation (4.11)): 70 wt% NdF ₃ , 80 wt% NdF ₃ and 85 wt% NdF ₃	68

Table 4-11 Linear analysis for the intercept, α , and the slope, β , for Equation (4.11) with regard to changing molar percentages of NdF_3 in the salt.....	70
Table 4-12 Coefficients for Equation (4.16) for different chemicals using data from (Janz, Janz et al. 1968).....	72
Table 4-13 Coefficient and statistics analysis for $\ln \kappa u$ and β with changing molar masses: NaCl, KCl, RbCl and CsCl.....	74
Table 5-1 Standard Gibbs Free Energies and potentials for Reactions of interest determined by HSC Chemistry 8.0 at 1050°C.....	81
Table 6-1 Experiment conditions for scoping study tests of neodymium electrolysis: 85 wt% NdF_3 , 1050 °C.....	122
Table 6-2 Analysis results for scoping study tests of neodymium electrolysis: 85 wt% NdF_3 , 1050 °C.....	126
Table 6-3 Experiment conditions for anode surface area study tests of neodymium electrolysis: 85% NdF_3 , 1050 °C.....	131
Table 6-4 Analysis results for electrolysis experiments.....	135
Table 6-5 Calculated parameters for electrolysis test results.....	137
Table 6-6 Coefficients for Boltzmann fit analysis as in Figure 6-21.....	154
Table 6-7 Coefficients for Boltzmann fit analysis as in Figure 6-22.....	155

ACKNOWLEDGEMENT

I would like to acknowledge the assistance and guidance I have received throughout my past three years of graduate studies and international experience. First, I would like to express my very great appreciation to Professor/Dr. Patrick R. Taylor, my academic and research advisor, for his invaluable and constructive guidance and advice for my study and project during my past three years of PhD program. He has devoted his time to discussing with me the project and granted me his trust and patience throughout the time. I have benefited tremendously from his philosophy of educating graduate students. Mr. Matthew Earlam has been generous with his knowledge and industrial experience in molten salt electrolysis. I would like to acknowledge to his help and time. Furthermore, many thanks are due to other members of my thesis committee, Professor Sridhar Seetharaman, Professor Corby Anderson, and Professor Roderick Eggert for their guidance and advice.

I would also like to extend my sincere gratitude to the faculty and students of the Kroll Institute for Extractive Metallurgy (KIEM), present and past, for their unparalleled support. My thanks also go out to the faculty, students and staff of the Department of Metallurgical and Materials Engineering and of the Colorado School of Mines for their aid in sundry activities. I have obtained a lot of assistance throughout campus to construct the experiment setups and conduct testwork for my research.

Thanks also to my family and my friends for their continual support during my study and my stay in the United States.

I would like to acknowledge the financial support of the Li Foundation, SME Mineral Processing and Metallurgy Division, and especially the Critical Materials Institute of the U.S. Department of Energy. This work was supported by the Critical Materials Institute, an Energy

Innovation Hub funded by the U.S. Department of Energy, Office of Energy Efficiency and Renewable Energy, Advanced Manufacturing Office.

CHAPTER 1

INTRODUCTION

Rare earth materials have played an essential role in the clean energy economy nowadays due to their widespread applications in high technologies. Apart from the high energy consumption to produce rare earth materials and the associated environmental problems, the increasing demand for those materials and the geographic production dominance have raised awareness globally that it is urgent to improve the technology to extract rare earth elements (REEs) to sustain the clean energy economy. As the last stage of the flowsheet to produce rare earth metals (REMs), the oxide-fluoride molten salt electrolysis is the most commercially available technique to produce rare earth metals. This technology is relatively young in terms of the rare earth metal production and there is a need for the continuous improvement to understand the fundamentals of the process and address the problems along with this technology. This chapter provides an introduction to the background of the rare earth materials and the techniques to extract them. A brief justification of reasons for investigating the fundamental properties for the $\text{NdF}_3\text{-LiF}$ electrolyte system and establishing the mathematical models to understand the electrolytic process. Furthermore, a scope of research for investigating these matters is indicated. This chapter is concluded by providing an overview of the structure of the dissertation.

1.1 Rare earth elements (REEs)

1.1.1 What are REEs?

Rare earth metals constitutes 17 chemical elements on the periodical table, including scandium (Sc), yttrium (Y), and the 15 lanthanides, namely lanthanum (La), cerium (Ce), praseodymium (Pr), neodymium (Nd), promethium (Pm), samarium (Sm), europium (Eu),

gadolinium (Gd), terbium (Tb), dysprosium (Dy), holmium (Ho), erbium (Er), thulium (Tm), Ytterbium (Yb) and lutetium (Lu).

Except for the radioactive promethium, rare earth elements are not considered rare in terms of their abundance in Earth's crust. Take cerium and neodymium as an example. They make the 27th and 28th most abundant chemical elements, respectively, as opposed to nitrogen the 31st. The nature of low concentrations of rare earths in the ore bodies in a variety of forms can be thought of as rare. Because of their extreme affinity with oxygen, they are found commonly existent in nature as oxides, which explains why they have the word "earth" in their name since it is commonly used to refer to oxidic materials in the 19th century. (Goonan 2011, Zepf 2016)

1.1.1 Applications of REEs

Due to their extraordinary magnetic, catalytic and fluorescent properties (Abbasalizadeh, Teng et al. 2016), many of the metals in the group of the rare earth elements have played an essential role as key materials in high technology and clean energy technology in the 21st century. Table 1-1 lists some examples for the applications of the rare earth elements.

The commercial applications (Fernandez 2017, Van Gosen, Verplanck et al. 2019) of these materials are cells phones, computers, fluorescent and light-emitting-diode (LED) lights, flat-screen television, computer monitors, permanent magnets used in the generators of wind turbines, and batteries of hybrid and electric vehicles. Besides, the rare earth elements are found in a variety of defense applications. Some examples are components of jet engines, missile guidance systems, antimissile defense systems, satellites and communication systems (Van Gosen, Verplanck et al. 2019). Rare earth elements enable the possibility for the electronic devices to become more compact, less detrimental to the environment with emission, more efficient to operate and more cost-effectively both in manufacturing and purchasing (Elliott

2018). Furthermore, limited substitutes are found available to replace the rare earth materials with the same effectiveness(USGS 2019).

Table 1-1 Rare earth elements (REEs) and their applications(Van Gosen, Verplanck et al. 2019)

Element	Symbol	Atomic number	Example applications
Light rare earth elements			
Lanthanum	La	57	Optical glass, nickel-metal-hydride batteries
Cerium	Ce	58	Colored glass (flat-panel displays), automobile catalytic converters
Praseodymium	Pr	59	Super-strong magnets, metal alloys, specialty glass, lasers
Neodymium	Nd	60	Permanent magnets
Samarium	Sm	62	Permanent magnets, nuclear reactor control rods, lasers
Europium	Eu	63	Optical fibers, visual displays, lighting
Gadolinium	Gd	64	Shielding in nuclear reactors, X-ray and magnetic resonance imaging scanning systems
Heavy rare earth elements			
Terbium	Tb	65	Visual displays, fuel cells, lighting
Dysprosium	Dy	66	Permanent magnets, lighting
Holmium	Ho	67	Lasers, high-strength magnets, glass coloring
Erbium	Er	68	Glass coloring, fiber optic cables
Thulium	Tm	69	Lasers, portable X-ray machines
Ytterbium	Yb	70	Stainless steel, lasers
Lutetium	Lu	71	Petroleum refining
Yttrium	Y	39	Metal alloys, visual displays, lasers, lighting

1.1.2 Geographic feature of REEs production

Figure 1-1 depicts the historical world mine production of rare earth oxide equivalent by country(Van Gosen, Verplanck et al. 2019). The United States was the world’s largest REE-producing country with the predominance in production from the Mountain Pass mine(Van Gosen, Verplanck et al. 2019) during the period between the mid-1960s to the early 1990s. Stimulated by the invention of NdFeB permanent magnets in Japan in 1984(Pang Siming 2011), China began the mining of the domestic REE deposits, the mineral processing of their ores and the development of the flowsheet to extract and separate the individual REEs in the late 1980s. Within two decades, China rapidly caught up and obtained the control over the world’s REE

production. By 2011 the processed REEs provided from China made up 95 % of the world market(Van Gosen, Verplanck et al. 2019). According to USGS’s report(USGS 2019), China produced approximately 70.5 percent of the global production, following by the United States with about 8.8%.

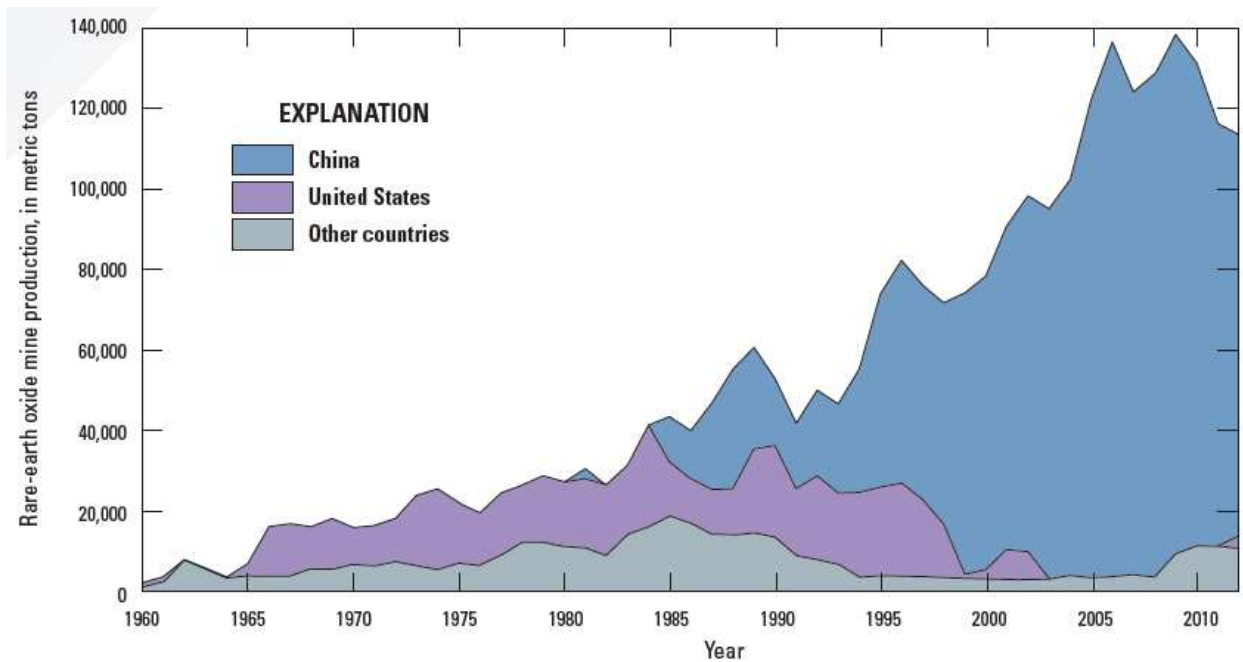


Figure 1-1 World mine production of rare-earth oxides, by country and year, from 1960 to 2012(Van Gosen, Verplanck et al. 2019).

1.1.3 Criticality of REEs

In the past decades, China has dominated the production for rare earth materials, producing more than 90% of the global production. The rest of world relies heavily on importing rare earth materials from China. Heavy dependence on a single country as a source of the rare earth materials has becomes of concern to many groups including countries such as the United States, Japan, and the European.(Van Gosen, Verplanck et al. 2019) The Critical Materials Institute (CMI) of the Department of Energy in the United States categorized rare earth elements

as critical elements. Rare earth metals are considered as essential seasoning ingredients in a larger variety of new technological devices due to their distinctive qualities. With the rapidly increasing demand for rare earth materials to sustain the clean energy economy, it is critical to develop technologies to produce rare earth metals to meet the needs and to control the risk of their supply disruptions(Charalampides, Vatalis et al. 2015, Borges de Lima 2016, Borges de Lima and Filho 2016).

1.2 Oxide-fluoride Molten Salt Electrolysis of Neodymium

The first reported exploration of the possibility to electrically decompose rare earth oxides to produce rare earth metals in the fluoride bath occurred in 1907. During the period from the 1960s to the last 1979s, researchers from the Bureau of Mines (Henrie 1964, Morrice 1964, Morrice and Henrie 1967, Morrice, Shedd et al. 1968, Jenkins 1969, Shedd, Wong et al. 1970, Morrice and Wong 1979) carried out a series of fundamental studies on the electrolysis of rare earth metals in the fluoride molten salt system, which set a base for the development of the technology of oxide-fluoride molten salt electrolysis later. Numerous patents (Goldsmith, Kruesi et al. 1973, Sharma 1987) were claimed to electrowin rare earth metals and their alloys based on the research. With the invention of the NdBFe permanent magnet in 1985 and its widespread applications in clean energy economy, the demand for rare earth elements drove the replacement of the chloride molten salt electrolysis technology for the oxide-fluoride electrolysis.

Compared to the chloride electrolysis process, the advantages of using oxides as the functional electrolyte are evidently obvious(Liu. 1987, Pang Siming 2011). On one hand, the rare earth oxides cost less as opposed to the chlorides and require no extra steps for pre-treatment. On the other hand, the anode products from the process are more desirable carbon dioxide and carbon monoxide in the oxide-fluoride process. With the development of the technology in the

past decades, the recovery and the current efficiency have improved to the level that favors the oxide-fluoride electrolysis as the reported recovery in the process is more than 92% and the current efficiency is 70-80%(Pang Siming 2011). The cell capacity with the fluoride baths is mostly 4,000-6,000 amps and some producers have expanded the unit cell capacity up to 25,000 amps(Pang Siming 2011).

1.3 Justification of research and research scope

In the past decades, the clean-energy economy has been driving the rapidly increasing demand for rare earth metals. More than 90 % of the REMs are produced in China nowadays. The most commercial technique to extract rare earth metals is the oxide-fluoride molten salt electrolysis. The most significant issues associated with the electrolysis production for rare earth metals are low energy efficiency and large PFCs emissions. Given the importance of the oxide-fluoride molten salt electrolysis for the production of rare earth metals and the severe economic and environmental issues jeopardizing the current technology, it is of great theoretical and technique importance to conduct investigations for the electrolysis system and provide guides to address these problems.

This thesis investigates the fundamental electrochemical properties of rare earth molten fluoride electrolyte systems and the fundamentals of the molten salt electrolysis, and it aims to provide scientific contributions to the optimization of rare earth metal electrowinning. The investigated system as molten fluoride electrolyte for the property determination and the electrolysis in this study is mainly $\text{NdF}_3\text{-LiF}$.

The ternary salt system, $\text{NdF}_3\text{-PrF}_3\text{-LiF}$, is extended for the study to determine the melting temperatures at different compositions and its solubilities of Nd_2O_3 at different temperatures. This work attempts to construct a ternary diagram for the liquidus temperatures of

the $\text{NdF}_3\text{-PrF}_3\text{-LiF}$ salt, which provides information with respect to the melting temperatures for different compositions and thus contributes to the determination of the temperature range for investigation for corresponding salts with a specific composition. Besides, the solubilities of the fluoride salts at different temperatures are determined in support of the electrolysis testwork.

One of the important objectives of this thesis is to establish an apparatus to conduct the electrical conductivity measurement for the molten fluorides. On one hand, the setup should be built to enable us to produce reliable electrical conductivity data despite the nature of corrosiveness of the fluoride salts. On the other hand, an extensive discussion regarding the electrical conductivity results, for both specific electrical conductivity and molar electrical conductivity, should be conducted to provide conclusions for better understanding the salt system.

To establish a mathematical model to provide guide to optimize the electrolysis conditions of winning neodymium, both thermodynamics and kinetics of the system should be studied, and the model is developed under clearly specified assumptions. Cell voltage and current are two of the most basic parameters in the molten salt electrolysis and a study on the response of cell voltage to the change of current is worthwhile. Electrolysis cell is designed and constructed to validate the proposed model and conduct further research in terms of electrolysis. This satisfies the goal of attempting to determine how to optimize the cell system to maximize throughput of neodymium production, increase energy efficiency and prevent the process from generating toxic and polluting PFCs.

1.4 Organization of dissertation

This thesis is organized in seven chapters. Chapter 1 constitutes an introduction to the background of the research, delineates the justification of the research and provides the scope of

the investigation to be conducted. In Chapter 2, it covers a literature study on the fundamental research regarding the rare earth oxide-fluoride molten salt electrolysis.

Chapter 3 investigates the liquidus temperature of the $\text{NdF}_3\text{-PrF}_3\text{-LiF}$ molten salt system and the solubility of neodymium oxide in the salt. Chapter 4 details the construction of the conductance cell for the measurement of electrical conductivity of the molten fluorides and discusses the results in terms of the electrical conductivity of the $\text{NdF}_3\text{-LiF}$ salt system at different temperatures and different compositions.

Chapter 5 proposes a mathematical model to elucidate the molten salt electrolysis of $\text{Nd}_2\text{O}_3\text{-NdF}_3\text{-LiF}$ system to produce metallic neodymium and provides insights regarding improving production throughput and energy efficiency and preventing the generation of perfluorocarbon gases (PFCs). In Chapter 6, an experimental setup is designed and constructed to conduct electrolysis testwork and the validation of the proposed mathematical model and more investigation on the system are carried out.

As a last chapter, Chapter 7 gives a conclusion to this thesis, in which the scientific findings and contributions of this research are summarized, and recommendations for future research are enumerated. Presented in the appendices are additional supporting data and operating procedure details to supplement the body of the content.

CHAPTER 2
FUNDAMENTAL STUDY ON RARE EARTH OXIDE-FLUORIDE MOLTEN SALT
ELECTROLYSIS

2.1 Introduction

This chapter reviews the research and technological efforts made on the fundamental properties of the molten salt in the neodymium electrolysis. The properties focused here are density of the fluoride electrolyte, the solubility and dissolution of neodymium oxide in the electrolyte and electrical conductivity of the electrolyte. In addition to that, a confusion on anode effect of the electrolysis and the PFCs generation is discussed. The knowledge gained from this review serves to motivate the specific goals of this research. At the end of the chapter, a list of outstanding questions is raised for further research.

2.2 Density of NdF₃-LiF melt

The determination of the density of the electrolyte is important for the electrolytic cell design and the electrolytic process. On one hand, the density is used to determine the mass of the electrolyte for the electrolytic cell. On the other hand, the density of the melt affects the emission rate of the gas product, the precipitation of the metal product, and the travel distance for the oxide before the completion of dissolution.

Zhang et al. (Liu, Chen et al. 2000) carried out the measurement of the density for the NdF₃-LiF electrolyte system as well as that with addition of Nd₂O₃ with the method of Archimedes'. The results showed that the density, ρ (g cm⁻³), was the function of the content of NdF₃, c (wt%) and temperature, t (°C) with the following relationship:

$$\rho = -4.112 \times 10^{-4}c^2 + 0.137c + 4.134 \times 10^{-4}t - 1.5 \times 10^{-5}ct - 3.817$$

where $73 \text{ wt}\% < c < 83 \text{ wt}\%$ and $1000^\circ\text{C} < t < 1100^\circ\text{C}$. The research also found that with the addition of Nd_2O_3 within its solubility the density showed minimal change.

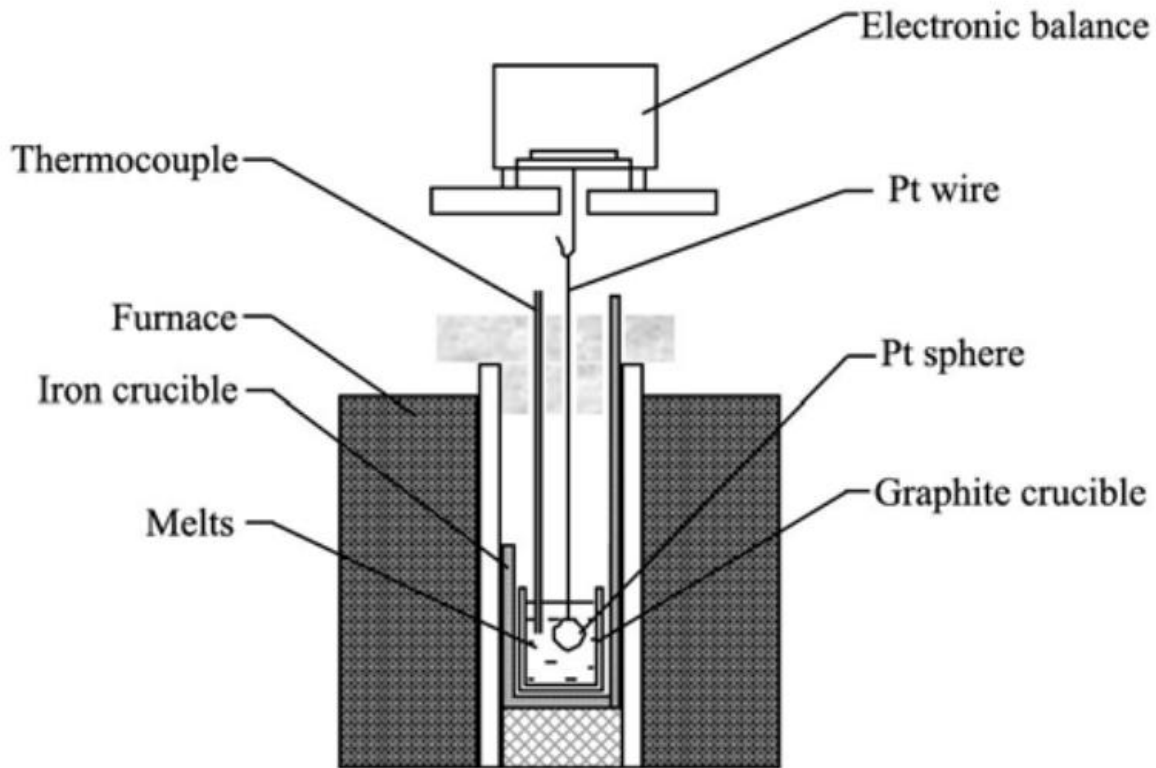


Figure 2-1 Schematic view of density measurement cell used in Hu and coworkers' work

Hu and co-workers (Hu, Wang et al. 2010) studied the density of the $\text{NdF}_3\text{-LiF}$ electrolyte for the neodymium reduction with the same principal for the measurement and the schematic of the cell for the density measurement is shown in . The result was organized and plotted as Figure 2-2. The authors concluded that the density of the melts decrease as temperature increases but increase with the content of NdF_3 in the fluorides. The data in terms of the density of the $\text{NdF}_3\text{-LiF}$ salt system reported by Hu et al. (Hu, Wang et al. 2010) is used for

the nonlinear curve fit as the reference for this research and the density ($\rho/ \text{g cm}^{-3}$) is a function of the content of NdF_3 ($c/\text{wt}\%$) and temperature (T/ K), expressed by the following equation:

$$\rho = -6.53212 \times 10^{-4}c^2 - 0.06987c + 1.31265 \times 10^{-5}T^2 - 0.05297T + 1.69004 \times 10^{-4}cT + 43.14013$$

The correlation factor for the equation above is 0.99399. The range for the NdF_3 content is 72.1wt% - 88.6wt% and that for the temperature is 950°C - 1050°C. Hu and coworkers also discussed the relationship between the density and ionic structure.

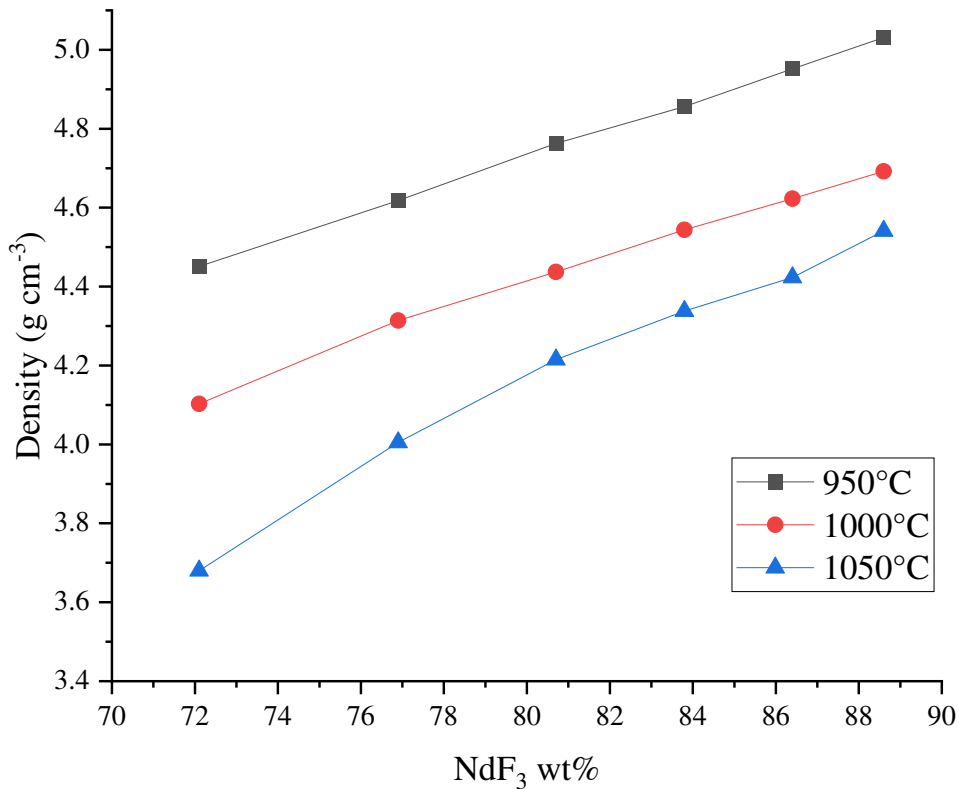


Figure 2-2 Density measurement data by Hu et al. (plotted based on the reported data)(Hu, Wang et al. 2010)

2.3 Solubility and dissolution of rare earth oxide in the fluoride melt

The solubility of the rare earth oxide in the fluoride melt for the electrolysis process and its dissolution behavior are of importance to be studied from both the fundamental and engineering perspectives. However, research on the relevant topic is scarce and in the industrial production, the addition of rare earth oxide into the fluoride electrolyte is commonly based on experience (Pang Siming 2011). It is general knowledge that the solubility of rare earth oxides in the fluoride melt is as low as less than 5 wt% within temperature ranges for research interest. An increasing addition of corresponding rare earth fluoride component increases the solubility and the solubility increases with temperature.

In 1961, Porter and coworkers (Porter and Brown 1960) conducted a series of research on the oxide solubility in the molten fluorides. Representative samples were obtained from an oxide-saturated melt for oxygen content analysis and a filtering device made of graphite was designed to capture analytical sample free from suspended oxide. The oxide content of the sample was analyzed with an inert-gas fusion procedure. The solubility of CeO_2 in the CeF_3 - BaF_2 - LiF (63-16-21 wt%) in this research were reported with an average of 2.1 wt% at 850 °C and 1.4 wt% at 800 °C.

Guo, et al. (Guo, Sun et al. 2016) proposed a semiempirical model for the solubility of rare earth oxides in the molten fluorides. In this study, they compiled the literature data in terms of the solubility of REOs in the fluoride melts as in Figure 2-3. Based on the model developed in their work, the solubility of Nd_2O_3 in the NdF_3 - LiF system with different compositions and different temperatures are predicted and compared with the literature results as shown in Figure 2-4.

Guo and coworkers(Guo, Sun et al. 2018) conducted quantitative study on dissolution behavior of Nd_2O_3 in the $\text{NdF}_3\text{-LiF}$ melts. An *in-situ* observation was achieved with the assistance of confocal scanning laser microscopy (CSLM) to study the dissolution behavior. It was concluded that the rate control process is diffusion step involved in dissolution. At the temperature range from 1141 K to 1291 K, the diffusion coefficient increases from 2.6×10^{-9} to $5.9 \times 10^{-9} \text{ m}^2 \text{ s}^{-1}$ and the activation energy for the process is determined as 68 kJ/mole.

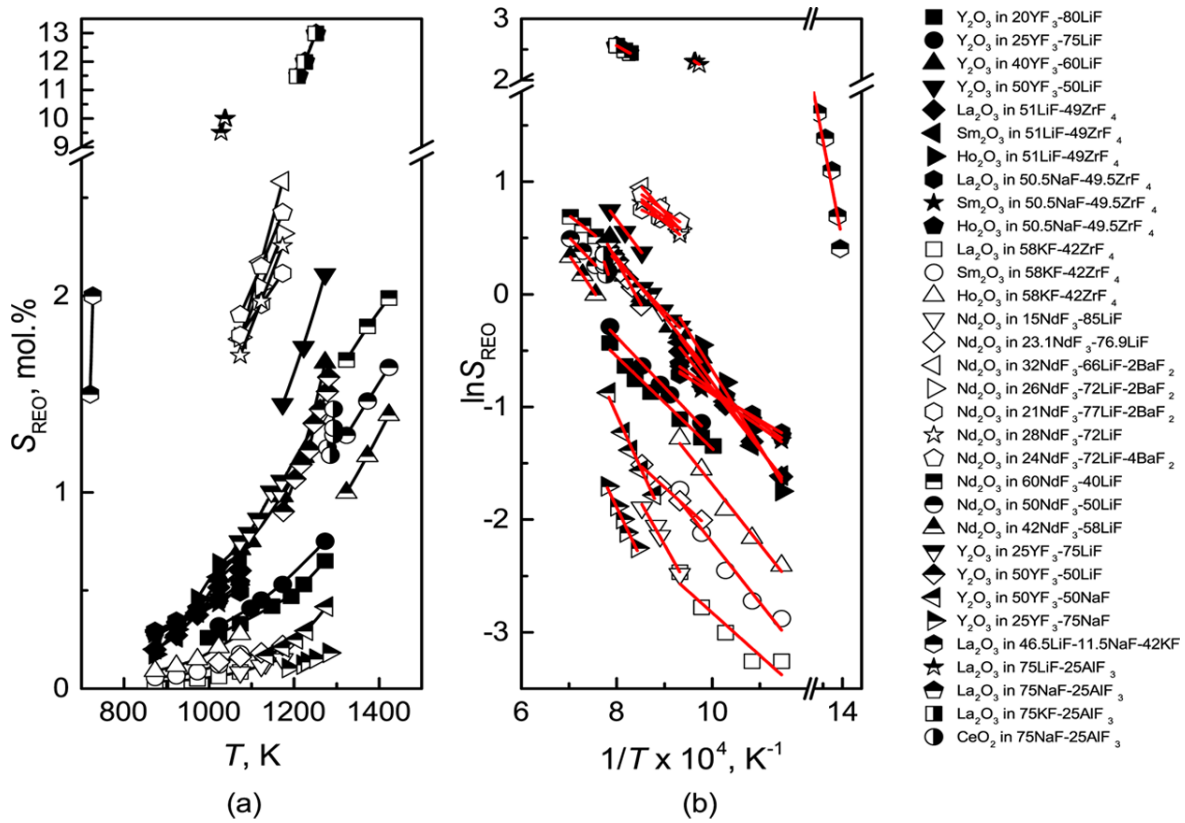


Figure 2-3 Solubility of rare earth oxide in fluoride molten salts(Guo, Sun et al. 2016)

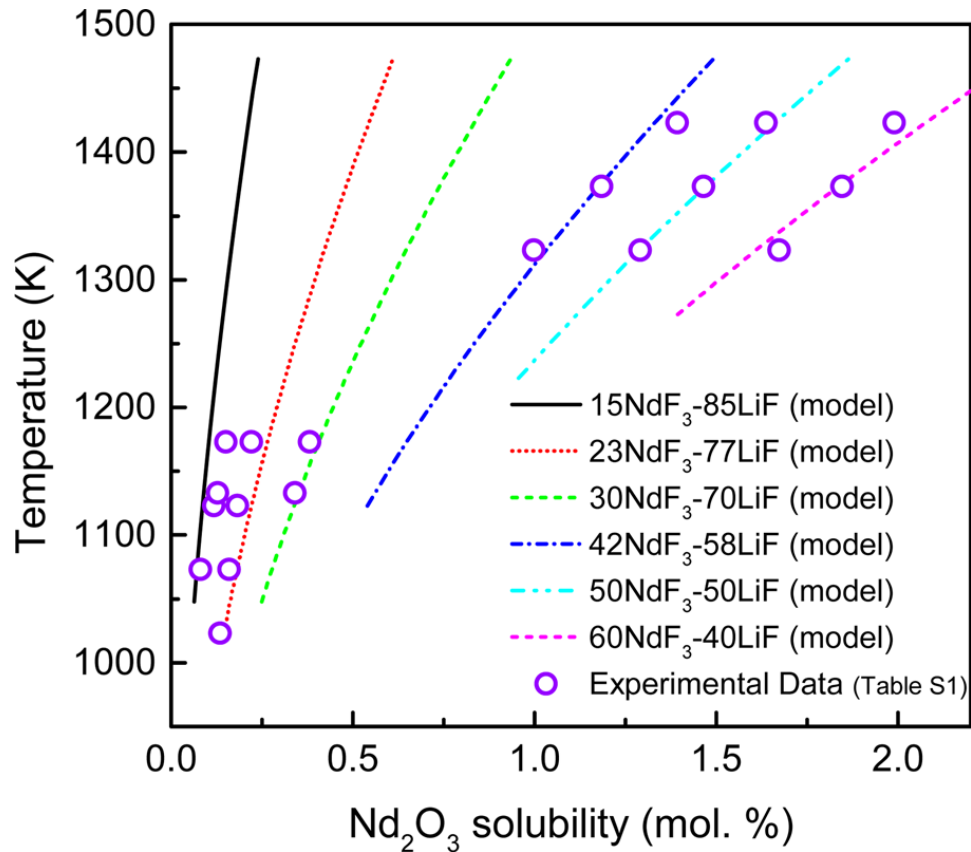


Figure 2-4 Nd_2O_3 solubility in fluoride melts with different NdF_3 -LiF compositions and at different temperatures in Guo, et al' work

2.4 Electrical conductivity of the electrolyte

Electrical conductivity of the fluoride electrolyte is one of the most importance electrochemical property for the electrolysis process. High electrolyte conductivity is desirable to minimize the resistance loss and increase energy efficiency. Little research has been reported in literature in this topic in terms of the rare earth fluoride electrolyte system.

Keller, et al (Keller and Larimer 1997) conducted the measurement of the electrical conductivity for the NdF_3 -LiF fluoride melt with the conductance cell design as Figure 2-5. Only two data points were reported: at 805 °C, the conductivity of NdF_3 -LiF with NdF_3 64.6 wt% was

4.75 $\text{ohm}^{-1} \text{cm}^{-1}$ and at 826 °C, it was 4.57 ohm^{-1} . It was stated by Keller that no intent of accurate measurement of the electrical conductivity in their research.

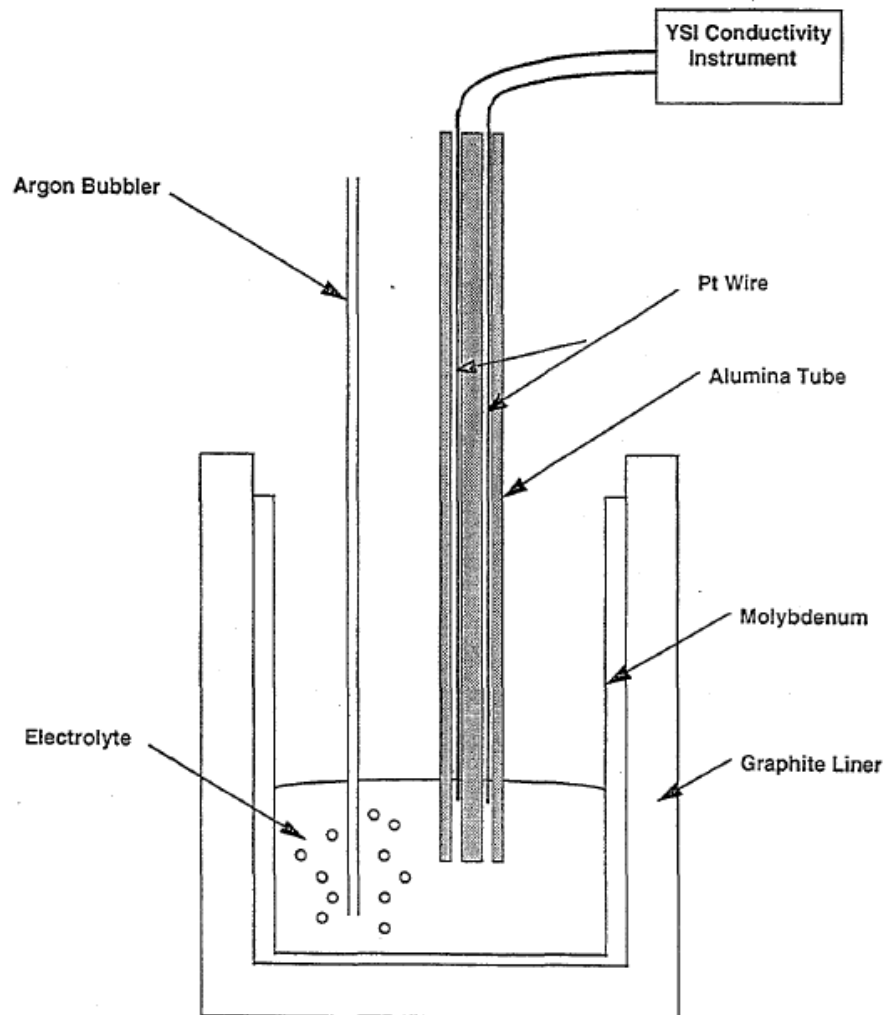


Figure 2-5 Keller's experimental setup to determine electrolyte conductivity(Keller and Larimer 1997)

Zheng et al. (ZHENG, ZHU et al. 2013) exploited the continuously varying cell constant (CVCC) technique and measured the specific electrical conductivity for the $\text{NdF}_3\text{-LiF}$ system with addition of Nd_2O_3 . The change of the conductivity of the melt with temperature and the

Nd₂O₃ content was studied, which indicated that the electrical conductivity of the melt increases with the temperature and that it decreases with the increase of the oxide content. The authors provided a range of the neodymium fluoride content in the melt for the study (83.5-89 wt%) instead of giving a specific value. Figure 2-6 was obtained by compiling the electrical conductivity data shown in the paper.

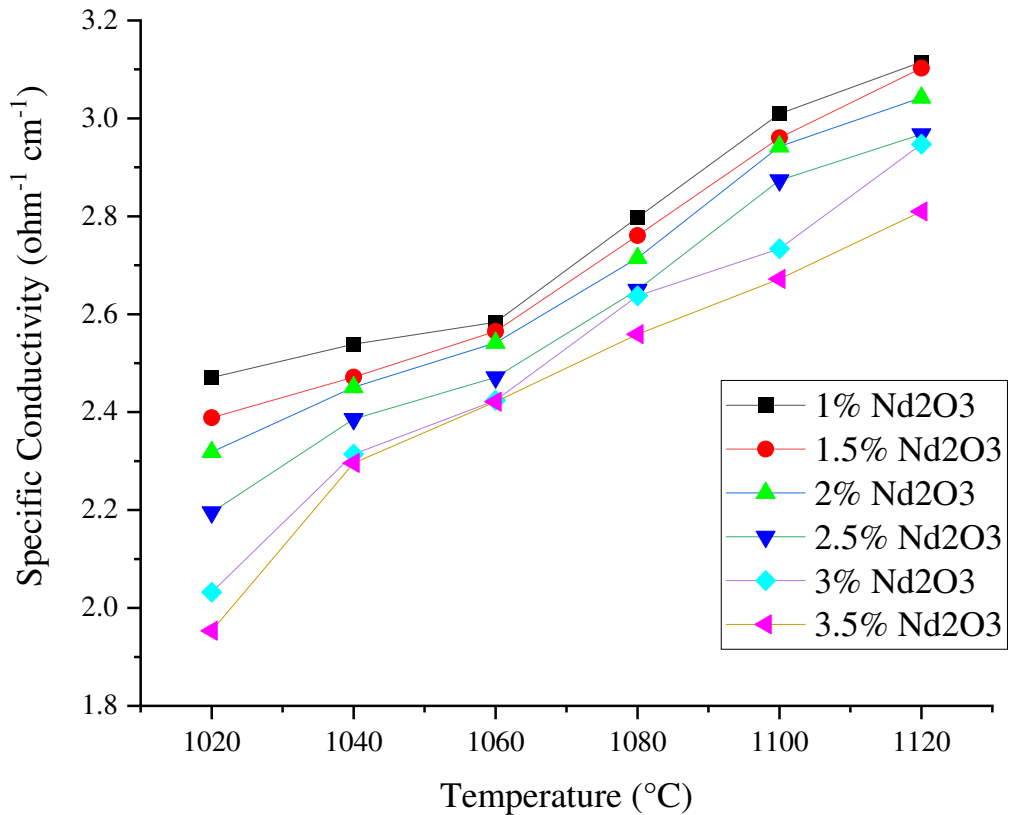


Figure 2-6 Electrical conductivity measurement results by Zheng et al. (ZHENG, ZHU et al. 2013) (plotted based on the graphs in the paper): (83.5-89%)NdF₃-(10-12.5%)LiF salt system

The part of the reason attributed to the lack of research may be that the measurement involves high temperature and corrosive fluoride. Good data for electrical conductivity measurement is hard to obtain. Kim and coworkers designed a conductance cell to suit this purpose of measurement and reported their efforts on the electrical conductivity determination of molten alkaline-earth fluorides. The conductance cell design is presented in Figure 2-7.

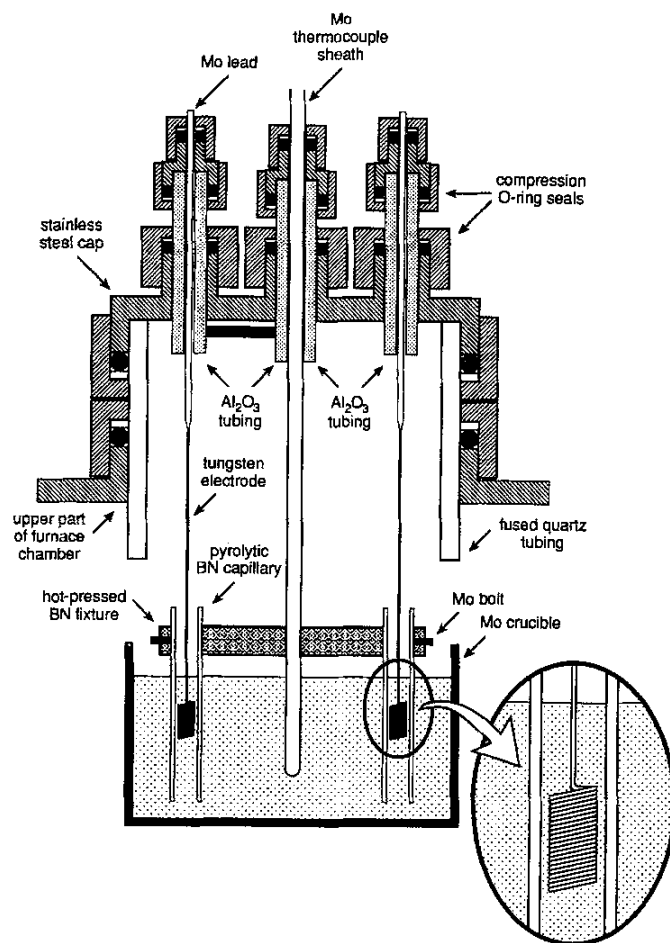


Figure 2-7 Schematic of apparatus for electrical conductivity measurement in Kim's work (Keller and Larimer 1997)

In this conductance cell, two vertical movable electrodes with coils on the ends were used for electrochemical impedance spectroscopy (EIS) measurement with AC posed on the electrode

and by continuously varying cell constant the results were taken. The specific electrical conductivity was determined by the following equation:

$$\kappa = \left(\frac{dZ_{cell}}{dl} \right)_{Z''=0}^{-1} \frac{dG}{dl}$$

2.5 Confusion on anode effect PFCs generation

Anode effect is a common phenomenon occurring in the molten salt electrolysis process. Anode effect is defined as “the effect produced by polarization of an anode in the electrolysis of fused salts. It is characterized by a sudden increase in voltage and a corresponding decrease in a amperage due to the anode being virtually separated from the electrolyte by a gas film.(ASM Gloss.; ASM Metals Handook, v.1. (Gloss 1961))” This effect is caused by ineffective removal of gas product from the anode at elevated current.

In the process of molten oxide-fluoride electrolysis to win aluminum and rare earth metals, perfluorocarbons (PFCs) including CF_4 and C_2F_6 are produced from the decomposition of the fluoride component and cause the inefficiency of the process and environmental issues. Perfluorocarbons (PFCs) include tetrafluoromethane (CF_4) and hexafluoroethane (C_2F_6). Owing to the extreme stability of PFCs in the atmosphere and their strong infrared band absorption capacity, PFCs effectively trap heat in the atmosphere and have very high global warming potentials (GWPs) (CF_4 : 7,390; and C_2F_6 : 12,200) and are regarded important greenhouse gases (Sekiya and Okamoto 2010). Zhang and his colleagues (Zhang, Wang et al. 2018) from Qiandong Rare Earth Groups CO., Ltd. estimated that the CO_2e of PFCs is 17.0 thousand tons globally and 15.3 thousand tons in China for the rare earth electrolysis industry.

The generation of PFCs in the molten salt electrolysis has been observed during an upset condition of anode effect(Marks, Roberts et al. 2000). A number of papers (Tabereaux 1994, Haupin 2016, Thonstad, Rolseth et al. 2016) imply that anode effect is the cause of the PFCs

generation. However, there have been many reports (Marks and Bayliss 2012, Thonstad, Rolseth et al. 2016) indicating PFC emissions are being detected during normal operation. Thonstad (Thonstad, Rolseth et al. 2016) and coworker refers to this as “non-anode effect PFC emissions” or simply “low voltage PFC emission”. Marks, et al. (Marks, Roberts et al. 2000) reported “low-level PFC emissions may be produced without a defined anode effect occurring”. From those interesting evidences, a question is raised: does the generation of PFCs at the onset of anode effect mean the anode effect is the cause of PFCs emission? There are few fundamental studies conducted to explain the essential association with the phenomena as far as the author is aware of from literature. It requires further work to establish a good understanding of the phenomena for better economic production of aluminum and rare earth metals.

2.6 Summary

With a review on the fundamental property study of the $\text{Nd}_2\text{O}_3\text{-NdF}_3\text{-LiF}$ molten electrolysis system, it is noticed that little work has been conducted on the electrical conductivity of the fluoride melt and there is a confusion regarding the cause of decomposition of fluorides in the molten electrolysis process. However, both are of great importance to elucidate the electrolysis process and address problems on the energy efficiency and PFCs emissions. This research is motivated to mainly work on these two matters and conduct fundamental studies to provide guide on increasing energy efficiency and reducing PFCs emissions.

CHAPTER 3

INVESTIGATION ON LIQUIDUS TEMPERATURE OF RARE EARTH FLUORIDE ELECTROLYTE AND THE SOLUBILITY OF NEODYMIUM OXIDE

3.1 Introduction

In order to investigate the electrochemical property of molten fluoride salt, one property which is of great importance is the liquidus temperature of the salts with different compositions. The salt achieves complete fused state only when the temperature is above its liquidus. Another important property is the solubility of the oxide in the salt. The solubility of rare earth oxide in the molten fluorides are both of theoretical and technical significance in terms of the design of the electrolyte for electrolysis and the process operation. In this chapter, we discuss the investigation on the liquidus temperature of $\text{NdF}_3\text{-PrF}_3\text{-LiF}$ molten salts and the Nd_2O_3 solubility in the molten fluorides. HF-DSC is adopted to determine the corresponding properties.

3.2 Methodology and experimental

3.2.1 Heat-flux differential scanning calorimetry (HF-DSC)

Differential thermal analysis (DTA) and heat-flux differential scanning calorimetry (HF-DSC) are adopted to determine the liquidus temperature of the mixture samples. DTA and HF-DSC analysis intends to determine the discrepancy in temperature (for DTA) or heat flow (for DSC) between the test materials and an inert standard during programmed heating or cooling with the energy changes continuously monitored and recorded (Boettinger, Kattner et al. 2007, ASTM 2018). The experiments conducted in this work follow the guideline of ASTM E794-06.

As indicated in Figure 3-1, T_n represents extrapolated crystallization onset temperature and it can be taken as the liquidus temperature for the research. Errors from this method of determination of liquidus temperature may result from the varying amounts of supercooling of

the materials. Samples with high purity materials may exhibit larger amounts of supercooling than polymeric, alloy and impure organic and inorganic chemicals because the latter have sufficient nucleation sites for repeatable determinations of crystallization temperatures (International 2018). On heating, melting requires an input of thermal energy and hence a downward peak is observed indicating the process is endothermic; on cooling, the freezing process releases thermal energy and indicates to be exothermic with an upward peak.

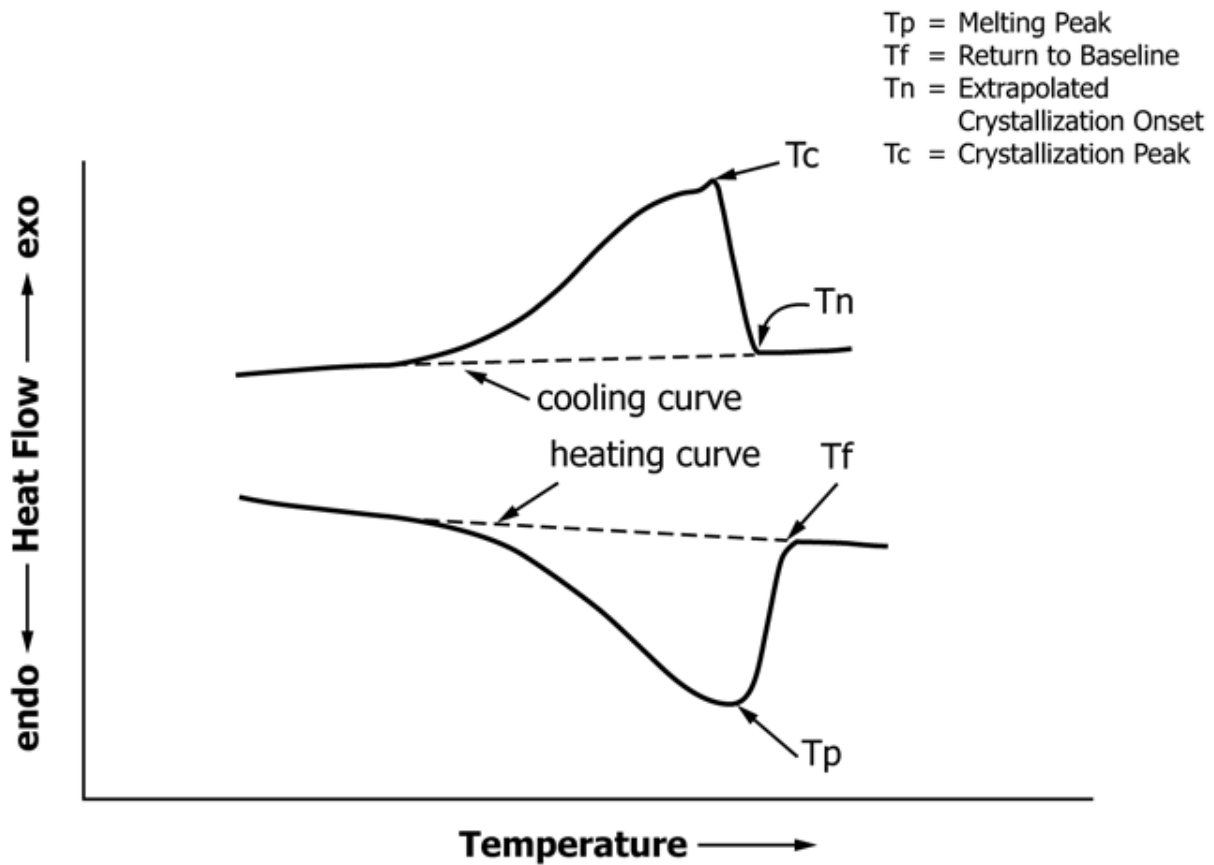


Figure 3-1 Fusion and crystallization temperature for polymeric materials (International 2018)

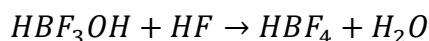
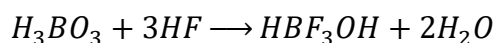
In this research, a TGA-DTA/DSC (SETSYS Evolution TGA-DTA/DSC, SETARAM Instrumentation) is used to conduct HF-DSC tests to determine the liquidus temperature of the

samples. The sample weighing 35-40 mg is contained in a graphite crucible with a lid and another crucible with no sample is used as a reference. DSC is carried out with the equipment programmed to heat with a ramp of 40 K/min from room temperature up to 1200 °C, hold the temperature at 1200 °C for 2 min and then cool the furnace with a ramp of 30 K/min back to 25 °C. Helium is used as a protective gas.

3.2.2 Inductively coupled plasma mass spectroscopy (ICP-MS)

Inductively coupled plasma mass spectroscopy (ICP-MS) is well-known as an effective trace element technique for rare earth element analysis and it has clear advantages in its multi-element characteristics, speed of analysis, detection limits and isotopic capacity(Thomas 2013). This research adopts ICP-MS for the determination of the element components in the samples and the confirmation of the compositions of the DSC test samples.

The components of the samples are lithium fluoride (LiF), neodymium fluoride (NdF₃) and praseodymium fluoride (PrF₃). Although LiF can be dissolved in nitric acid easily, NdF₃ and PrF₃ are difficult to dissolve in common acids. Thus, aqua regia is required to dissolve the complete sample for the ICP-MS test. In addition, excess boric acid is added to the aqua regia prior to the addition of the sample to prevent the production of hydrogen fluoride with the following exothermic reactions:



3.2.3 Determination of liquidus temperature of fluoride mixtures

The mixture of fluorides with certain composition is continued to mix with ceramic grinding media (yttria stabilized zirconia, 3mm, Inframat Advanced Materials). Anhydrous ethanol is added prior to grinding to protect the materials from overheating. The mixture is then

dried in an oven overnight and tested with ICP-MS to determine the composition. Sample the mixture multiple times for ICP-MS tests to make sure the fluorides are fully mixed.

The fully mixed fluorides are sampled to run DSC tests. The post-DSC samples are collected for composition confirmation with ICP-MS. By determining the extrapolated crystallization onset temperature, the liquidus temperature of the fluorides is determined.

3.2.4 Determination of solubilities using DSC

The liquidus temperature of the mixture of fluorides with a specific composition added with a certain amount of oxide can be interpreted as a given temperature at which the oxide is saturated in the molten fluoride salt assuming the oxide is the first phase to crystallize at liquidus temperature. With this considered, the measurement of solubilities of the oxide becomes a question of the measurement of liquidus temperature for the mixture of fluorides and oxide. The same technique is used to conduct the measurement as in 3.2.3.

3.3 Results and discussion

3.3.1 Liquidus temperature measurement

Figure 3-2 represents the general curve of the DSC test using the sample with the composition of $\text{NdF}_3\text{-PrF}_3\text{-LiF}$ (60.5-24.5-15.0 wt%) as an example. As can be seen in the figure, during the heating process, the sample absorbed thermal energy from the surrounding and it is endothermic, thus the heat flow indicating negative value. At 723 °C, the melting of the sample commenced and a peak was observed. The melting of the sample proceeded until reaching its completely fused state. As the figure depicts, the cooling process was exothermic and the point of 865 °C was onset of the crystallization of the sample, the temperature value of which was recorded as the liquidus temperature.

Table 3-1 compares the results from this method for pure lithium fluoride and $\text{NdF}_3\text{-LiF}$ salts with different compositions with those reported in literature by Thoma (Thomas 2013). This shows the values are close and the method used in this research produces reliable results.

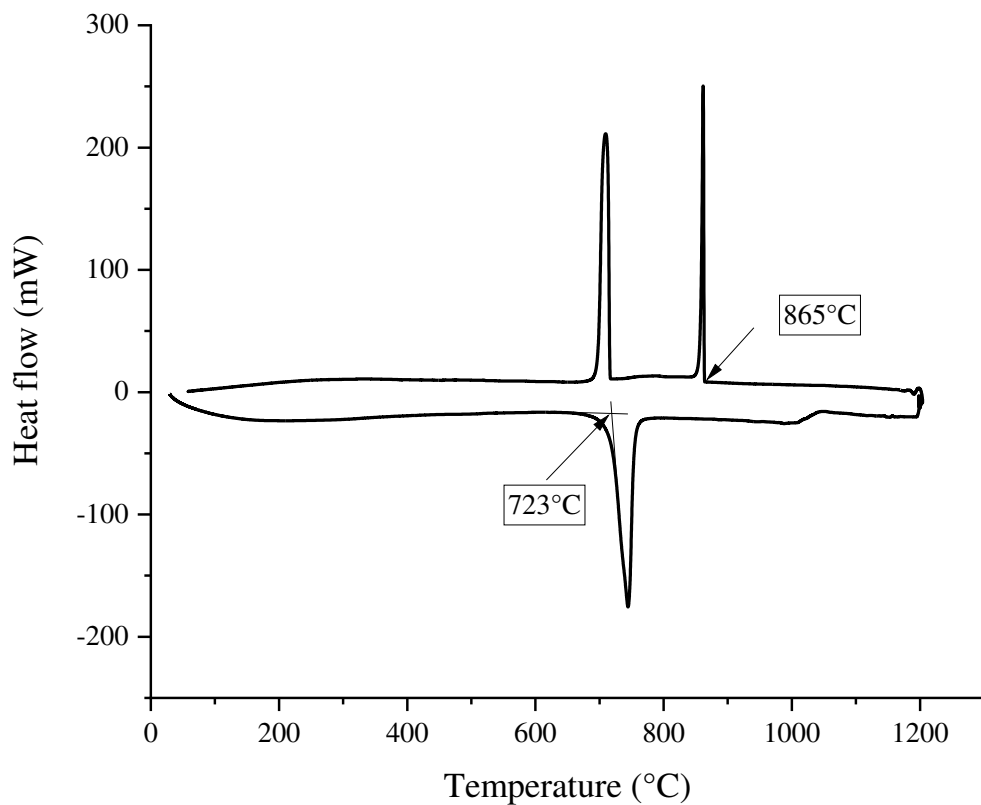


Figure 3-2 DSC results for $\text{NdF}_3\text{-PrF}_3\text{-LiF}$ (60.5-24.5-15.0 wt%)

Table 3-1 Comparison of measured data with the literature data by Thoma regarding NdF₃-LiF melt system

Test #	Composition		Solidus		Liquidus	
	NdF ₃ (wt%)	LiF (wt%)	Measured (°C)	Literature(Thoma 1975) (°C)	Measured (°C)	Literature(Thoma 1975) (°C)
1	0	100	850	848	839	848
2	82.6	17.4	726	730	872	884
3	71.1	28.9	727	730	749	750

Table 3-2 List of results for liquidus temperatures for NdF₃-PrF₃-LiF salts by DSC

Test #	Composition (wt%)			Solidus (°C)	Liquidus (°C)
	NdF ₃	PrF ₃	LiF		
1	62.8	17.2	20.0	720	874
2	59.9	13.6	26.5	722	783
3	59.5	18.9	21.6	724	807
4	62.5	13.7	23.8	720	777
5	59.0	16.3	24.7	724	779
6	55.3	13.1	31.6	720	732
7	49.7	13.8	36.5	718	722
8	48.1	11.7	40.1	725	728
9	60.5	24.5	15.0	723	865
10	36.0	8.7	55.3	724	714
11	82.6	0.0	17.4	726	872
12	71.1	0.0	28.9	727	749
13	52.7	12.9	34.4	720	732

Table 3-2 lists the DSC results in terms of the liquidus temperature and the composition of the sample is confirmed with ICP-MS. Combined the results reported by Thoma regarding the

binary fluoride salt systems, $\text{NdF}_3\text{-LiF}$ and $\text{PrF}_3\text{-LiF}$, the data from this work is used to construct a ternary contour diagram to present the liquidus temperatures for the $\text{NdF}_3\text{-PrF}_3\text{-LiF}$ salt system, as in Figure 3-3.

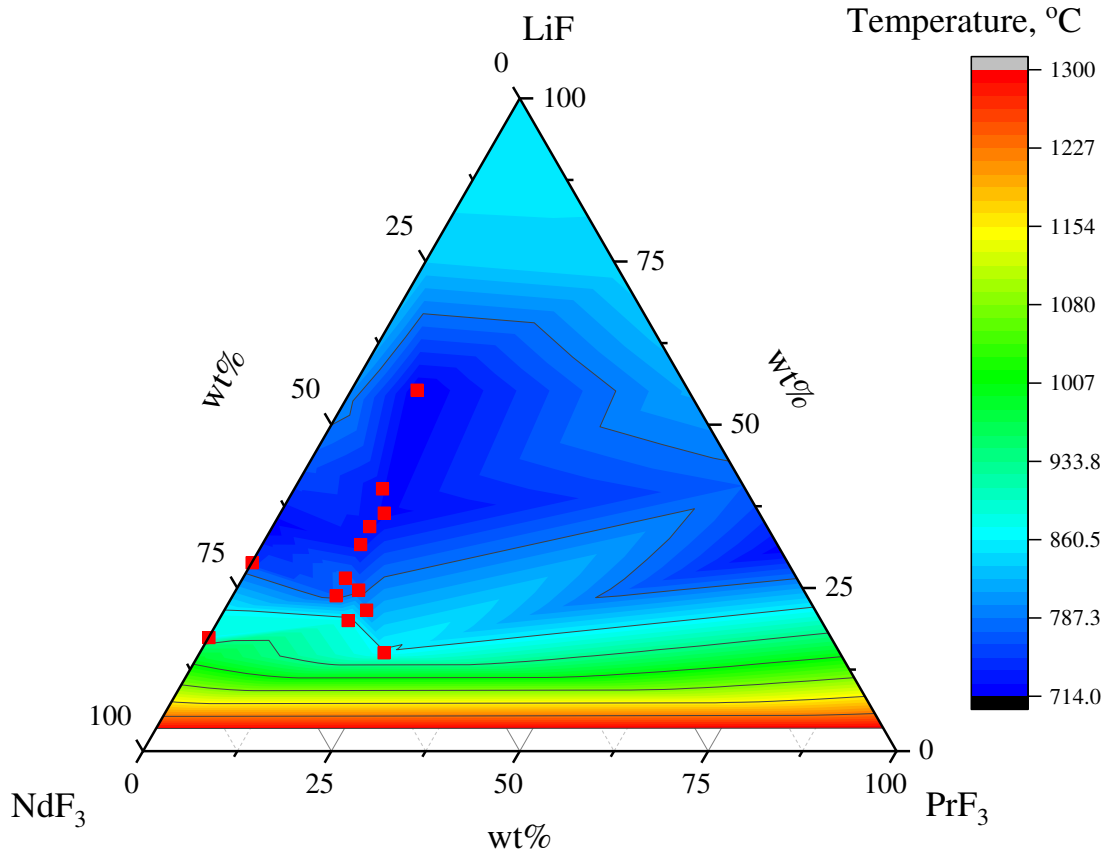


Figure 3-3 Ternary contour diagram of the liquidus temperature for the $\text{NdF}_3\text{-PrF}_3\text{-LiF}$ system based on data from this research (red square dots in the diagram) and the reported data by Thoma ($\text{NdF}_3\text{-LiF}$ and $\text{PrF}_3\text{-LiF}$ phase diagrams)

3.3.2 Measurement on the solubility of Nd_2O_3

With the same technique, the solubility of Nd_2O_3 in the $\text{NdF}_3\text{-LiF}$ (82.6-17.4 wt%) and $\text{NdF}_3\text{-PrF}_3\text{-LiF}$ (36.0-8.7-55.3 wt%) salts were determined.

Figure 3-4 depicts the DSC result for the NdF_3 -LiF salt with a composition of NdF_3 82.6 wt% and LiF 17.4 wt% compared with that with various amounts of Nd_2O_3 addition into the fluoride mixture. It shows that for the samples with higher amounts of Nd_2O_3 addition the onset of crystallization while cooling occurred sooner. The liquidus temperatures for samples with Nd_2O_3 1.10, 1.77, and 3.39 wt% of the total mass of fluorides are determined to be 957 °C, 979 °C, and 1053 °C.

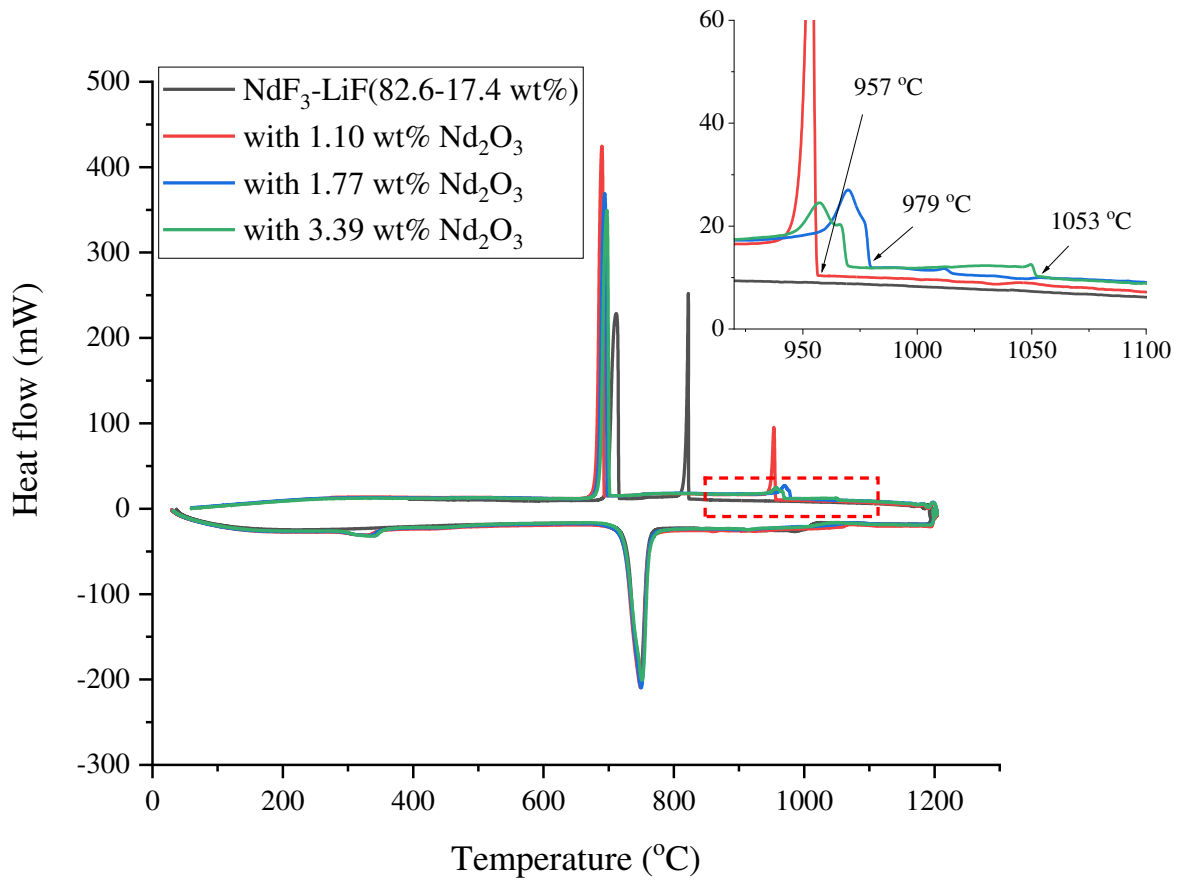


Figure 3-4 DSC results for NdF_3 -LiF (82.6-17.4 wt%) and its mixtures with Nd_2O_3 (1.10, 1.77, 3.39 wt% of total fluoride mass)

Figure 3-5 shows the DSC result for the NdF_3 - LiF salt with a composition of NdF_3 36.0 wt%, PrF_3 8.7 wt% and LiF 53.3 wt% compared with that with various amounts of Nd_2O_3 addition into the fluoride mixture. Similarly, the liquidus temperatures for samples with Nd_2O_3 0.66, 0.89, and 1.78 wt% of the total mass of fluorides are determined to be 900 °C, 936 °C, and 1071 °C.

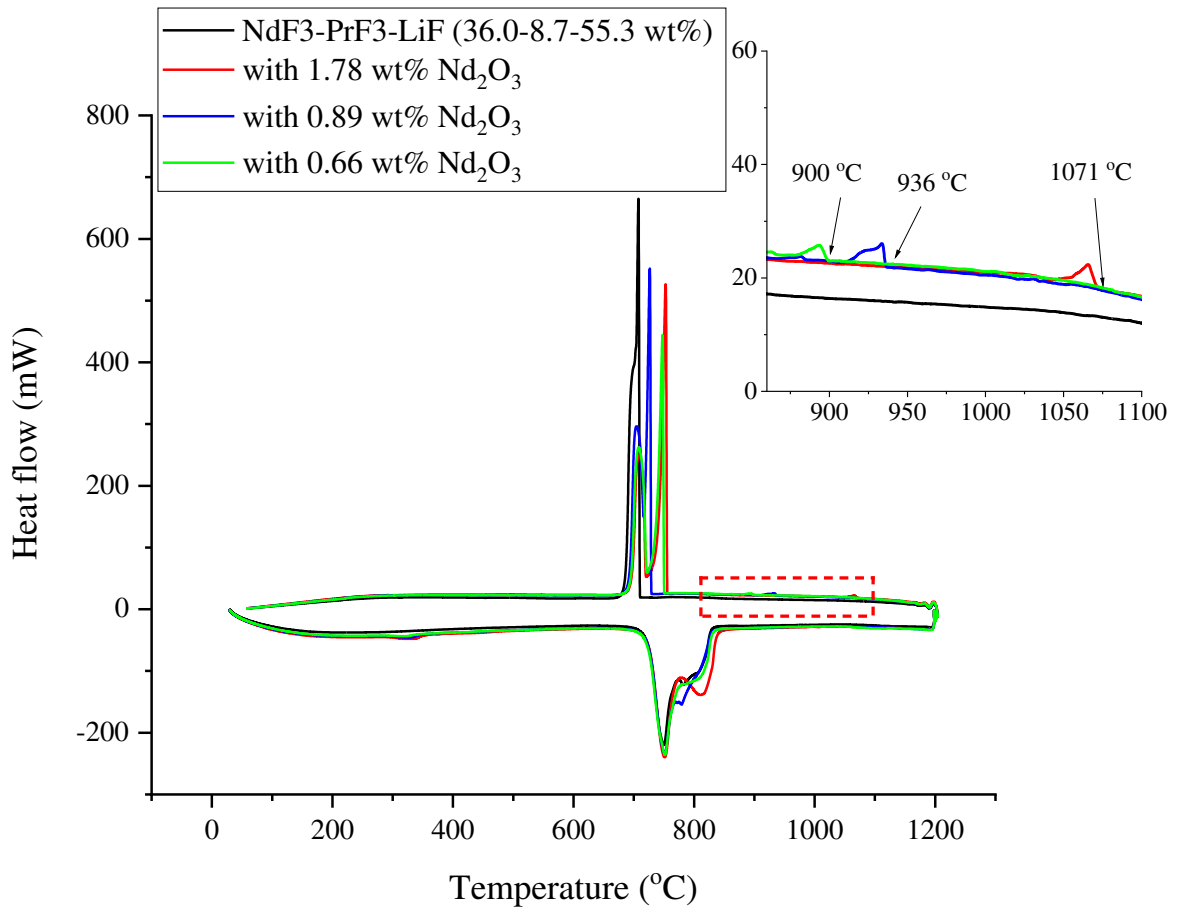


Figure 3-5 DSC results for NdF_3 - PrF_3 - LiF (36.0-8.7-55.3 wt%) and its mixtures with Nd_2O_3 (1.78, 0.89, 0.66 wt% of total fluoride mass)

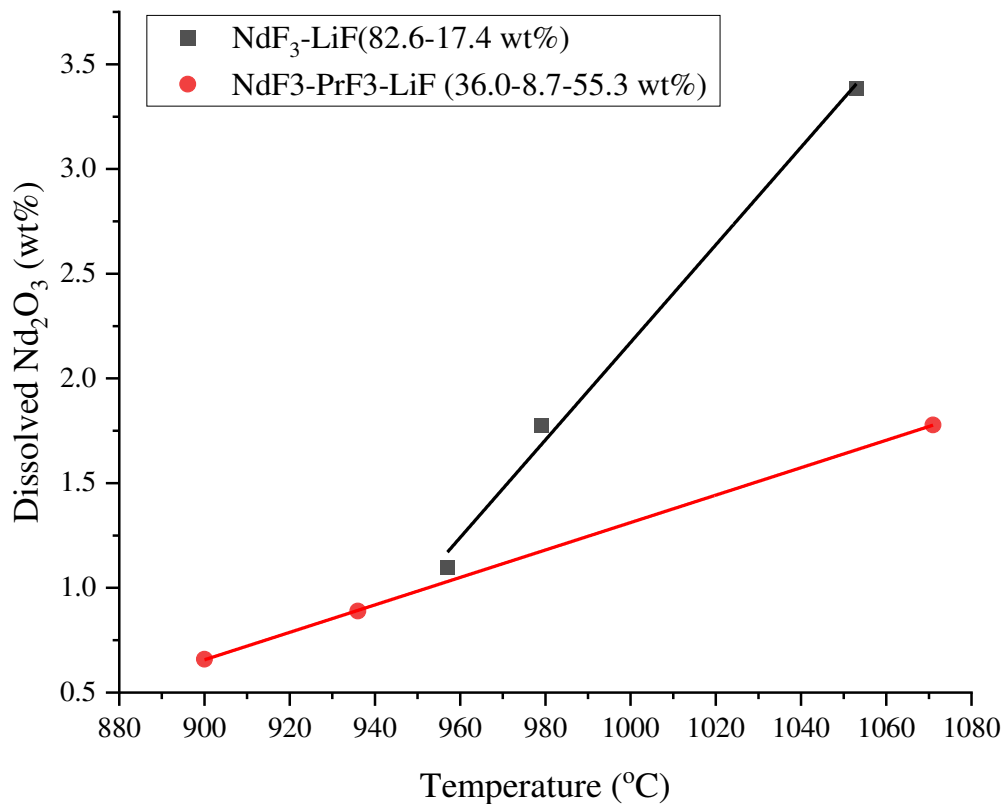


Figure 3-6 Solubility of Nd_2O_3 in the $\text{NdF}_3\text{-LiF}$ (82.6-17.4 wt%) and $\text{NdF}_3\text{-PrF}_3\text{-LiF}$ (36.0-8.7-55.3 wt%) salts (presented in wt% of the total mass of the fluorides)

Considering that at the liquidus temperature the mixture of oxide and fluoride reaches its saturation state of the oxide in the fluoride, the data obtained from above can be converted as the solubilities of the oxide in the fluoride salt at a certain temperature. With this considered, the results for the solubility determination are presented in Figure 3-6 and Figure 3-7 in mass percentage and molar percentage, respectively. As shown in Figure 3-6, for both salt system, the solubility of Nd_2O_3 in the fluorides increases with temperature and a good linearity exists and the solubility of the oxide in the $\text{NdF}_3\text{-LiF}$ with NdF_3 82.6 wt% is greater than that for the $\text{NdF}_3\text{-PrF}_3\text{-LiF}$ with NdF_3 36.0 wt%. An explanation for this is that the increased presence of NdF_3 is

beneficial to the dissolution of Nd_2O_3 and increases the solubility of the corresponding oxide. This is congruent with the previous result by peer researchers (Guo, Sietsma et al. 2014) in terms of the conclusion that the rare earth oxide solubility increases with the REF_3 content in the melts. The same conclusions can also be drawn from an analysis of Figure 3-7.

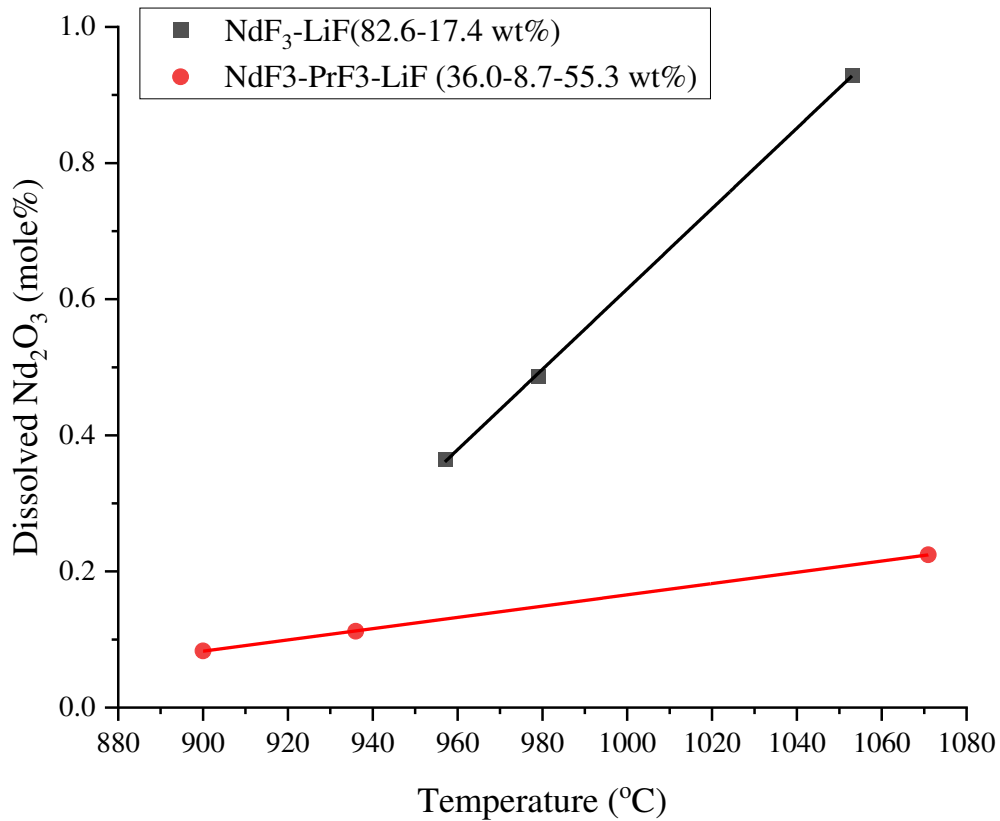


Figure 3-7 Solubility of Nd_2O_3 in the $\text{NdF}_3\text{-LiF}$ (82.6-17.4 wt%) and $\text{NdF}_3\text{-PrF}_3\text{-LiF}$ (36.0-8.7-55.3 wt%) salts (presented in respective mole% of the total moles of the fluorides)

3.4 Conclusion

In this research, liquidus temperatures of mixed NdF_3 , PrF_3 and LiF were determined with the technique of differential scanning calorimetry (DSC) and inductively coupled plasma

mass spectroscopy (ICP-MS) was used to characterize the composition of the mixture. A ternary diagram of liquidus temperatures with respect to the $\text{NdF}_3\text{-PrF}_3\text{-LiF}$ system has been constructed. This informs the choice of the experimental temperature range when investigating the properties of the $\text{NdF}_3\text{-PrF}_3\text{-LiF}$ molten salt with a specific composition.

Furthermore, the same technique was adopted to estimate the solubility of Nd_2O_3 in the fluoride melt considering at the liquidus state of a fluoride salt containing a small amount of Nd_2O_3 the fluoride salt is considered saturated with the oxide. Compared with other techniques to evaluate the oxide solubility in molten salts, this novel technique requires only small sample amounts and is easy to operate. The results indicate that the presence of NdF_3 in the fluoride salt increases the solubility of Nd_2O_3 even though the solubility of Nd_2O_3 is not high. The results also show that the Nd_2O_3 solubility in the fluoride salt increases with temperature. In this research, it shows that the solubility of Nd_2O_3 in the $\text{NdF}_3\text{-LiF}$ (NdF_3 82.6 wt%) is 3.39 wt% of the total fluoride mass at 1053 °C.

CHAPTER 4

ELECTRICAL CONDUCTIVITY MEASUREMENT OF MOLTEN SALT NdF_3 -LiF ELECTROLYTE

4.1 Introduction

Electrical conductivity is a fundamental property of a molten salt in electrolysis applications. It is of both theoretical importance and technological significance. The electrical conductivity information enables us to understand the transport phenomena in the electrolysis process as well as the melt structure. In metallurgical processes such as molten salt electrolysis, it provides important information for metallurgists to determine the thermal balance and energy efficiency for process design and optimization. The electrowinning of rare earth metals is achieved mainly through molten fluorides with oxide dissolved in the salt. The NdF_3 -LiF salt system is used as electrolyte for neodymium production. Nd_2O_3 has extremely low solubility in fluoride salts except for molten NdF_3 and thus NdF_3 is an essential component in the carrier electrolyte. The addition of LiF decreases the melting point for the salt and increases the electrical conductivity of the electrolyte. The high corrosiveness of fluoride salts renders a reliable measurement of the electrical conductivities of fluorides difficult to achieve. Little information on the electrical properties of the NdF_3 -LiF salt system is found in the literature.

The first objective of the current research was to construct a conductance cell which withstood the severe conditions for electrical conductivity measurements of fluorides and produced reliable results. Secondly, it aimed to carry out measurements of the electrical conductivities of NdF_3 -LiF salts with different compositions and temperatures. Lastly, efforts were made to interpret the data and understand the electrical properties of the salt system.

4.2 Experimental setup

4.2.1 Conductance cell construction

In order to achieve the goal for the measurement of the electrical conductivity of the molten fluorides, an experimental apparatus is designed and constructed based on The detailed description in the previous work of Kim and coworkers (Kim and Sadoway 1992), and some modifications and improvement are made. The schematic of the conductance cell is illustrated in Figure 4-1. The core of the apparatus is the conductance cell constituting a pair of pyrolytic boron nitride tubes, movable tungsten electrodes and a graphite crucible. The temperatures of the melt are measured by a Type K thermocouple, protected in a closed-one-end Inconel tube immersed in the melt.

The boron nitride tubes measuring 6.4 mm ID X 12.7 mm OD X 12.7 cm in length are mounted on a fixture of a molybdenum plate with a thread connection. The molybdenum plate is suspended underneath the lid with a threaded rod connected in between. Boron nitride has high thermal conductivity and low electrical conductivity, and it performs well to resist the severe conditions of high corrosiveness and high temperature in this environment. The boron nitride components are fired in the atmosphere at 800 °C for 10 hours prior to being applied in the conductance cell for measurements.

The electrodes of the conductance cell are made of tungsten wire (99.95% metal basis, Alfa Aesar, Tewksbury, MA), 0.75 mm diameter X 40 cm long. Constituting eighteen turns, a tightly wound coil (4.7 mm diameter X 1.4 cm long) terminates each electrode and the end with the coil is designed to be immersed into the melt, as is shown in Figure 4-2. Gas tungsten arc welding (GTAW) is used to connect the other end of the electrode with a molybdenum rod

(99.95% molybdenum, Torrey Hills Technologies, San Diego, CA), 4.8 mm diameter X 30.5 cm long. The electrodes are sleeved with alumina through the lid for insulation.

The crucible is made of graphite (Grade CS, Graphite Products Corp. MI, USA) and measured 57.2 mm OD X 50.8 mm ID X 114.3 mm deep X 127.0 mm tall. The inner wall is tapered by 0.5 degree to facilitate removal of solidified material removal from the crucible. On the bottom of the crucible, a blind hole with 12.7 mm in diameter and 6.4 mm in depth is bored to center the crucible in the canister with a boron nitride rod. The crucible is placed on the top of a plate made of boron nitride as electrical insulator. A set of heat shields made of Inconel is held beneath the lid.

The canister used in the experiment is made of Inconel super alloy resilient to persistent at high temperatures. The lid of the cell is made of stainless steel and its configuration design is as Figure 4-3. The fitting connection is as shown in Figure 4-4. A stainless steel tube is bent and welded against the stub of the lid and used to run cooling water to limit the lid temperature. Figure 4-5 is a picture of the configuration of the conductance cell underneath the lid.

In the experiments, the electrodes are moved vertically within the boron nitride insulating tubes to change the effective interelectrode spacing. The controlled movability of the electrodes is achieved by the installation of a set of screw set collars for each. The mechanism of changing the electrode position is illustrated in Figure 4-6. The upper collar is fixed in the position which allows the lower end of the electrode coil distant from the bottom of the boron nitride tube by 2mm when the lower collar sits free on the insulating alumina tube. A set of spacers measuring 2, 4, 6, and 8mm are built for determining the vertical offset of the electrodes. The spacer sits between the two electrodes and then the lower collar is fixed. By using the spacer accordingly, the interelectrode spacing can change in increments of 2 mm up to 16 mm total.

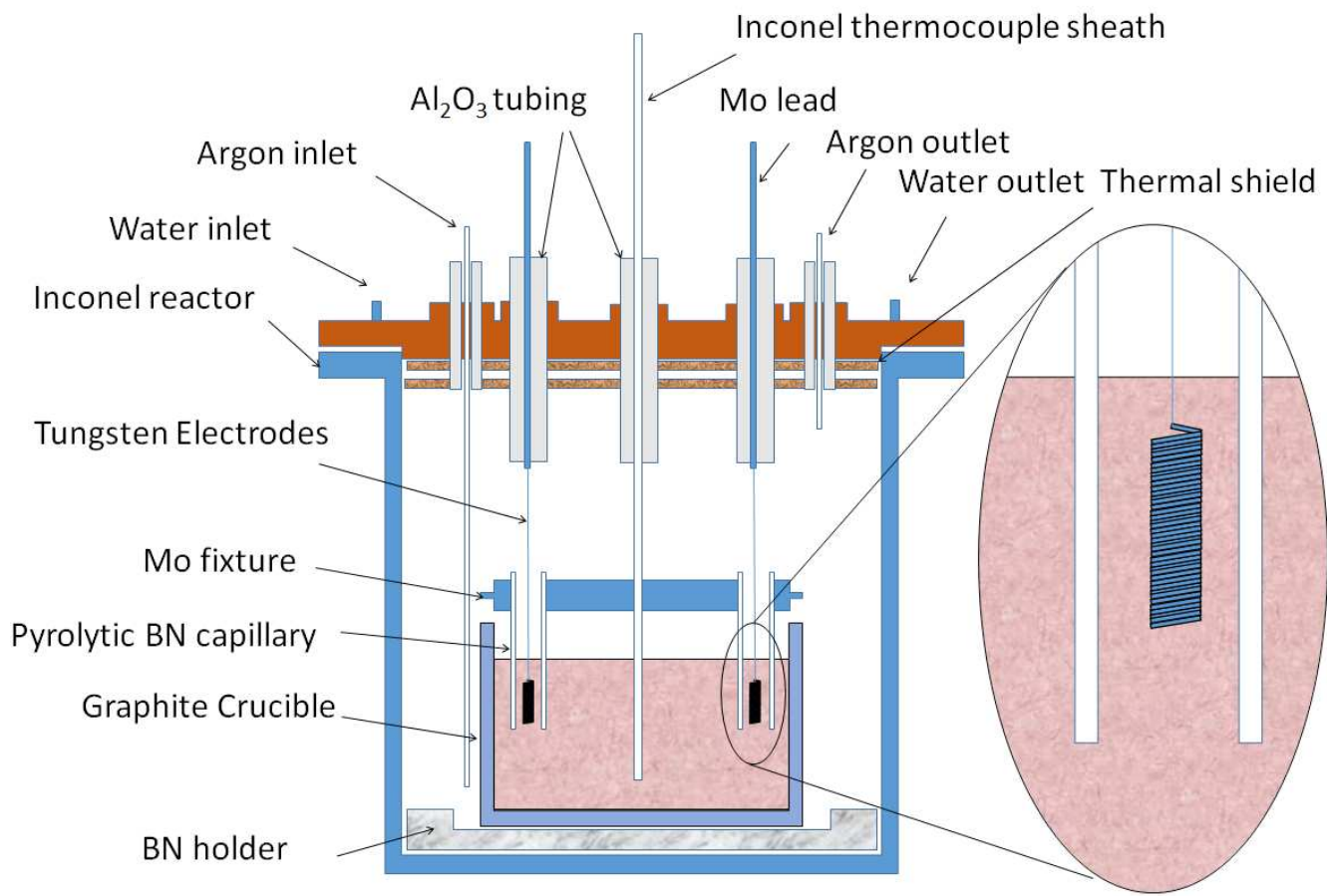


Figure 4-1 Schematic of conductance cell for electrical conductivity measurement

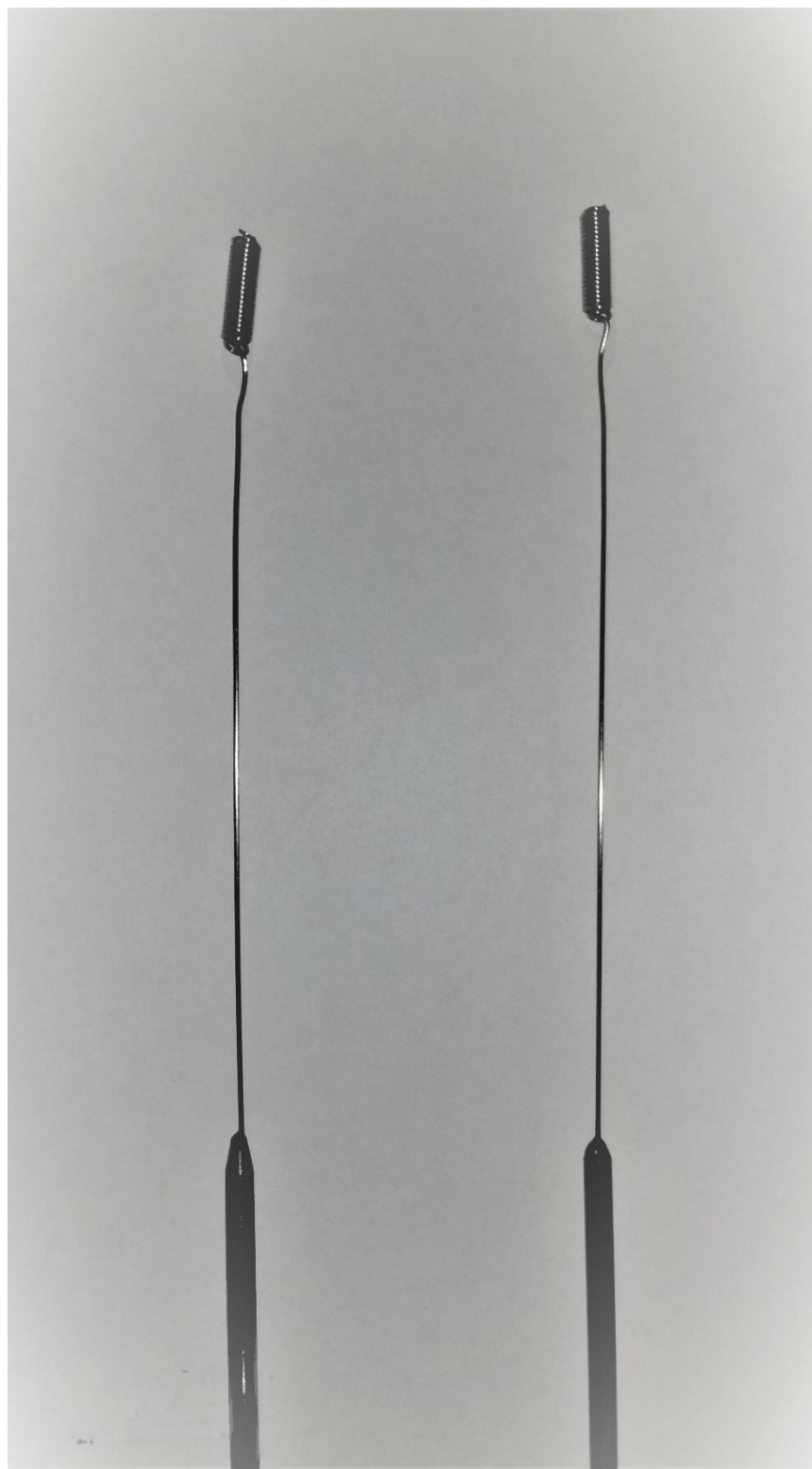


Figure 4-2 Tungsten coil tips of the electrodes for the conductance cell

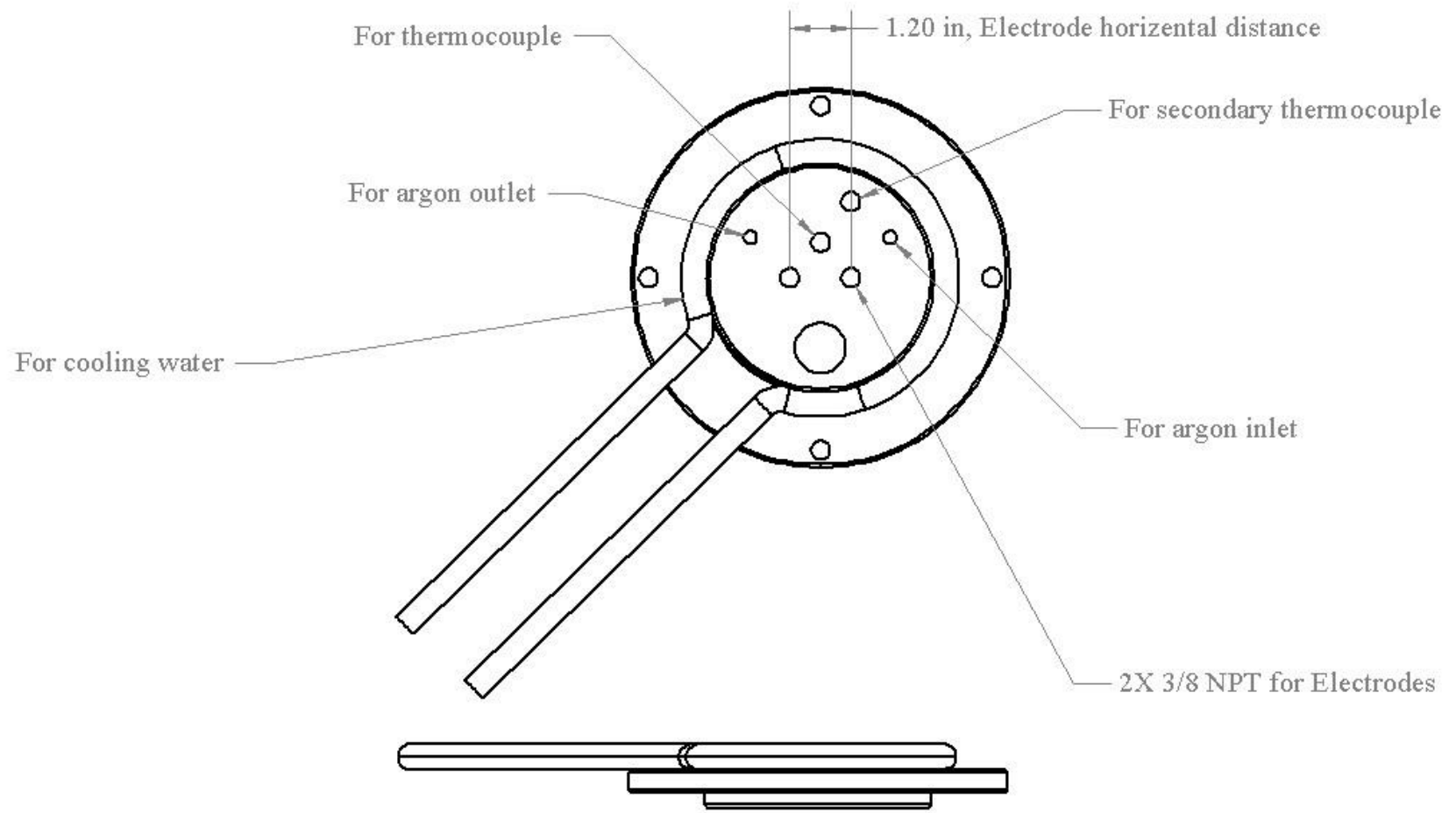


Figure 4-3 Configuration of the cell lid for the conductance cell

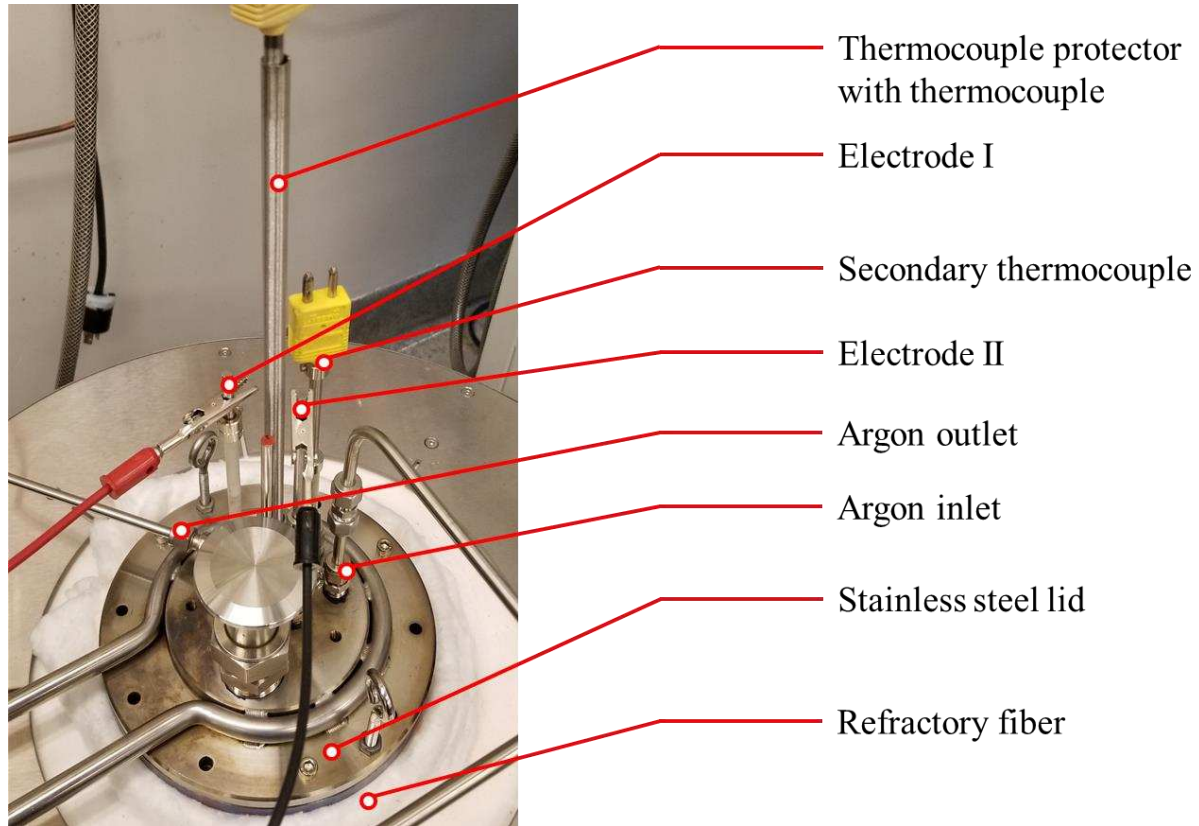


Figure 4-4 Configuration of the conductance cell lid

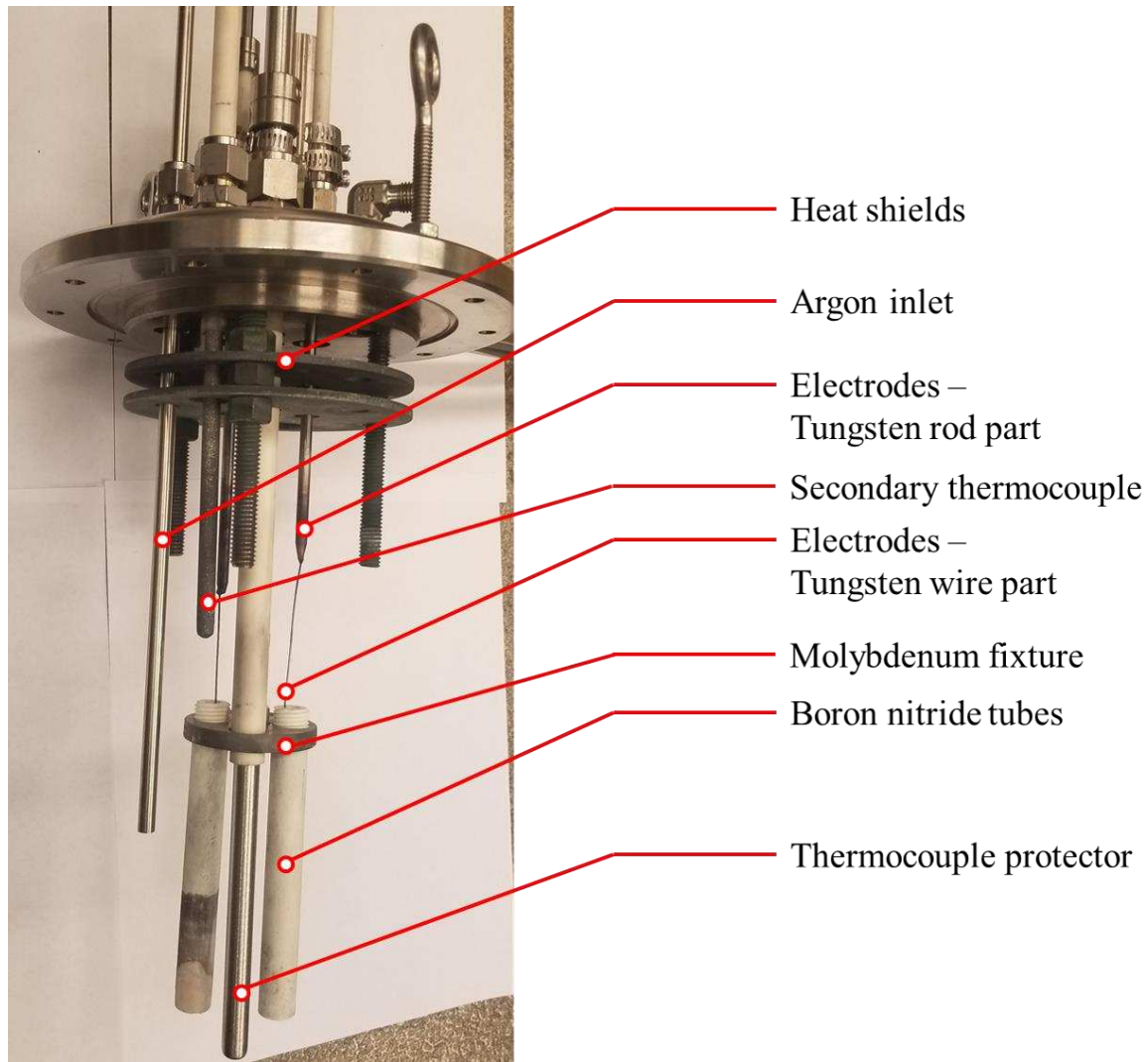


Figure 4-5 Configuration of the conductance cell underneath the lid for EIS measurements

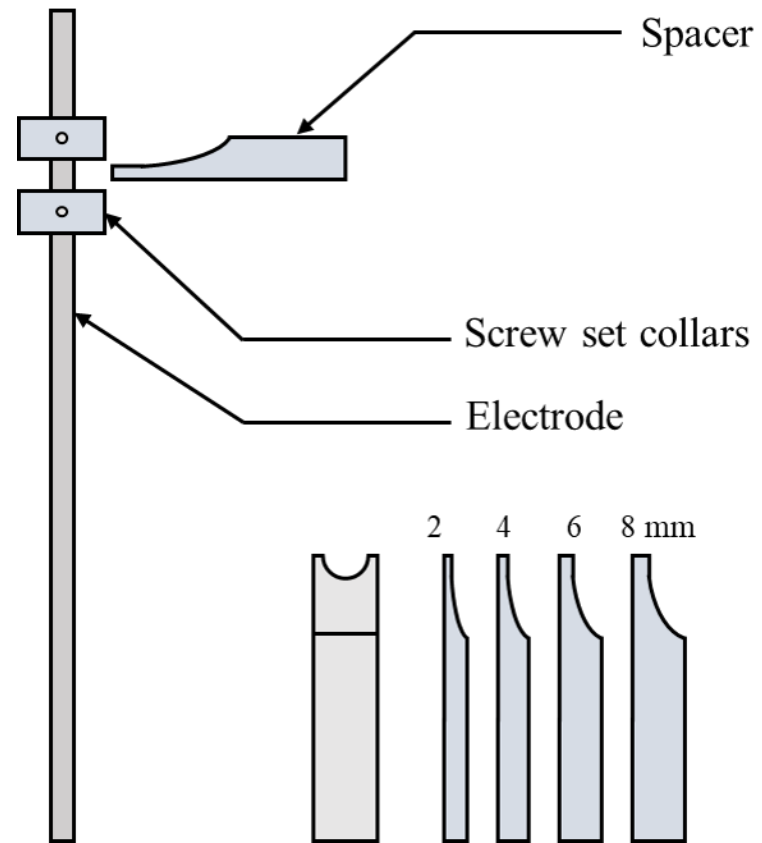


Figure 4-6 Illustration of the design for the change of electrode position for EIS tests

4.2.2 EIS test circuit construction

The system is assembled to carry out EIS tests for the determination of the electrical conductivity. A tubular furnace is used to heat the conductance cell. The controller is connected with the melt thermocouple and uses its signal to control the power to heat the furnace. The furnace temperature is monitored to protect the furnace from overloading. A hoist system powered by a motor is built to lift the lid with attached chains. The furnace and the hoist system are contained in a glovebox chamber in which an inert atmosphere is maintained at well-controlled level (<1 ppm moisture and < 1 ppm oxygen content). Figure 4-7 is a picture of the setup for the EIS test.

An alternative setup (Figure 4-8) is built to conduct measurements outside the glovebox. Within this setup, the argon is continuously injected into the cell to purge the system and protect the graphite crucible and the salt from the oxygen attack.

A Gamry Potentiostat/Galvanostat/Zero Resistance Ammeter (Interface 1000E, Gamry Instrument, USA) are employed for the electrochemical impedance spectroscopy (EIS) experiments on the conductance cell.

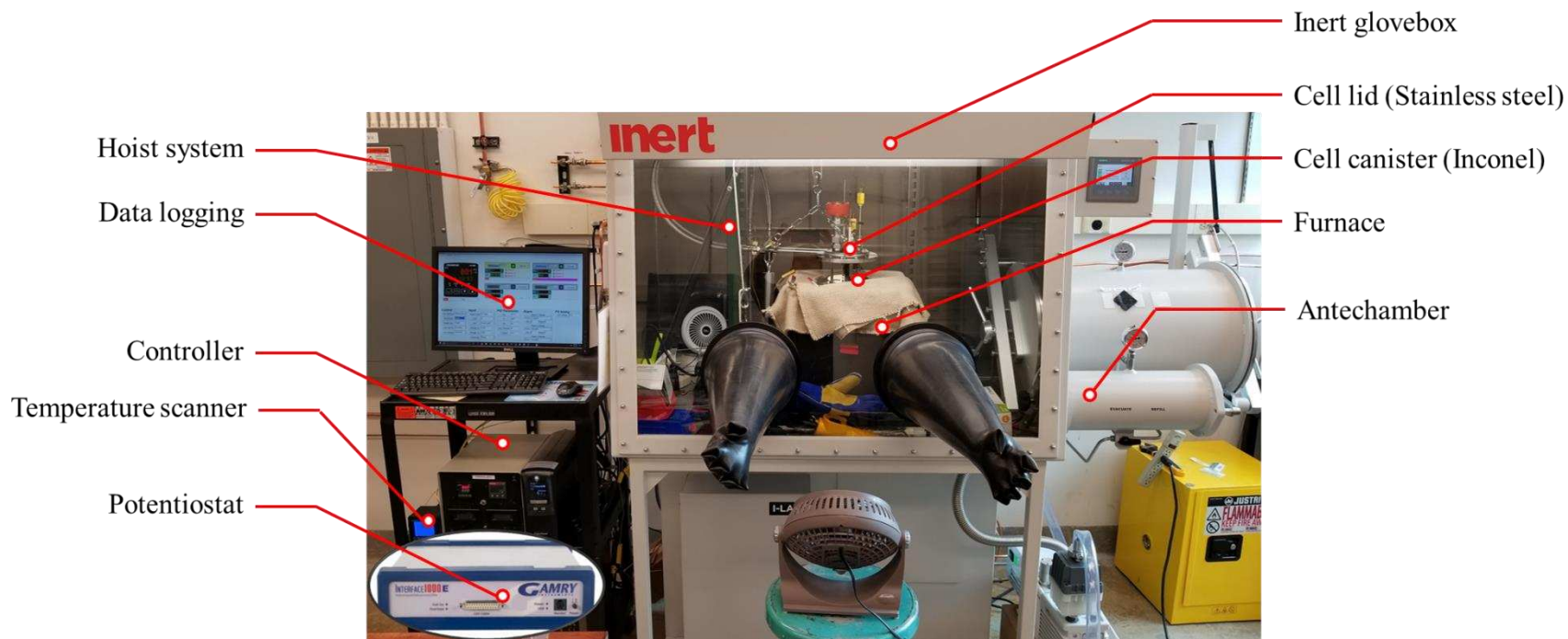


Figure 4-7 Conductance cell system for EIS measurement with glovebox

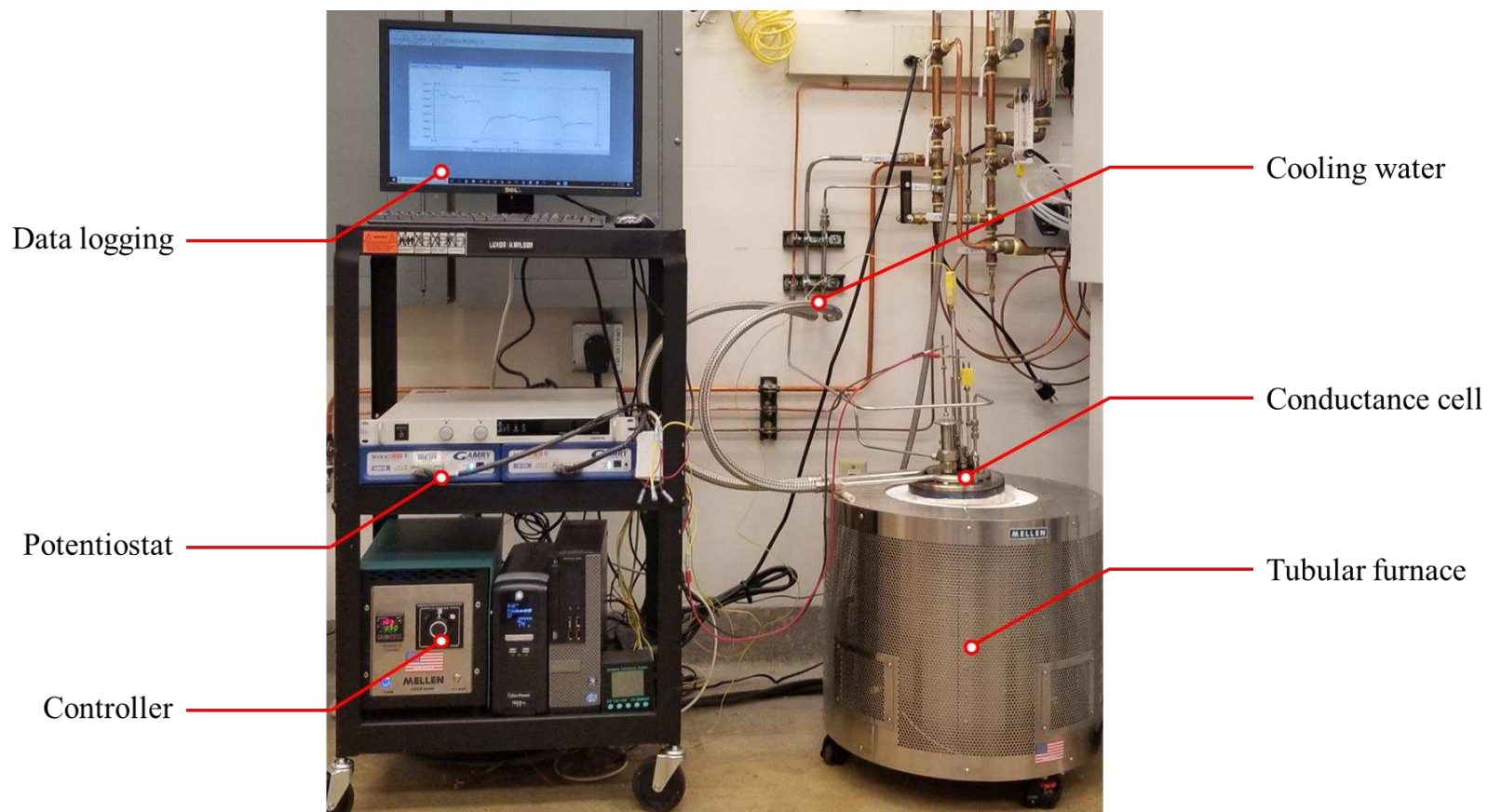


Figure 4-8 Conductance cell setup for EIS measurements

4.3 Methodology and experimental procedures

The Continuously Varying Cell Constant (CVCC) technique is applied to determine the electrical conductivity of the molten salt system. In this method, the impedance of the conductance cell, Z_{cell} , is measured through electrochemical impedance spectroscopy (EIS) with varying electrode distance. The cell constant, G , which is defined as the equivalent cross-sectional area between the electrodes, A , divided by the equivalent electrode distance, l , changes concomitantly. The specific electrical conductivity of the molten salt, κ , is calculated by the following equation.

$$\kappa = \left(\frac{dZ_{cell}}{dl} \right)_{Z''=0}^{-1} \frac{dG}{dl}$$

where $\left(\frac{dZ_{cell}}{dl} \right)_{Z''=0}$ refers to the change of the cell impedance with changing electrode distance when the imaginary part equals zero, which is determined by the experiment in this investigation, and $\frac{dG}{dl}$ represents the change of the cell constant with regard to the change in the electrode distance, which is calibrated with the measurement over a reference salt with known electrical conductivities.

Pure molten lithium fluoride (99.9% pure, -100 mesh, Noah Technologies Corp., Texas) is used as reference salt to calibrate the cell constant term $\frac{dG}{dl}$. The electrical conductivity of lithium fluoride is known from literature (Janz, Janz et al. 1968) according to the following equation:

$$\kappa_{LiF}(\text{ohm}^{-1} \text{cm}^{-1}) = -15.0389 + 3.53546 \times 10^{-2} \times T(K) - 1.28145 \times 10^{-5} \times T(K)^2$$

The lithium fluoride is dried overnight in an oven at 250 °C.

The graphite crucible is loaded with the dried pure lithium fluoride before being transferred into the argon atmosphere glovebox chamber through the antechamber of the system.

After the crucible is in position, the conductance cell is mounted with the lid suspended and the boron nitride tubes above the solid salt. After the salt has melted, the lid is slowly lowered to close the canister. Meanwhile, the tubes are immersed into the melt and positioned with their ends 5 mm above the floor of the crucible. By moving the electrodes up and down slowly several times any gas bubbles built up in the tubes are removed.

After reaching the targeted temperature and waiting for an hour to let the temperature stabilize, the impedance of the conductance cell was measured with the Gamry Interface 1000E to apply an AC voltage across the electrodes and detect the current response through the cell. The potentiostat is programmed to impose a sinusoidal excitation voltage with a fixed amplitude (5 mV) and a frequency set from 10^6 Hz to 100 Hz (30 points per decade). After the entire frequency range is swept and the result is recorded in the program (Gamry Instrument Framework), each electrode is moved by 2 mm, 4 mm, 6 mm and 8 mm with the spacers and the lower collar of the corresponding electrode is fastened prior to each test.

At least 7 intervals for the change of the interelectrode spacing are conducted for the EIS tests. A curve is obtained for each test with the data displayed in a Nyquist plot. The resistance of the cell is determined as the real part of the impedance when the imaginary part equals zero. This value is found to be strictly linear against the interelectrode distance and the correlation factor is greater than 0.999. The term $(\frac{dZ_{cell}}{dl})_{Z''=0}$ is regarded a constant for the melt and its value is the slope of the curve of the determined resistance against the relative distance. As the term $\frac{dG}{dl}$ is constant in the entire range of the interelectrode spacing and the specific electrical conductivity of the melt is known, the value of $\frac{dG}{dl}$ is determined for the calibration. After the last measurement is completed, the melt is heated to another temperature and same experiments is

conducted to determine $(\frac{dZ_{cell}}{dl})_{Z''=0}$. With the known $\frac{dG}{dl}$, the specific electrical conductivity of the salt is calculated and used to compare with the literature data for the error analysis. More temperature levels are investigated. With the completion of the calibration and validation tests, the cell assembly is raised out of the melt and held above it to allow the furnace to cool down to room temperature until the removal of the salt.

The measurement of the electrical conductivities of the molten fluoride mixtures (NdF₃-LiF and NdF₃-PrF₃-LiF) are carried out with the same experimental procedure mentioned above for the cell constant term calibration.

The grade of the neodymium fluoride and the praseodymium fluoride used in the experiments is 99.9%.

4.4 Results and discussion

4.4.1 Equivalent circuit development

An equivalent circuit to the conductance cell is proposed as Figure 4-9. This circuit consists of a series of resistors (melt resistance, electrode resistance, etc.), capacitors (double layer capacitance, etc.) and inductors (coil inductance).

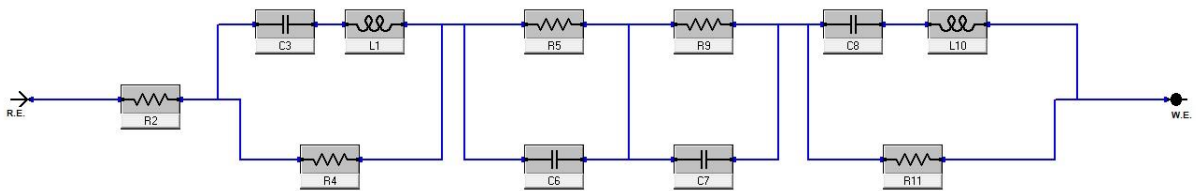


Figure 4-9 Equivalent circuit of the conductance cell: R series represents resistances, C series represents capacitors, and L series represents inductors.

The potentiostat is programmed to impose a sinusoidal excitation voltage over the lithium fluoride melt at 950 °C with a fixed amplitude (5 mV) and a frequency set from 10^6 Hz to 1 Hz (100 points per decade). The results are fitted the results with the proposed equivalent in both Bode plot and Nyquist plot, as shown in Figure 4-10 and Figure 4-11. The patterns of the fitted curves match with the real plots. Therefore, it can be concluded the proposed equivalent circuit can be used to represent the conductance cell circuit.

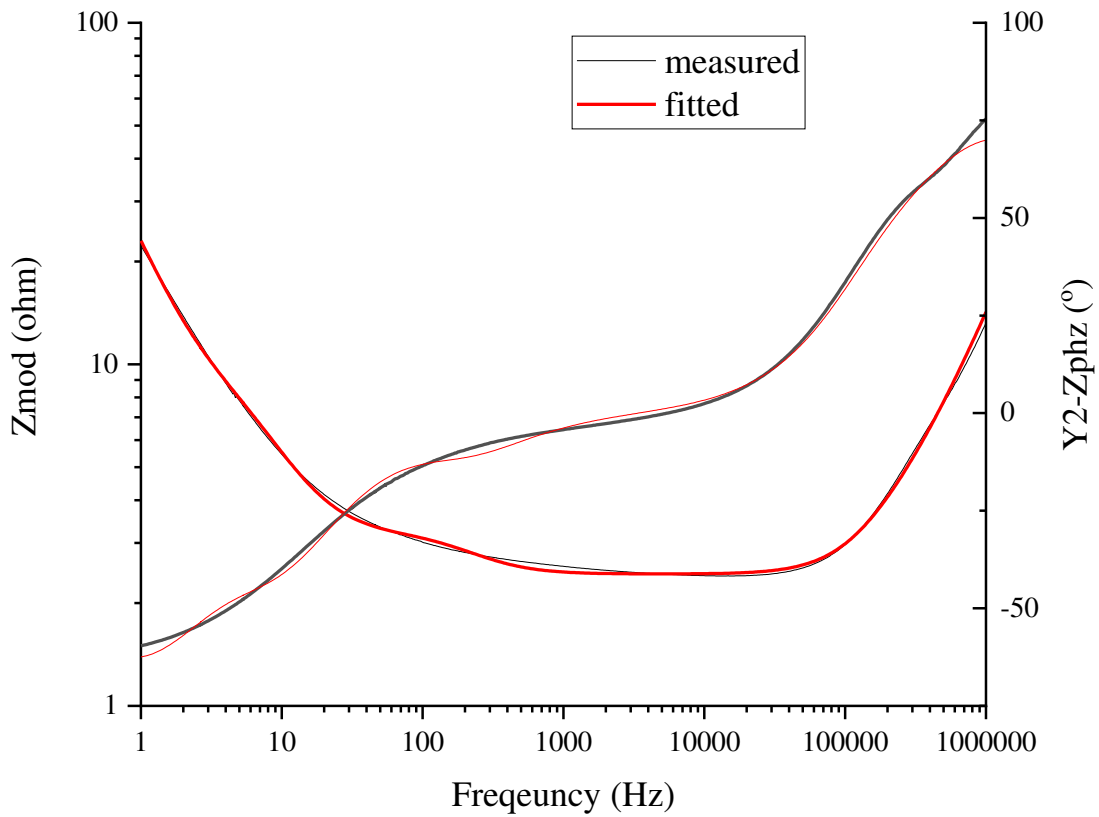


Figure 4-10 Bode plot plot and fitted plot with the proposed equivalent circuit: LiF, 950 °C

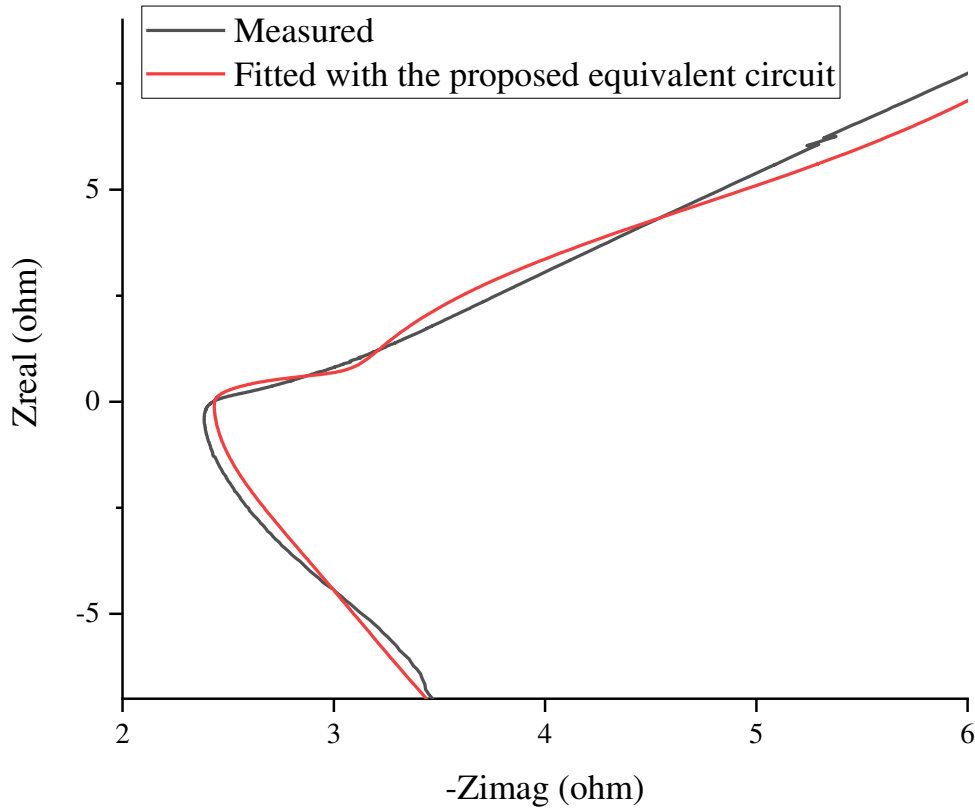


Figure 4-11 Nyquist plot and fitted plot with the proposed equivalent circuit: LiF, 950 °C

4.4.2 Calibration and validation

LiF melts are used to calibrate the cell constant term $\frac{dG}{dl}$ in this experiment. The following paragraphs show an example of calibration and validation for the electrical conductivity measurement. The calibration experiment is carried out at 960 °C within a LiF melt, and the result is shown in Figure 4-12. The real part of the impedance is taken for each curve at $z_{imag}=0$ and it gives the resistance change with increasing interelectrode spacing as in Figure 4-13. Then the slope of the fitted line is used as the value of $(\frac{dZ_{cell}}{dl})_{z''=0}$. With the electrical conductivity of LiF at 960 °C known, the term $\frac{dG}{dl}$ is calibrated. Table 4-1 lists the results for the measurement of

LiF conductivities at other temperatures with the calibration value compared with the literature results. It shows the relative deviation is within 1%, indicating this method provide reliable data for the electrical conductivity measurement of the fluoride melts.

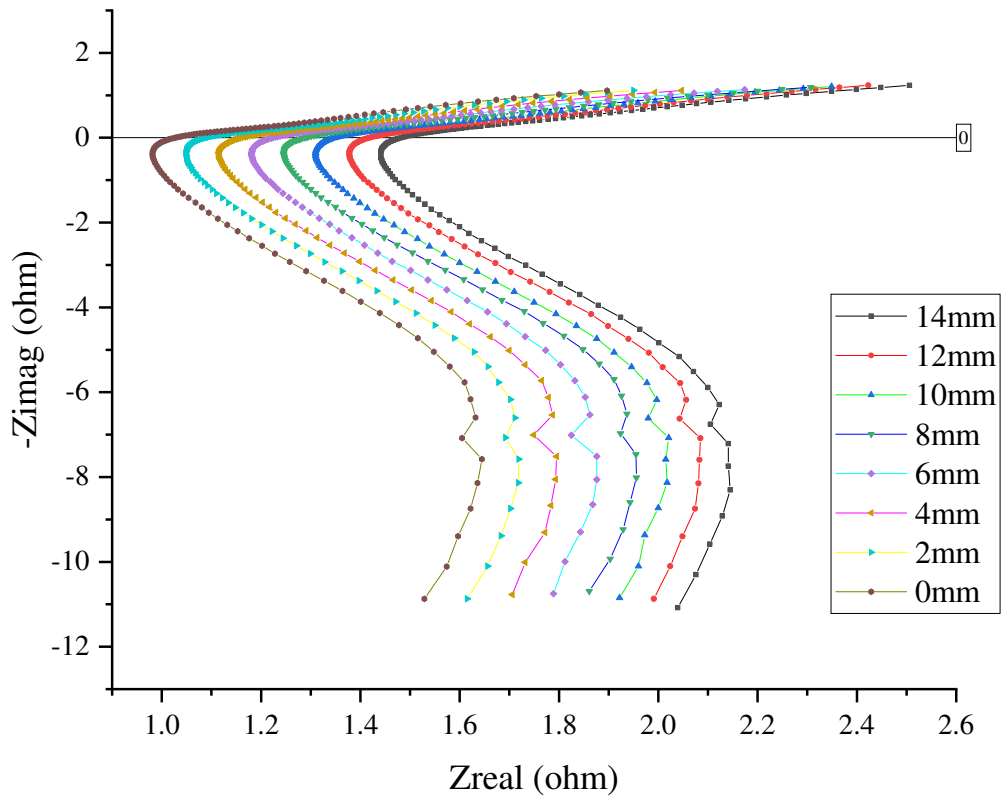


Figure 4-12 Nyquist plot for calibration with LiF at 960 °C

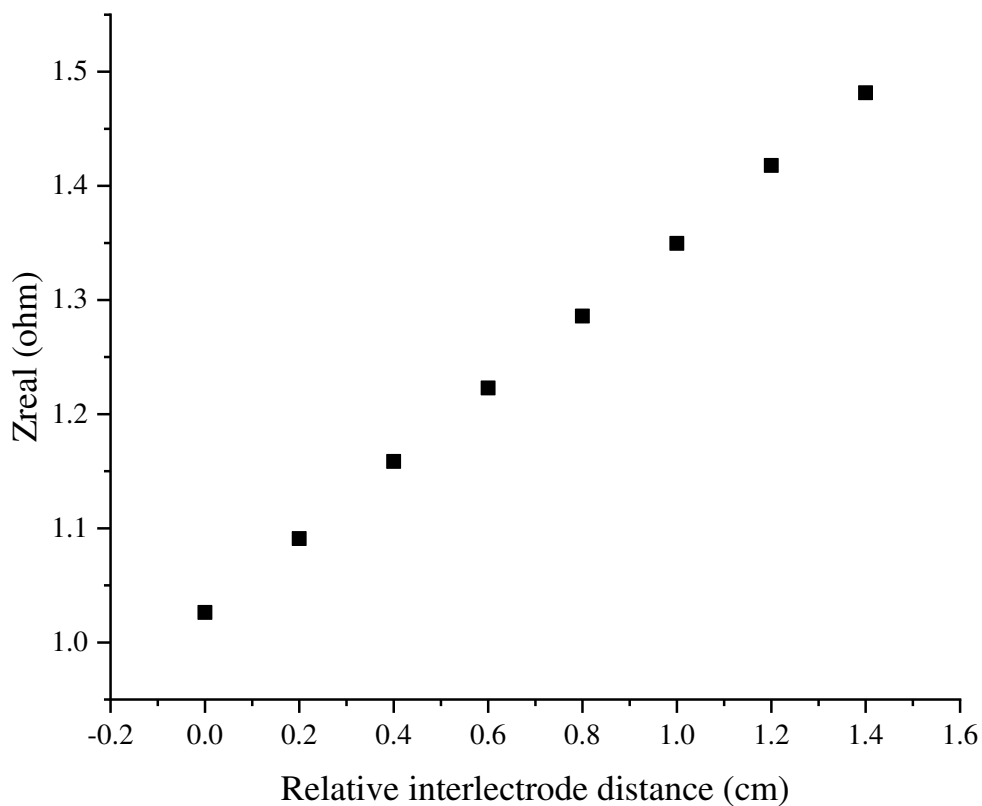


Figure 4-13 The real part for the cell impedance determined when the imaginary part equals zero for LiF at 960 °C

Table 4-1 Measured LiF electrical conductivity compared with the literature data for validation

Temperature, t (°C)	Electrical conductivity (measured), κ ($\text{ohm}^{-1} \text{cm}^{-1}$)	Electrical conductivity (literature), κ ($\text{ohm}^{-1} \text{cm}^{-1}$)	Relative deviation (%)
900	8.881	8.801	0.909
940	8.917	8.992	-0.831
980	9.201	9.142	0.643

4.4.3 NdF₃-LiF electrical conductivity measurement results and discussion

The electrical conductivities of the NdF₃-LiF system are investigated and the scope of research in terms of compositions and temperatures ranges for the electrolytes are listed as in Table 4-2.

Table 4-2 Investigated compositions and temperature ranges for NdF₃-LiF electrolytes

NdF ₃ weight percentage, c_{NdF_3} (wt %)	Liquidus Temperature, T_m (°C)	Test temperature range (°C)
70	757	950-1050
80	886	950-1050
85	973	975-1050

The EIS results are presented in the Nyquist plot form where the impedances of the conductance cell at different frequencies are broken down into the real part (x-axis) and the imaginary part (y-axis). A typical plot is depicted in Figure 4-14. As the electrode is lifted by 2 mm each time and interelectrode spacing increases, the impedance of the cell increases accordingly. When the imaginary part of the impedance equals zero, the real part ($Z_{cell}(Z'' = 0)$) represents the resistance of the cell. The relationship between $Z_{cell}(Z'' = 0)$ and the relative electrode distance is linear (Figure 4-15). The values of $(\frac{dZ_{cell}}{dl})_{Z''=0}$ are obtained as the slope of the fitted line. As a result, the specific electrical conductivity of the electrolyte is determined based on Equation (4.1) while the term $\frac{dG}{dl}$ is calibrated with LiF of which the values for the specific electrical conductivities are known.

$$\kappa = \left(\frac{dZ_{cell}}{dl}\right)_{Z''=0}^{-1} \frac{dG}{dl} \quad (4.1)$$

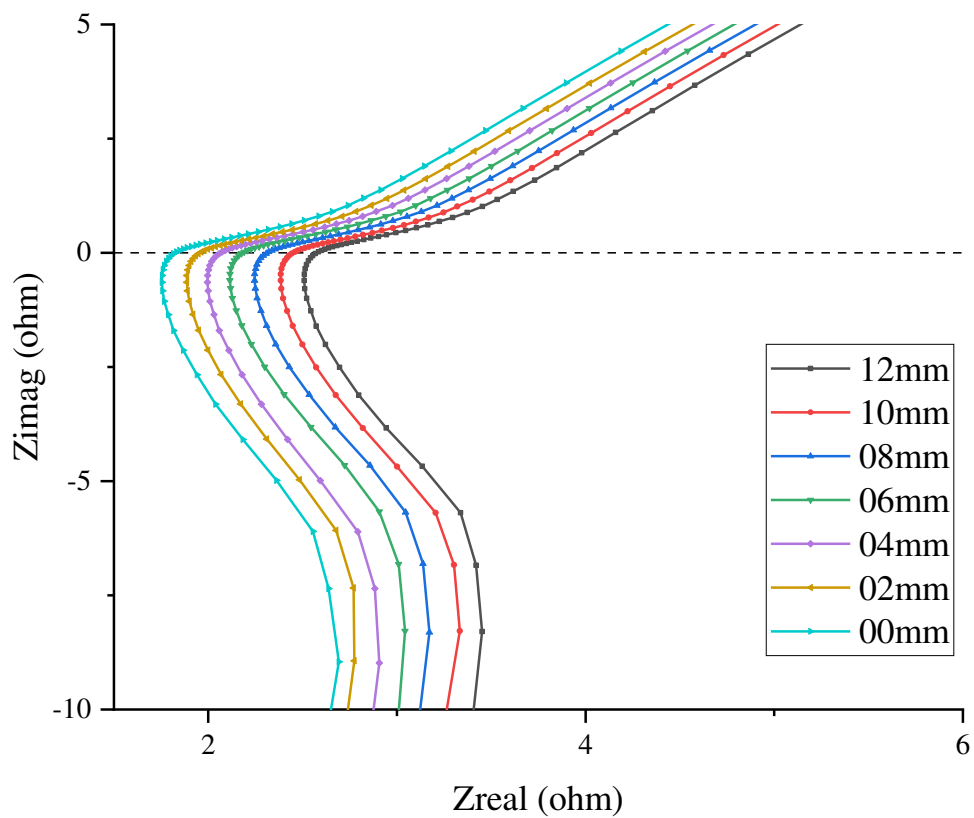


Figure 4-14 Nyquist plot for the EIS results of NdF₃-LiF with increasing interelectrode spacing:
 c_{NdF_3} =85wt%, 975°C

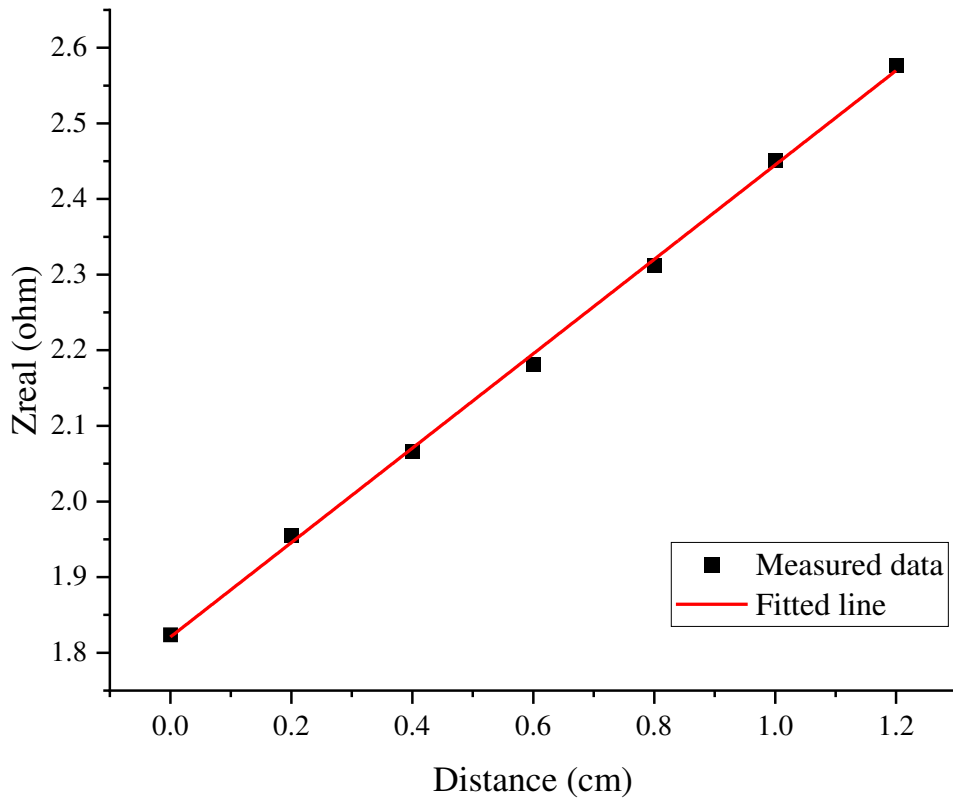


Figure 4-15 Linear relationship between $Z_{cell}(Z'' = 0)$ and the relative electrode distance:
 $c_{NaF_3}=85\text{wt}\%$, 975°C

The molar electrical conductivity, Λ_m , is calculated according to the following equation:

$$\Lambda_m = \kappa V_m \quad (4.2)$$

where V_m is the molar volume of the salts.

The molar volume (V_m) of the molten salt is calculated based on the following equation:

$$V_m = \frac{M}{\rho} \quad (4.3)$$

where V_m is in $\text{cm}^3 \text{mole}^{-1}$, M is the molar mass of the salt in g mole^{-1} , and ρ is the density of the salt in g cm^{-3} .

The pertinent values for the salts in this investigation are listed in Table 4-3. The density values are determined according to Equation (4.4) which is derived by using the data reported by Hu and coworker (Hu, Wang et al. 2010).

$$\rho = -6.53212 \times 10^{-4} c_{NdF_3}^2 - 0.06987 c_{NdF_3} + 1.31265 \times 10^{-5} T^2 \quad (4.4)$$

$$- 0.05297T + 1.69004 \times 10^{-4} c_{NdF_3} T + 43.14013$$

Table 4-3 Pertinent parameters for the NdF₃-LiF salt system

Temperature, t (°C)	NdF ₃ weight percentage, c_{NdF_3} (wt%)	NdF ₃ molar percentage, X_{NdF_3} (mole%)	Molar mass, M (g mole ⁻¹)	Density, ρ (g cm ⁻³)	Molar volume, V_m (cm ³ mole ⁻¹)
950	70	23.1	66.473	4.367	15.222
975	70	23.1	66.473	4.149	16.020
1000	70	23.1	66.473	3.948	16.836
1025	70	23.1	66.473	3.764	17.662
1050	70	23.1	66.473	3.595	18.488
950	80	34.0	85.576	4.756	17.995
975	80	34.0	85.576	4.580	18.683
1000	80	34.0	85.576	4.422	19.355
1025	80	34.0	85.576	4.279	19.999
1050	80	34.0	85.576	4.153	20.606
975	85	42.2	99.936	4.747	21.053
1000	85	42.2	99.936	4.609	21.682
1025	85	42.2	99.936	4.488	22.268
1050	85	42.2	99.936	4.383	22.801

The specific electrical conductivities and the molar electrical conductivities of the salts for the NdF₃-LiF system are determined and listed in Table 4-4.

Table 4-4 Electrical conductivities of the NdF₃-LiF salts determined in this research

NdF ₃ weight percentage, c_{NdF_3} (wt%)	Temperature, t (°C)	Specific electrical conductivity, κ (ohm ⁻¹ cm ⁻¹)	Standard error of κ , $\varepsilon(\kappa)$ (ohm ⁻¹ cm ⁻¹)	Molar electrical conductivity, Λ_m (ohm ⁻¹ cm ² mole ⁻¹)
70	950	5.551	0.051	84.496
70	975	5.662	0.052	90.704
70	1000	5.773	0.053	97.199
70	1025	5.987	0.055	105.736
70	1050	6.081	0.056	112.428
80	950	4.554	0.042	81.945
80	975	4.756	0.044	88.857
80	1000	4.885	0.045	94.542
80	1025	5.050	0.047	100.997
80	1050	5.247	0.048	108.109
85	975	4.380	0.040	92.215
85	1000	4.567	0.042	99.031
85	1025	4.730	0.044	105.326
85	1050	4.908	0.045	111.918

The measured specific electrical conductivities in this investigation are presented as a function of temperature with regard to various compositions as in Figure 4-16. As shown in the figure, the specific electrical conductivity increases with the increase of temperature and with more percentage of NdF₃ added into the salt, the specific electrical conductivity decreases.

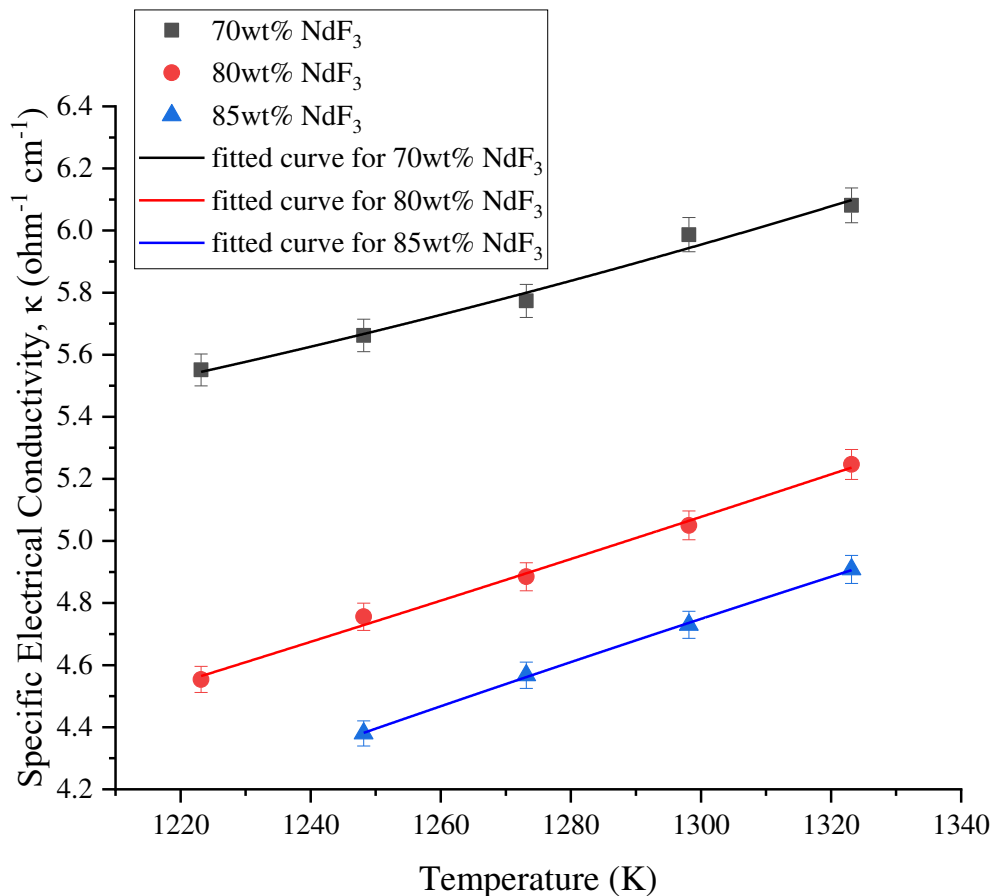


Figure 4-16 Temperature dependence of the specific electrical conductivity of molten fluorides (NdF₃-LiF): 70 wt% NdF₃, 80 wt% NdF₃ and 85 wt% NdF₃

A series of temperature-dependent equations are proposed regarding three compositions with the form of Equation (4.5). The fitted curves are shown in Figure 4-16 and the analysis results for the corresponding coefficients are presented in Table 4-5. Figure 4-17 indicate that the values calculated with Equation (4.5) are consistent with the measured results due to low deviations.

$$\kappa = A + BT + CT^2 \quad (4.5)$$

Table 4-5 Second order series analysis of the electrical conductivity data for the molten NdF₃-LiF system: 70 wt% NdF₃, 80 wt% NdF₃ and 85 wt% NdF₃

NdF₃ weight percentage, c_{NdF_3} (wt%)	A, intercept	Standard error for A, $\varepsilon(A)$	B	Standard error for A, $\varepsilon(B)$	$C \times 10^6$	Standard error for C, $\varepsilon(C) \times 10^6$	Adj. R-Square	Temperature range, °C
70 wt%	12.84153	25.83356	-0.0166	0.04063	8.69318	15.9651	0.97111	950 - 1050
80 wt%	-0.55277	17.75409	0.00184	0.02793	1.91587	10.9805	0.99068	950 - 1050
85 wt%	-10.71012	12.08717	0.0169	0.01882	-3.85616	7.3238	0.99836	975 - 1050

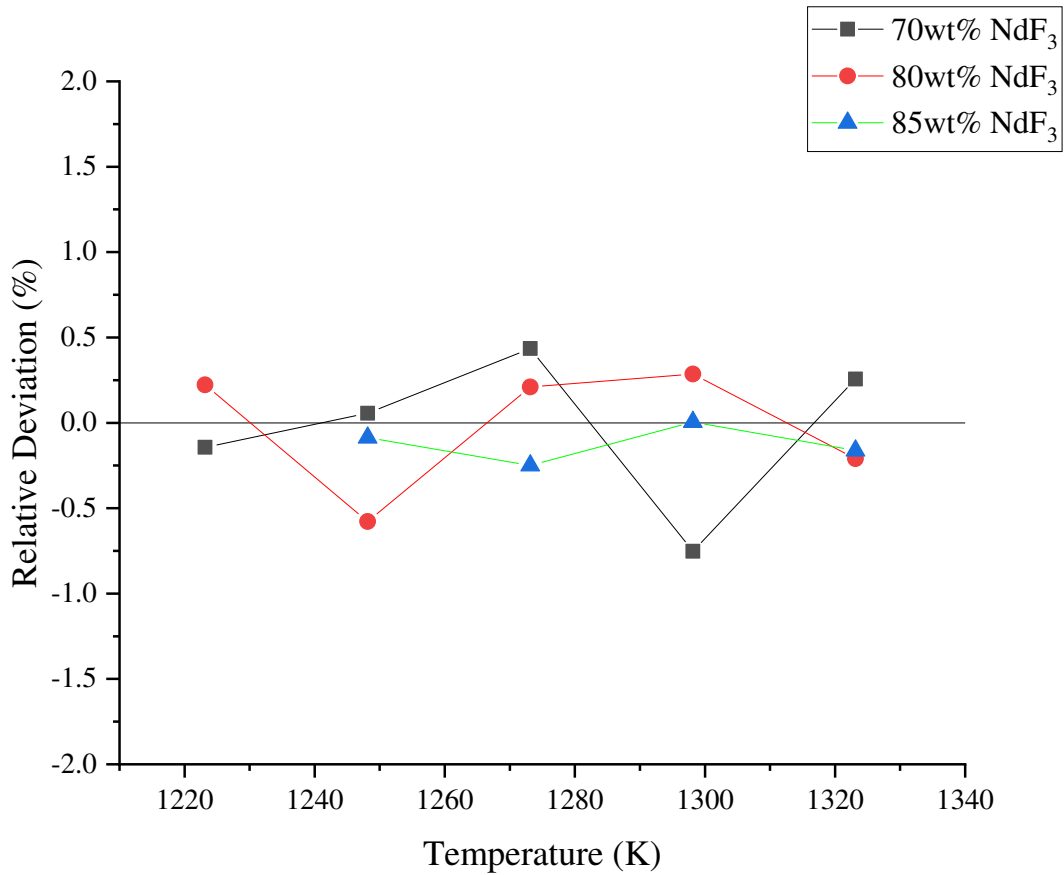


Figure 4-17 Relative deviations for calculated data by Equation (4.5) compared to the measured data

Furthermore, as the specific electrical conductivity is the function of temperature and composition, it can be expressed in the following form of the following equation (Equation (4.6)). The 3D plot for the equation is shown in Figure 4-18 and the relevant coefficients are listed in Table 4-6.

$$\kappa = A_1 \times T^2 + A_2 \times T + B_1 \times c_{NdF_3}^2 + B_2 \times c_{NdF_3} + C_1 \times c_{NdF_3} \times T + D_1 \quad (4.6)$$

where the weight percentage of NdF₃, c_{NdF_3} , is in wt% and temperature, T, is in Kelvin.

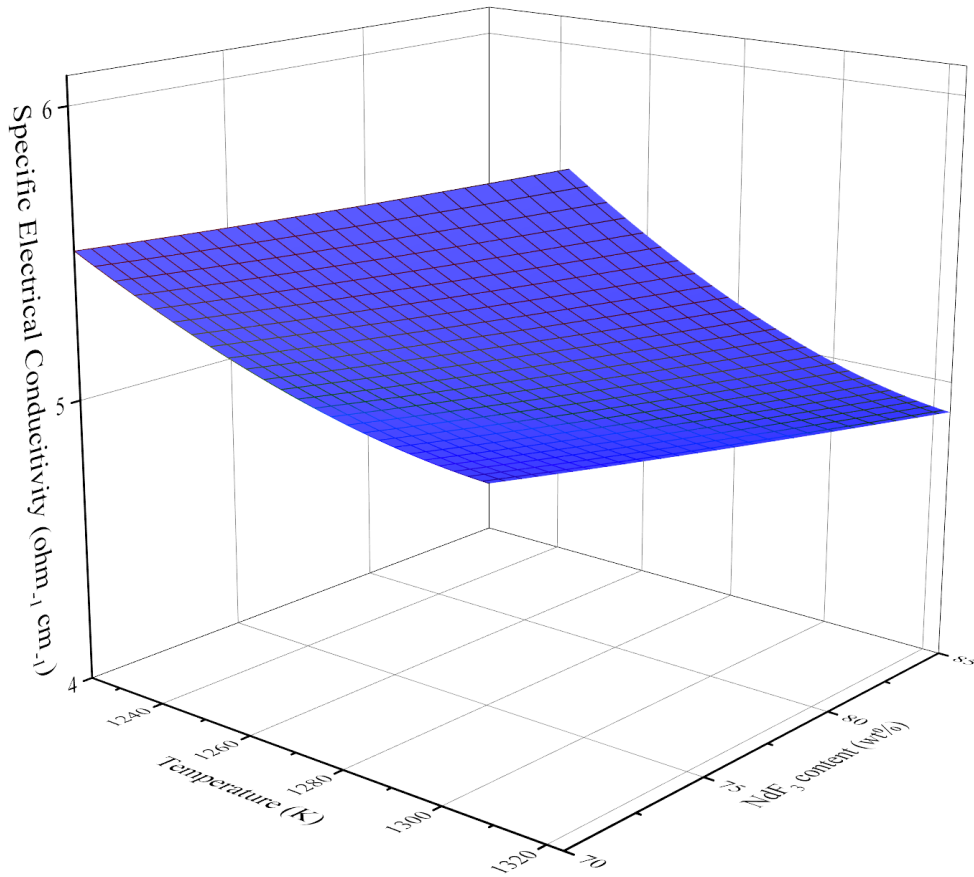


Figure 4-18 3D plot for the specific electrical conductivity of the $\text{NdF}_3\text{-LiF}$ salt system with Equation (4.6)

Figure 4-19 shows the relative deviations of the calculated values for the specific electrical conductivity with Equation (4.6) as opposed to the measured ones. The results demonstrate a good prediction is achieved by the equation because a high correlation is achieved and the deviation is within 1%.

Table 4-6 Coefficient values for Equation (4.6) showing the specific electrical conductivity of $\text{NdF}_3\text{-LiF}$ salts as a function of temperature and composition

	Value	Standard error
A_1	3.13E-06	6.62E-06
A_2	-0.00942	0.01651
B_1	0.00156	2.88E-04
B_2	-0.4526	0.05553
C_1	1.00E-04	3.31E-05
D_1	27.83054	10.82288
Adj. R-Square	0.99816	

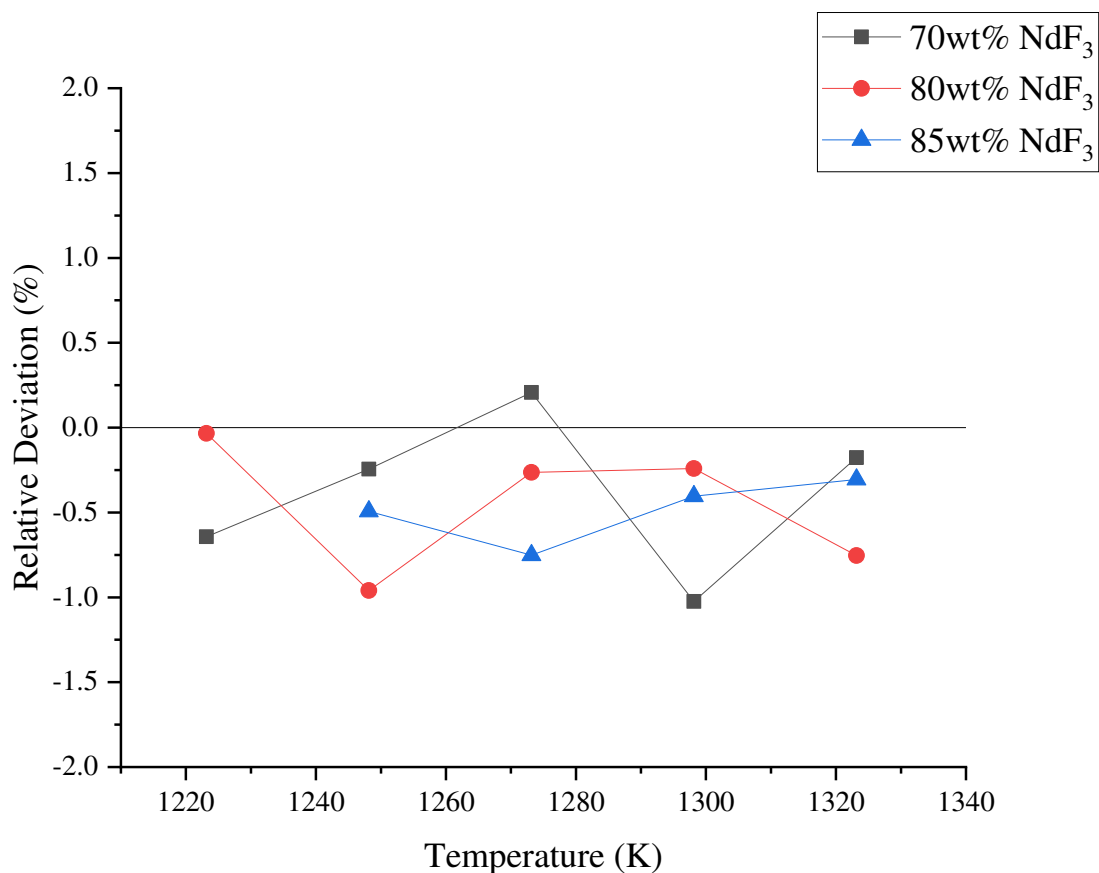


Figure 4-19 Relative deviations for calculated data by Equation (4.6) compared to the measured data

The specific electrical conductivity results are fitted in the Arrhenius equation form with least square regression analysis as indicated below (Figure 4-20):

$$\ln \kappa = D + \frac{E}{T} \quad (4.7)$$

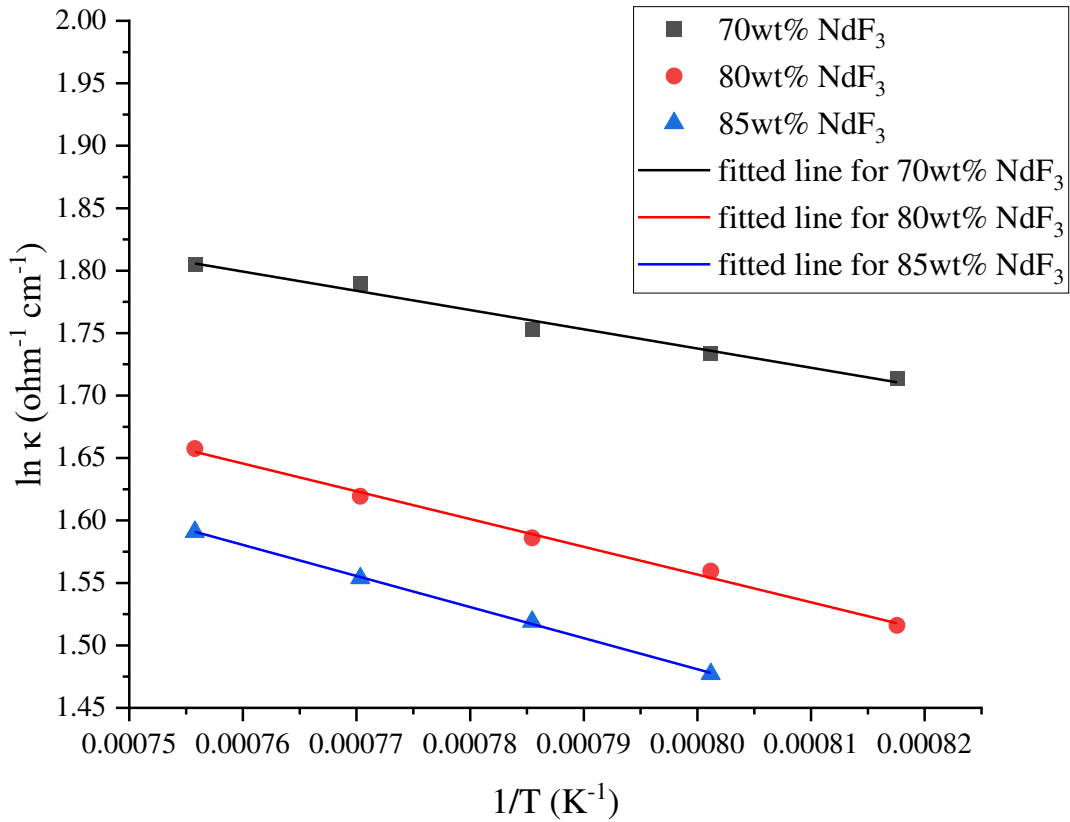


Figure 4-20 Arrhenius form analysis for specific electrical conductivity of the NdF₃-LiF system: 70 wt% NdF₃, 80 wt% NdF₃ and 85 wt% NdF₃

Table 4-7 Coefficients and statistics analysis in Arrhenius form (Equation (4.7)) for the specific electrical conductivity of the NdF₃-LiF system: 70 wt% NdF₃, 80 wt% NdF₃ and 85 wt% NdF₃

NdF ₃ weight per centage, c_{NdF_3} (wt%)	D, intercept	$\epsilon(D)$, standard error for D	E, slope	$\epsilon(E)$, standard error for E	Adj. R-Square
70	2.96966	0.09312	-1539.9818	118.41583	0.97676
80	3.33418	0.0701	-2221.82284	89.14756	0.99359
85	3.47158	0.03597	-2488.32597	46.21624	0.99897

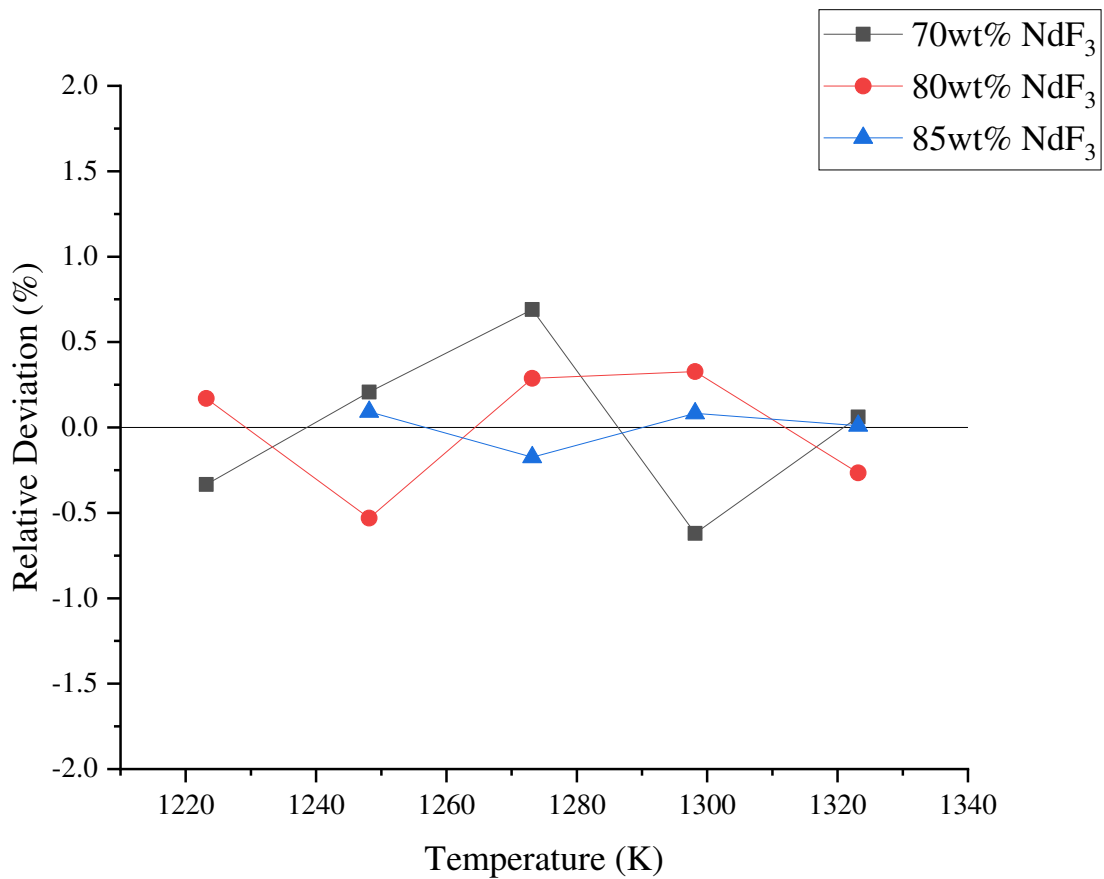


Figure 4-21 Relative deviations for calculated data by Equation (4.7) compared to the measured data

The analysis data with regard to different compositions are listed in Table 4-7. Figure 4-21 shows the Arrhenius equations have high correlations with the measured data. The opposite of the slope values, $-E$, are considered the activation energies (E_a) for the conductivity of the salts. The activation energy for the conductivity increases with the NdF_3 content in the salt. The activation energies for the $\text{NdF}_3\text{-LiF}$ with the NdF_3 content of 70 wt%, 80 wt% and 85 wt% are $1540.0 \text{ kJ mole}^{-1}$, $2221.9 \text{ kJ mole}^{-1}$, and $2488.3 \text{ kJ mole}^{-1}$.

Specific electrical conductivity represents the electrical current carrying capacity of a fixed volume of melt and is subjected to the impact of changes in density and electrical mobilities of the ions and that molar electrical conductivity studies a fixed number of chemical entities. But from a theoretical standpoint it is more valuable to study the *molar* electrical conductivity (Kim and Sadoway 1992).

Molar electrical conductivity results are presented in Figure 4-22 as a function of temperature and the results illustrate a linear relationship between the molar electrical conductivity and temperature for the compositions of interested. Least square regression analysis results are shown in Table 4-8 with the coefficients for the fitted linear equation series with the form as the following:

$$\Lambda_m = G + H \times T \quad (4.8)$$

The statistics for linear fit with the equations indicate a good correlation but neither the intercept nor the slope shows an obvious relationship with the change of compositions.

Similar with the aforementioned analysis on the specific electrical conductivity data which is fitted with the Arrhenius equation form, the molar electrical conductivity results are treated in the form of the following equation:

$$\ln \Lambda_m = I + \frac{J}{T} \quad (4.9)$$

The coefficients, I and J, are listed in Table 4-8 and the statistics results show that the correlation of the equation is high. However, no direct indication of a trend for the equation to change with the change of the NdF_3 content.

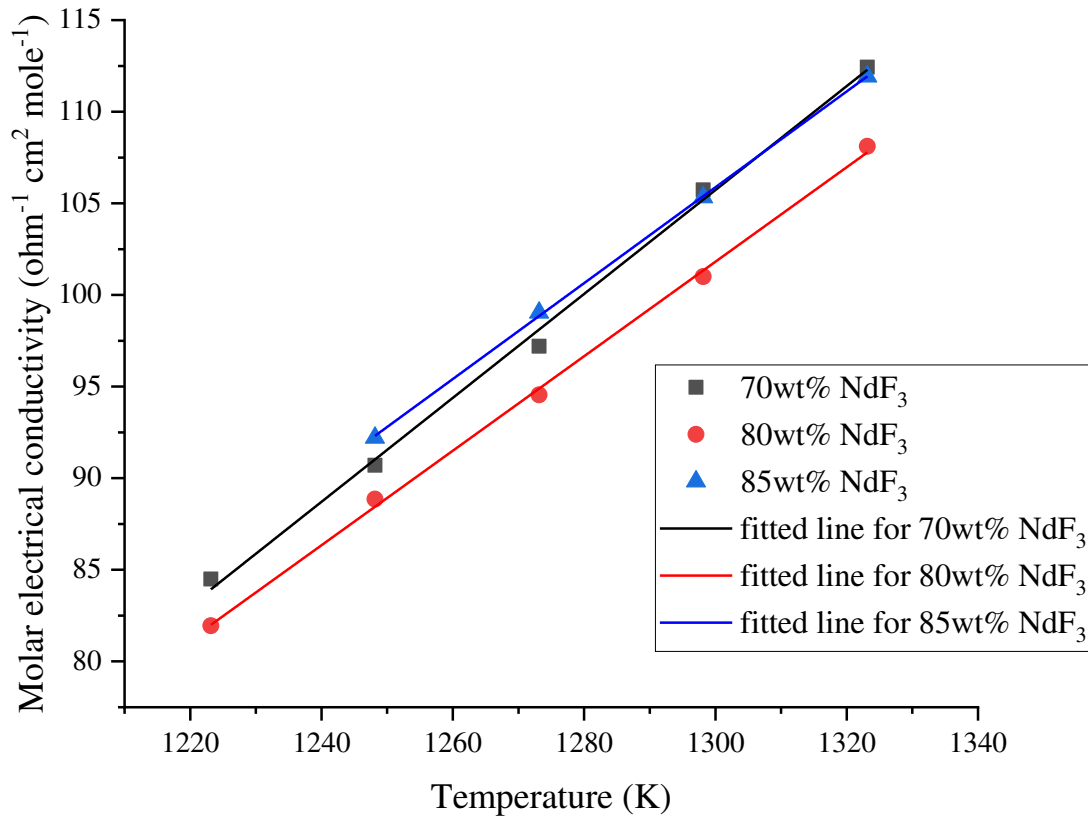


Figure 4-22 Molar electrical conductivity of NdF_3 -LiF salts as a function of temperature: 70 wt% NdF_3 , 80 wt% NdF_3 and 85 wt% NdF_3

Table 4-8 Coefficients and statistics analysis in the linear fit (Equation (4.8)) for the molar electrical conductivity of the NdF₃-LiF system: 70 wt% NdF₃, 80 wt% NdF₃ and 85 wt% NdF₃

NdF ₃ weight per centage, c_{NdF_3}	G, intercept	$\epsilon(G)$, standard error for G	H, slope	$\epsilon(H)$, standard error for H	Adj. R-Square
70	-262.9252	11.6058	0.28358	0.00911	0.99588
80	-233.41554	6.68367	0.25787	0.00525	0.99835
85	-234.22102	3.49709	0.26161	0.00272	0.99968

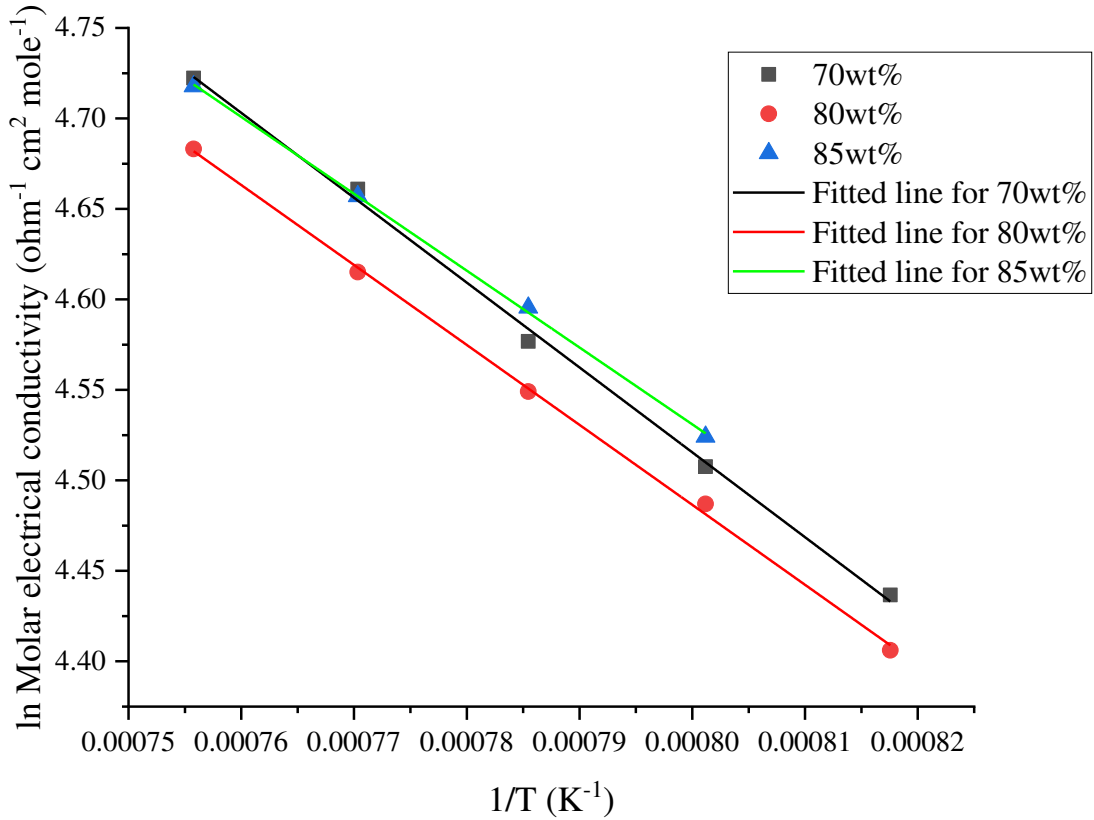


Figure 4-23 Arrhenius form analysis for the molar electrical conductivity of NdF₃-LiF salts: 70 wt% NdF₃, 80 wt% NdF₃ and 85 wt% NdF₃

Table 4-9 Coefficients and statistics analysis for Arrhenius form equations (Equation (4.9)) in terms of the molar electrical conductivity of NdF₃-LiF salts: 70 wt% NdF₃, 80 wt% NdF₃ and 85 wt% NdF₃

NdF ₃ weight per centage, C_{NdF_3}	I, intercept	$\epsilon(I)$, standard error for I	J, slope	$\epsilon(J)$, standard error for J	Adj. R-Square
70	8.26706	0.09592	-4689.46561	121.97542	0.9973
80	8.02091	0.06719	-4418.03491	85.4426	0.99851
85	7.92812	0.05535	-4246.45298	71.11649	0.99916

Figure 4-24 presents the molar electrical conductivity results with the relationship between the natural logarithm of molar electrical conductivity and that of charge density that is defined as

$$\rho_q = \frac{Fz}{V_m} \quad (4.10)$$

where F is Faraday constant, and z is the charge of the anions in mole per mole of relevant chemicals in the salt.

In the figure, the color-coded symbols represent the data at different temperatures regardless the NdF₃ in the salts. The symbols with the same NdF₃ content are connected and fitted in a straight line. As shown in the diagram, the molar electrical conductivity increases with temperature while the charge density decreases as temperature increases. An interesting finding is that the symbols representing the same temperatures are distributed with no obvious trend as the NdF₃ changes but they are located in the same block region in the diagram. The dots for the same NdF₃ content fits in a straight line and it can be expressed as the following equation:

$$\ln \Lambda_m = \alpha + \beta \times \ln \rho_q \quad (4.11)$$

where Λ_m is the molar electrical conductivity in $\text{ohm}^{-1} \text{cm}^2 \text{mole}^{-1}$, ρ_q is the charge density in C cm^{-3} , and α and β represent, respectively, the intercept and the slope for the equations, of which the values are listed in Table 4-10.

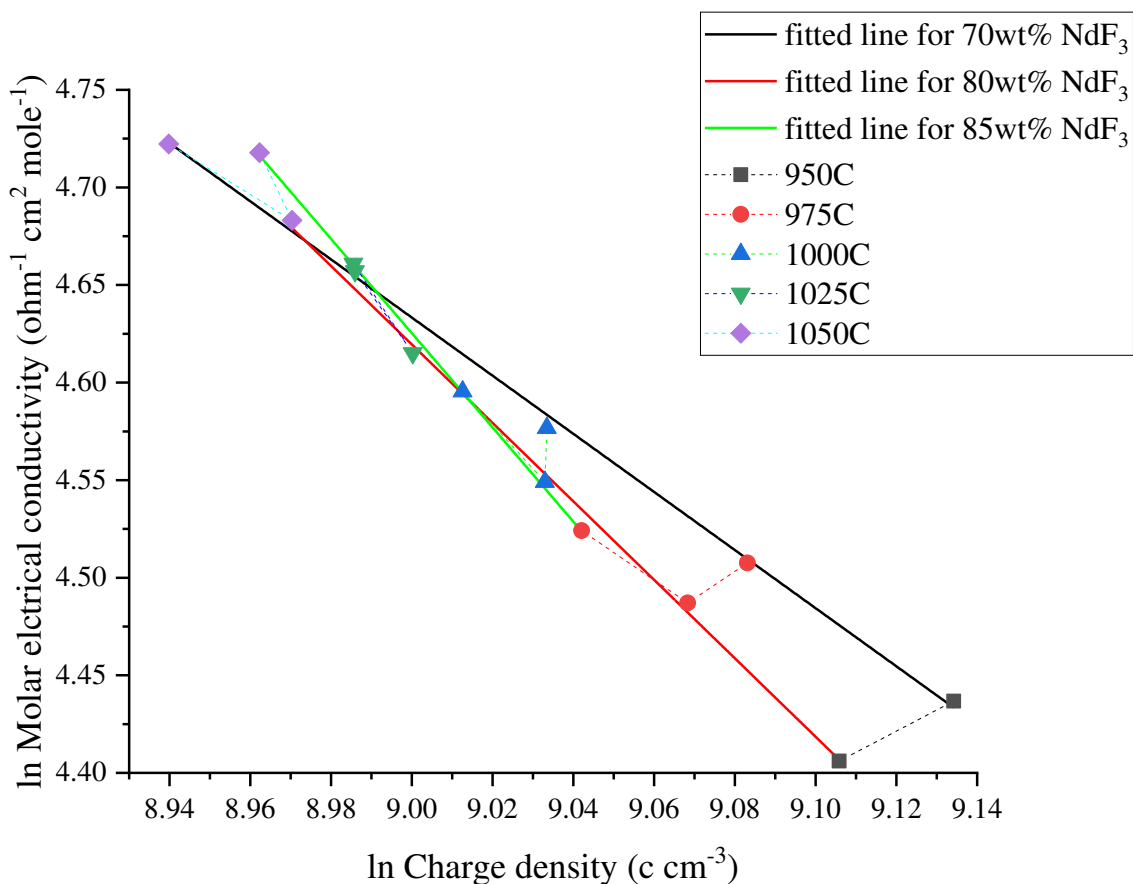


Figure 4-24 Analysis on the relationship between the molar electrical conductivity and the charge density for $\text{NdF}_3\text{-LiF}$ salts: 70 wt% NdF_3 , 80 wt% NdF_3 and 85 wt% NdF_3

It is shown that within the investigated temperature and content ranges, the relationship between the molar electrical conductivity and the charge density is independent of temperature but varies with the change of NdF_3 contents. The intercept, α , is the natural log of the molar electrical conductivity when the change density is unity, and the slope, β , can be interpreted as a

coefficient which determines how the molar electrical conductivity responds to the change in the charge density of the salt.

Table 4-10 Coefficients and statistics analysis for the fitted equations (Equation (4.11)): 70 wt% NdF₃, 80 wt% NdF₃ and 85 wt% NdF₃

NdF ₃ weight per centage, c_{NdF_3}	α , intercept	$\epsilon(\alpha)$, standard error for α	β , slope	$\epsilon(\beta)$, standard error for β	Adj. R-Square
70	18.03713	0.33513	-1.48931	0.03709	0.99752
80	22.71443	0.41518	-2.01054	0.04595	0.99791
85	26.35706	0.28739	-2.41464	0.03193	0.99948

It is found that the intercept, α , and the slope, β , both have a linear relationship with the molar content of NdF₃ as shown in Figure 4-25 and they can be determined by the following equations:

$$\alpha = 7.9589 + 0.43562 X_{NdF_3} \quad (4.12)$$

$$\beta = -0.36868 - 0.04845 X_{NdF_3} \quad (4.13)$$

This suggests that because the salt structures are similar among the salt compositions considered, the molar mass plays an important role in determining how the molar electrical conductivity would respond to the changes in the charge density of the salt.

Considering that

$$\Lambda_m = \frac{\kappa M}{\rho} \quad (4.14)$$

and

$$\rho_q = \frac{Fz\rho}{M} \quad (4.15)$$

Equation (4.11) can be rewritten in the form of the following equation:

$$\kappa = \kappa_u \left(\frac{\rho}{\rho_u} \right)^\gamma \quad (4.16)$$

where κ_u is the electrical conductivity when the charge density equals unity, of which the value is determined by

$$\ln \kappa_u = \alpha - \ln Fz \quad (4.17)$$

ρ_u is the density when the charge density equals unity, of which the value is

$$\rho_u = \frac{M}{Fz} \quad (4.18)$$

and γ equals $\beta+1$.

Given that

$$\beta = \frac{d \ln \Lambda_m}{d \ln \rho_q} = \frac{d \ln (\kappa V_m)}{d \ln \left(\frac{Fz}{V_m} \right)} = \frac{d \ln \left(\kappa \frac{M}{\rho} \right)}{d \ln \left(\frac{Fz\rho}{M} \right)} = \frac{d \ln \kappa}{d \ln \rho} - 1$$

we have

$$\gamma = \frac{d \ln \kappa}{d \ln \rho} \quad (4.19)$$

Therefore, an equation using the density of the salt system considered to estimate the specific electrical conductivity is determined in the form of Equation (4.16) and the relative deviations are plotted in Figure 4-26.

It is also found that Equation (4.16) is suitable for other salt systems (Table 4-12) with high correlation coefficients. The data for more salt systems not listed in the table shows similar feature and fits in Equation (4.16).

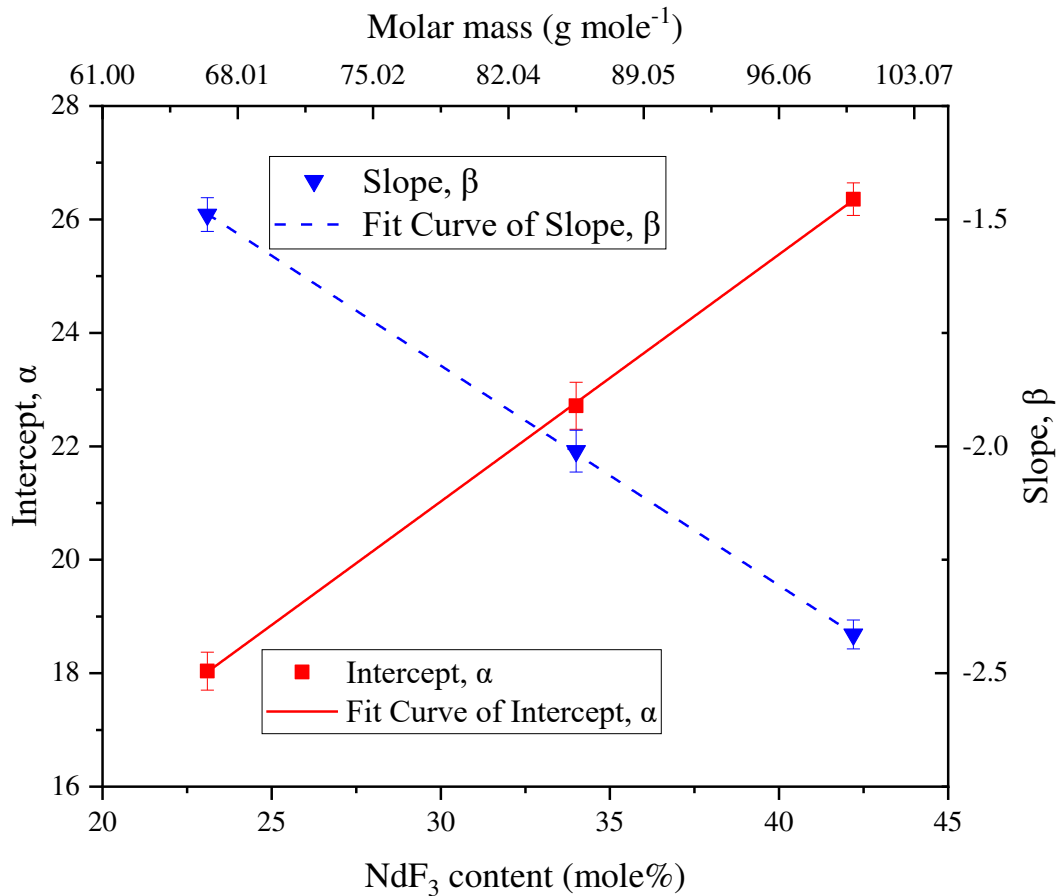


Figure 4-25 Changes of coefficients α and β from Equation (4.11) with the increase of NdF_3 content in the $\text{NdF}_3\text{-LiF}$ salt

Table 4-11 Linear analysis for the intercept, α , and the slope, β , for Equation (4.11) with regard to changing molar percentages of NdF_3 in the salt

	ν , intercept	$\varepsilon(\nu)$, standard error for ν	θ , slope	$\varepsilon(\theta)$, standard error for θ	Adj. R-Square
Intercept, α	7.9589	0.1223	0.43562	0.00349	0.99987
Slope, β	-0.36868	0.01183	-0.04845	3.37273E-4	0.9999

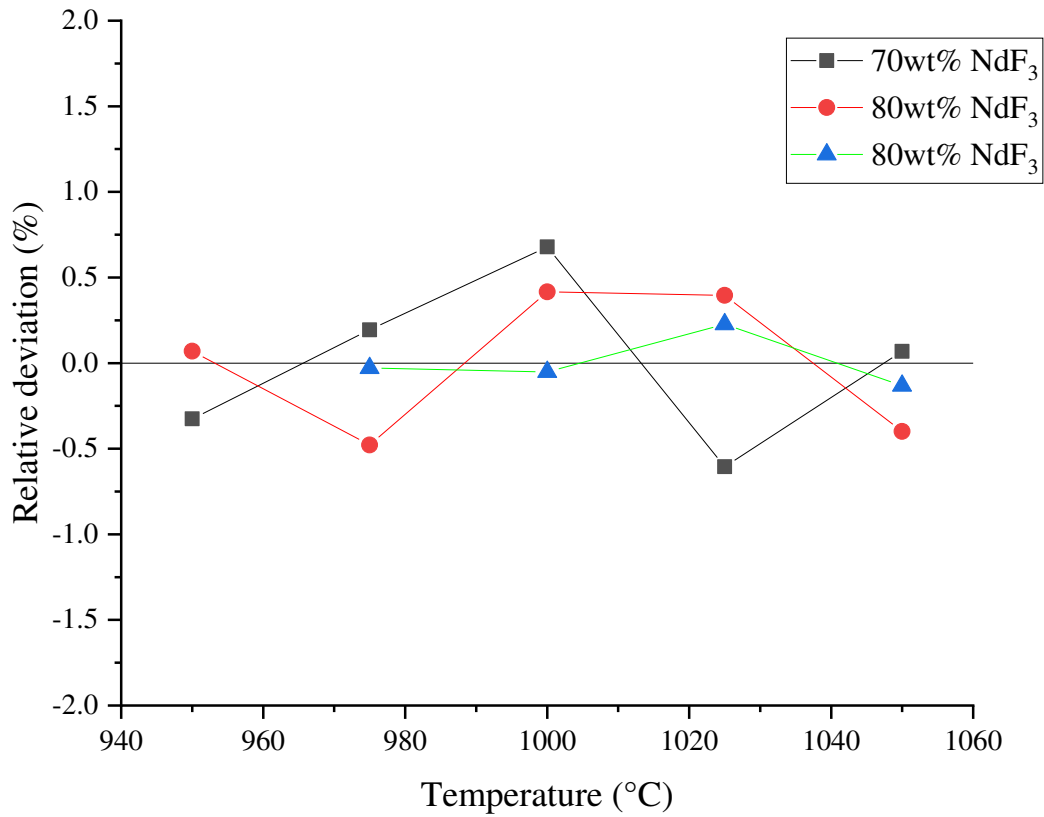


Figure 4-26 Relative deviations for calculated data by Equation (4.6) compared to the measured data

Consider the most investigated chlorides of alkaline group metals (NaCl, KCl, RbCl and CsCl) which share similar chemical properties and salt structures, the coefficients, $\ln \kappa_u$ and β , are plotted as the changes of molar mass for the chemicals. Interestingly, both $\ln \kappa_u$ and β fit in straight lines with changing the molar masses (Figure 4-27 and Figure 4-28) and the correlation factors for both are very high (Table 4-13).

Table 4-12 Coefficients for Equation (4.16) for different chemicals using data from (Janz, Janz et al. 1968)

Chemicals	κ_u	ρ_u	β	Adj. R-Square	Temperature range (K)
NaF	1.96270x107	4.35178x10-4	-2.807970	0.99987	1270-1420
KF	4.04364x108	6.02132x10-4	-3.300590	0.99968	1130-1290
NaCl	1.78913x107	6.05794x10-4	-2.963660	0.99722	1080-1290
CaCl2	5.92092x1031	5.75115x10-4	-9.840790	0.99825	1060-1240
KCl	1.79946x108	7.72659x10-4	-3.401770	0.99693	1060-1200
RbCl	4.39677x1011	1.25346x10-3	-4.522910	0.99352	990-1220
CsCl	2.43438x1015	1.74504x10-3	-5.782540	0.99221	940-1170
SrCl2	8.76448x1026	8.21371x10-4	-8.565380	0.99893	1160-1310
BaCl2	2.24787x1025	1.07892x10-3	-8.219190	0.99929	1240-1360
AgCl	1.66746x1013	1.48541x10-3	-4.592570	0.98554	730-1020
LaCl3	2.70380x1025	8.47455x10-4	-8.059200	0.98686	1140-1260
CeCl3	7.62066x1024	8.51600x10-4	-7.935900	0.98957	1100-1210
MnCl2	6.05835x1020	6.51915x10-4	-6.794460	0.99971	930-1130
CdCl2	3.90574x1016	9.49889x10-4	-5.593070	0.99404	840-1070
NaBr	1.06931x109	1.06638x10-3	-3.563060	0.99832	1030-1220
KBr	1.73515x109	1.23346x10-3	-3.787560	0.98638	1020-1200
RbBr	7.73578x1010	1.71426x10-3	-4.384940	0.97987	960-1180
CsBr	1.97449x1017	2.20584x10-3	-6.512410	0.99075	910-1140

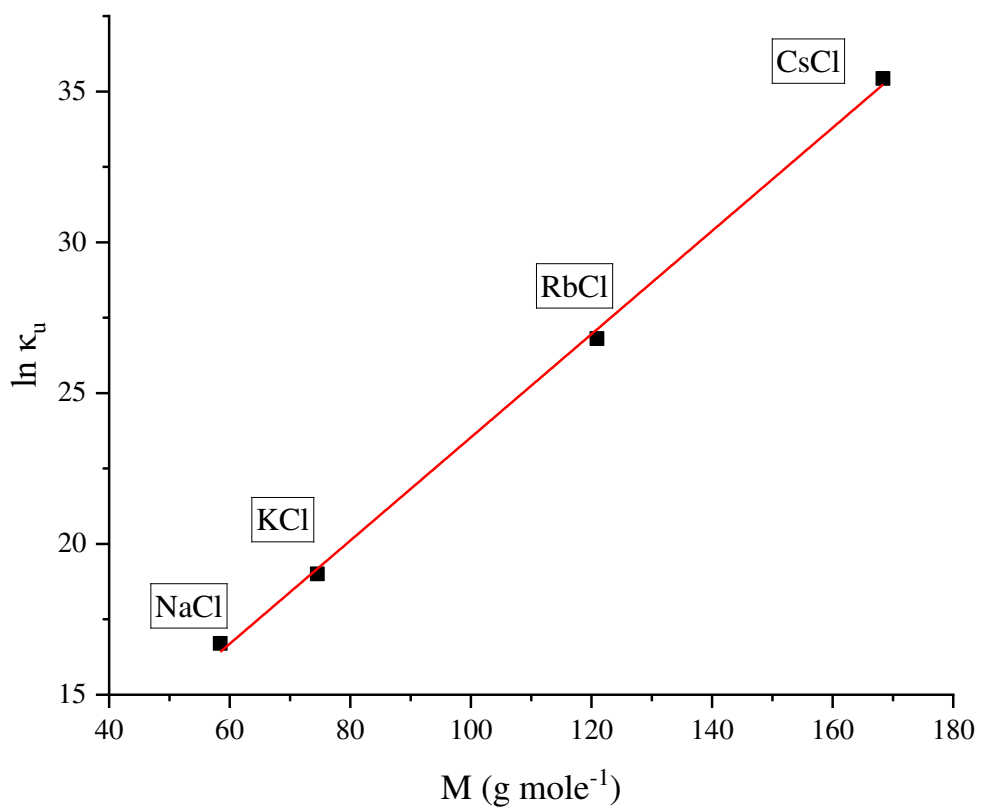


Figure 4-27 Coefficient $\ln \kappa_u$ changes with increasing molar masses for NaCl, KCl, RbCl and CsCl

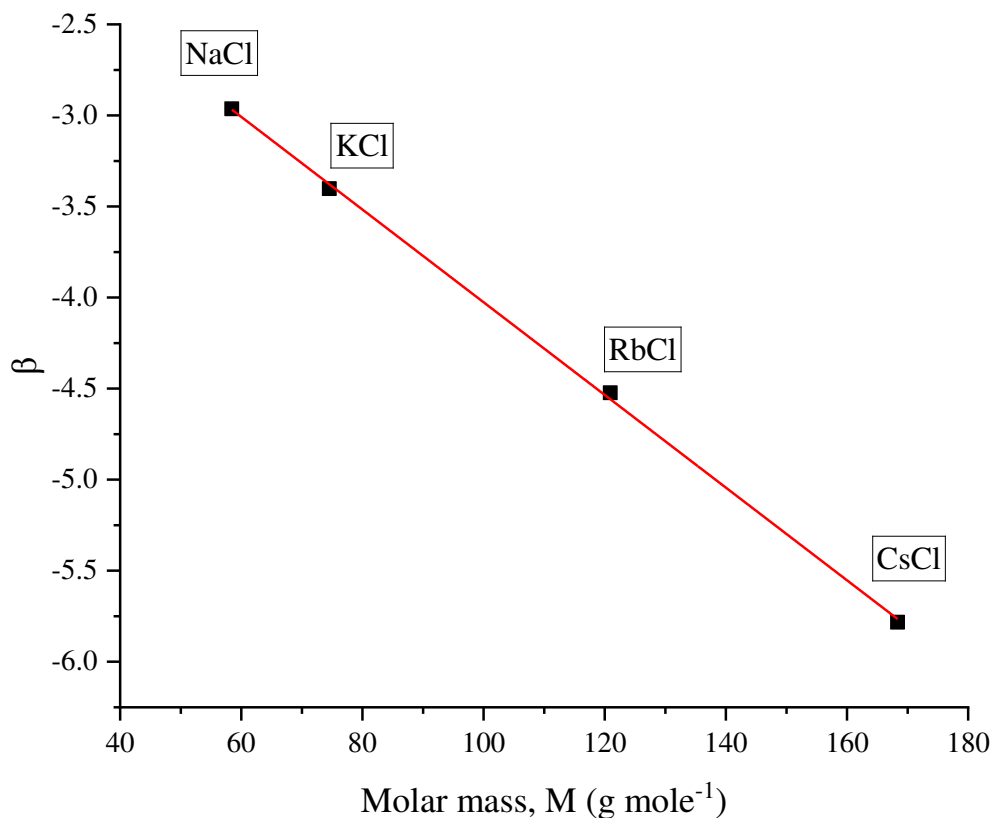


Figure 4-28 Coefficient β changes with increasing molar masses for NaCl, KCl, RbCl and CsCl

Table 4-13 Coefficient and statistics analysis for $\ln \kappa_u$ and β with changing molar masses: NaCl, KCl, RbCl and CsCl

	ν , intercept	$\varepsilon(\nu)$, standard error for ν	θ , slope	$\varepsilon(\theta)$, standard error for θ	Adj. R-Square
$\ln \kappa_u$	6.422700	0.45827	1.71090E-01	0.00402	0.99834
β	-1.480970	0.04349	-2.54500E-02	3.82E-04	0.99933

For the salts discussed insofar, the relationship between the density and the electrical conductivity shows a high correlation with the form of Equation (4.16). With minimum of two

sets of density/electrical conductivity data pairs, the coefficients involved in the equation can be determined. Equation (4.16) can be considered as an empirical equation for one to estimate the value of density or electrical conductivity with that of the other known.

Equation (4.16) can be rewritten as

$$\frac{\ln \kappa - \ln \kappa_u}{\ln \rho - \ln \rho_u} = \frac{d \ln \kappa}{d \ln \rho} \quad (4.20)$$

where $\frac{d \ln \kappa}{d \ln \rho}$ can be determined statistically with minimum of two pairs of data for density and electrical conductivity as constant, and κ_u and ρ_u can be also replaced by the known set of data information as κ_x and ρ_x . Therefore, it further gives

$$\frac{d \ln \kappa}{d \ln \rho} = \text{constant} \quad (4.21)$$

Because the electrical conductivity of molten salts is very difficult to measure, especially for the highly corrosive fluorides, there is limited access to those values in practice. Equation (4.20) enables one as an empirical equation to estimate the electrical conductivities with known density information and gives a reasonably reliable estimation.

4.5 Conclusion

A conductance cell with resistance to high temperature up to 1200 °C (limited by the furnace temperature capability) and corrosive molten fluorides has been constructed to apply measurements to determine the electrical conductivities of molten salts by electrochemical impedance spectroscopy using the Constantly Varying Cell Constant (CVCC) technique. The conductance cell has demonstrated itself to be capable of producing data of high quality under severe conditions.

The electrical conductivities of the molten NdF₃-LiF salt system between 70 wt% NdF₃ and 85 wt% NdF₃ within the range of temperature from 950 °C to 1050 °C have been

systematically measured with the conductance cell. It is found that the specific electrical conductivity of the $\text{NdF}_3\text{-LiF}$ salt increases with temperature and the addition of NdF_3 reduces the electrical conductivity. The electrical conductivities of the salts investigated in this study range from $4.38 \text{ ohm}^{-1} \text{ cm}^{-1}$ to $6.08 \text{ ohm}^{-1} \text{ cm}^{-1}$. A number of statistical equations have been developed to estimate the electrical conductivities in the discussion section and all demonstrate a high correlation with the capability to yield reliable estimation data.

As a favorable composition and temperature condition for the electrowinning practice, the fluoride salt with NdF_3 85 wt% gives at $1050 \text{ }^\circ\text{C}$ the specific electrical conductivity of $4.908 \text{ ohm}^{-1} \text{ cm}^{-1}$ and the molar specific electrical conductivity of $111.918 \text{ ohm}^{-1} \text{ cm}^2 \text{ mole}^{-1}$.

The relationship between \ln molar electrical conductivity ($\ln \Lambda_m$) and \ln charge density ($\ln \rho_q$) for the $\text{NdF}_3\text{-LiF}$ system and it is shown that there is a linear correlation between the two, which is determined by the content of the fluorides and shows independence of temperature. The intercept and the slope of the linear fit vary linearly with changing molar masses. A similar relationship is also found for the chlorides of alkali metals (NaCl , KCl , RbCl and CsCl) in order of increasing molar mass. The main reason for this is likely to be, similar to the $\text{NF}_3\text{-LiF}$ salts with varying NdF_3 content, that the molten salt structures are similar among the alkaline chlorides because of valence electronic similarity. It appears that from Na and K to Rb and then to Cs the increasing atom size results in decreasing mobility of the ions in the salt system.

An empirical equation to estimate the value of the electrical conductivity for a specific molten salt is proposed. It enables one to conduct estimation with density known with reasonably good confidence from a minimum of two density/electrical conductivity value sets.

CHAPTER 5

MATHEMATICAL MODEL DEVELOPMENT OF Nd_2O_3 - NdF_3 - LiF MOLTEN SALT ELECTROLYSIS SYSTEM

5.1 Introduction

Oxide-fluoride molten salt electrolysis is the most commercial technique to produce aluminum and rare earth metals (REMs). In this chapter, we discuss the thermodynamics and kinetics with respect to the neodymium electrolytic process in the Nd_2O_3 - NdF_3 - LiF molten system and then a mathematical model is developed based on the analysis. With the model established, we discuss the impact of various relevant parameters on the optimization of the energy efficiency and the prevention of the generation of perfluorocarbon gases (PFCs). After that, the parameters were discussed for the optimization of the molten salt electrolysis technology. A conclusion is made at the end of the chapter regarding the molten salt system.

5.2 Problem establishment

To develop a mathematical model for the neodymium electro-winning process in the Nd_2O_3 - NdF_3 - LiF molten system at elevated temperature (1050 °C), we consider the configuration of an electrolytic cell as illustrated in Figure 5-1. The cell mainly constitutes a center-located cylindrical cathode made of tungsten, a concentric anode made of graphite against the inner wall of the cell and NdF_3 - LiF molten fluorides with fixed composition. The inner radius of the graphite anode is r_a and the radius of the tungsten cathode is r_c . In a continuous electrolytic process, neodymium oxide is consistently introduced into the fluoride electrolyte at a certain rate while a direct current is imposed on the electrodes through the cell.

The added neodymium oxide is first dissolved into the electrolyte and then diffuses in the form of ions into the bulk solution. When the ions travel through the boundary layers associated

with the electrodes to the electrode surfaces, the chemical reactions occur to produce the metallic neodymium and the gases.

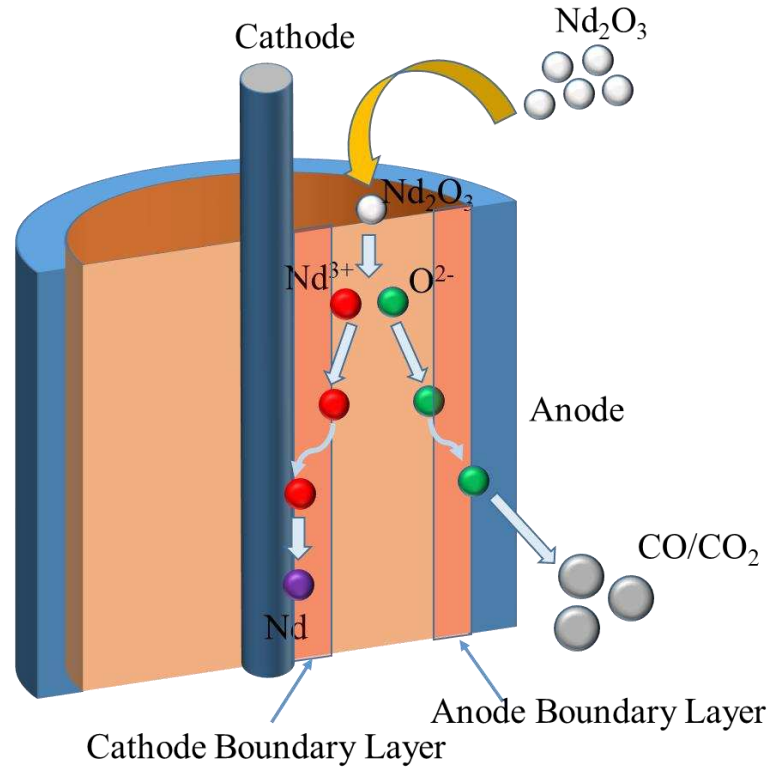
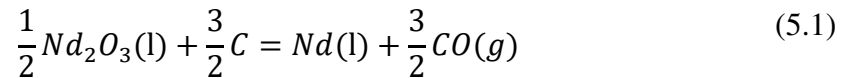
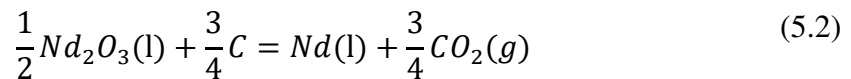


Figure 5-1 Electrolytic process for the neodymium production in the molten fluoride electrolyte

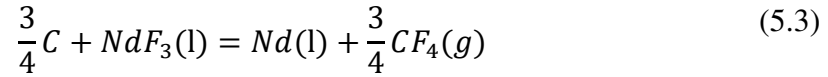
As is known, the process decomposes the dissolved neodymium oxide and produce metallic neodymium with the composition of the electrolyte maintaining fixed. The primary overall reactions involved in the electrolysis process are as follows:



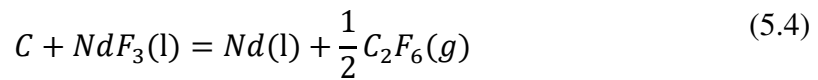
and



Thus the desirable gas products are carbon monoxide and carbon dioxide. However, other components may be decomposed by the electricity when Nd_2O_3 is not sufficiently available at the electrodes and then other gases are observed to be generated such as perfluorocarbon gases (CF_4 , C_2F_6 , etc.). The secondary reactions with perfluorocarbon emission are listed below:



and



The two by-product perfluorocarbon gases (PFCs), tetrafluoromethane (CF_4) and hexafluoroethane (C_2F_6), have a remarkably high greenhouse gas equivalent and have a global warming potential (GWP) of 7,390 and 12,200 (Sekiya and Okamoto 2010), respectively. They are believed to contribute to global warming. In addition to that, the generation of PFCs consumes the supposedly non-reactive fluoride component in the electrolyte and, as a result, makes the process less cost-effective. Therefore, the sustainable electrolysis process requires the prevention of these secondary reactions.

Researches (Stefanidaki, Photiadis et al. 2002, Ambrová, Jurišová et al. 2008, Pshenichny and Omelchuk 2012, Guo, Sun et al. 2016) have shown that the oxygen ions from the rare earth oxide as it dissolves into the electrolyte react with the fluoride component and form complexes. As Stefanidaki and coworkers (Stefanidaki, Photiadis et al. 2002) reported, the dissolved Nd_2O_3 in the NdF_3 - LiF eutectic forms complexes of $\text{NdOF}_x^{(x-1)-}$ as mononuclear compounds and $\text{Nd}_2\text{OF}_{x+3}^{(x-1)-}$ as the binuclear complexes according to Raman spectroscopy observations and also concluded the most reasonable candidates are NdOF_4^{3-} , NdOF_5^{4-} , $\text{Nd}_2\text{OF}_{10}^{6-}$ and $\text{Nd}_2\text{OF}_8^{4-}$.

The dissolution of the neodymium oxide can be expressed with the following reactions:



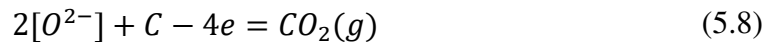
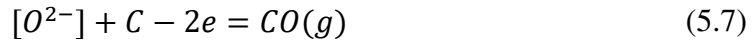
and



where $[O^{2-}]$ represents the corresponding oxygen-carrying ion complexes.

For the primary reactions, the half reactions at the anode and the cathode are, respectively:

(Anode)



(Cathode)



5.3 Thermodynamics Considerations

Thermodynamics is of great importance when it comes to the electrolysis process with chemical reactions involved. We first analyze the possible chemical reactions at the electrolysis conditions and then assess the theoretical decomposition voltage regarding the corresponding reactions.

The possible species generated out of anode half-cell reactions can be CO, CO₂, COF₂, COF, CF₄, C₂F₆, CF₂, and CF. The relevant reactions are listed in Table 5-1 and the corresponding thermodynamics information obtained through HSC Chemistry 8.0 is also included in the table for 1050 °C. In the table, n is the moles of electron transfer involved in the reaction per unit mole of neodymium production, and E^0 is the potentials for the reaction calculated with the Nernst equation.

Table 5-1 Standard Gibbs Free Energies and potentials for Reactions of interest determined by HSC Chemistry 8.0 at 1050°C

Reaction No.	Chemical Reactions	$\Delta G_{1050\text{ }^\circ\text{C}}^0$ (kJ/mole Nd)	n ^b	E^0 ^c (V)
(5.1)	$\frac{1}{2}Nd_2O_3(l) + \frac{3}{2}C = Nd(l) + \frac{3}{2}CO(g)$	350.651	3	-1.211
(5.2)	$\frac{1}{2}Nd_2O_3(l) + \frac{3}{4}C = Nd(l) + \frac{3}{4}CO_2(g)$	396.392	3	-1.369
(5.10)	$\frac{1}{4}Nd_2O_3(l) + \frac{3}{4}C + \frac{1}{2}NdF_3(l)$ $= Nd(l) + \frac{3}{4}COF_2(g)$	622.165	3	-2.149
(5.11)	$\frac{1}{3}Nd_2O_3(l) + C + \frac{1}{3}NdF_3(l)$ $= Nd + COF(g)$	691.925	3	-2.390
(5.3)	$\frac{3}{4}C + NdF_3(l) = Nd(l) + \frac{3}{4}CF_4(g)$	801.467	3	-2.769
(5.4)	$C + NdF_3(l) = Nd(l) + \frac{1}{2}C_2F_6(g)$	866.535	3	-2.994
(5.12)	$\frac{3}{2}C + NdF_3(l) = Nd(l) + \frac{3}{2}CF_2(g)$	1014.494	3	-3.505
(5.13)	$3C + NdF_3(l) = Nd(l) + 3CF(g)$	1669.941	3	-5.769

^a $\Delta G_{1050\text{ }^\circ\text{C}}^0$ is the standard Gibbs free energy for the corresponding reaction at 1050 °C;

^b n is the moles of electron transfer involved in the reaction considering unit mole of neodymium production;

^c E^0 is the potentials for the reaction calculated with the Nernst equation.

In order to determine the thermodynamically stable species at equilibrium and the involved reactions at the electrolysis conditions, a Gibbs free energy minimization is carried out with HSC Chemistry 8.0 given that carbon is excessive. In this evaluation, the input of the carbon as the sole solid-phase species is 100 kmol and the listed species above in the gas phase

are all 1 kmol, respectively. Figure 5-2 depicts the equilibrium amount of each species as temperature increases. With the excess of carbon, the final gas products at equilibrium are CO(g), CO₂(g), and CF₄(g). With elevated voltages (or high current density), the probability for the generation of C₂F₆(g), CF₂(g) and CF(g) increases accordingly.

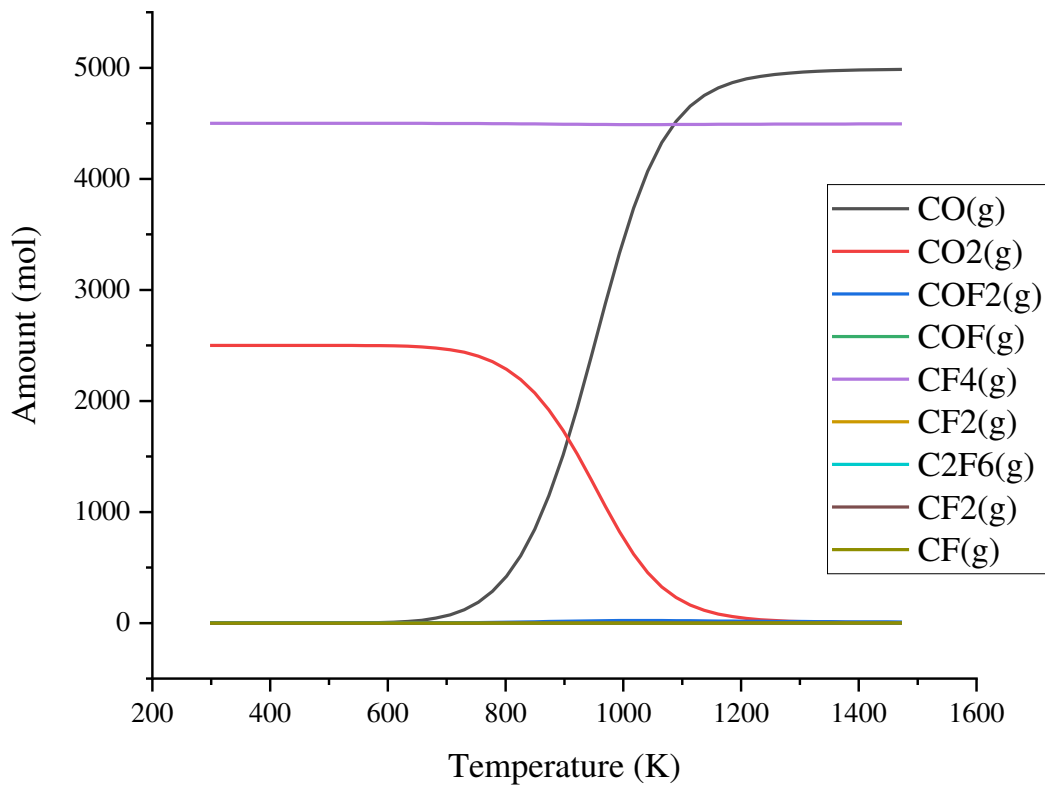


Figure 5-2 Gibbs free energy minimization by HSC Chemistry 8.0

The ratio of the CO(g) content to that of CO₂(g) is governed by the equilibrium of the Boudouard reaction ($CO_2(g) + C = 2CO(g)$). K is the equilibrium constant for the Boudouard

reaction, and Figure 5-3 illustrates the percentage of CO(g) content in the gas product, α , equals $\frac{\sqrt{K^2+4K}-K}{2}$ at equilibrium. At the practical operating temperature 1050 °C (1323 K), complete conversion of carbon dioxide into carbon monoxide is realized at equilibrium. Thus, α equals unity. Therefore, the decomposition of Nd₂O₃ at 1050 °C produces CO(g) as the primary reaction according to (5.1).

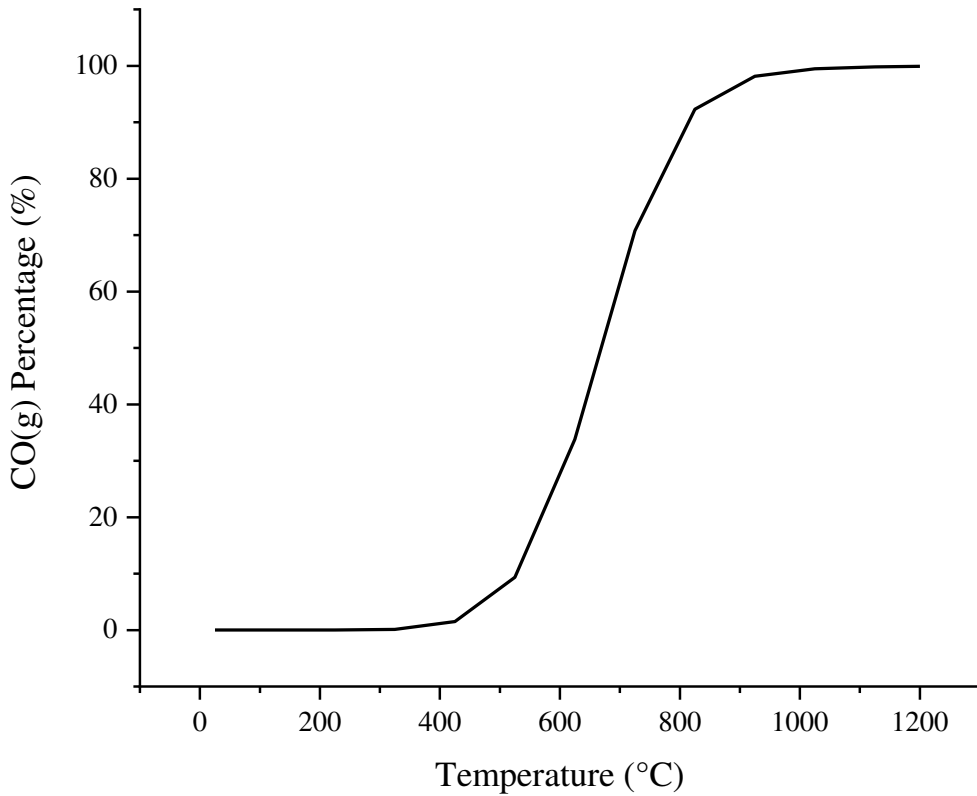


Figure 5-3 CO(g) percentage at equilibrium for the Boudouard Equation in the gas product

For Reaction (5.1), the decomposition voltage $\Delta V_{d,1}$ can be expressed as

$$\Delta V_{d,1} = \frac{1}{n_1 F} \left[\Delta G_1^o + \frac{1}{2} RT \ln \frac{\left(\frac{P_{CO}}{P^o} \right)^3}{a_{Nd_2O_3}} \right] \quad (5.14)$$

where n_1 is the moles of the transferred electrons to obtain one mole of neodymium according to (5.1), which equals 3; F is Faraday constant with value of 96485.33289 C mol⁻¹; ΔG_1^o is the standard Gibbs free energy for Reaction (5.1); R is the gas constant, which equals 8.3145 J mol⁻¹ K⁻¹; T is temperature in Kelvin (K); P_{CO} is the partial pressure of carbon monoxide; P^o is the total pressure of the atmosphere in the system, which here is regarded as 1 atm; and $a_{Nd_2O_3}$ is the activity of the dissolved neodymium oxide in the electrolyte. The activities of carbon and Nd are both considered unity.

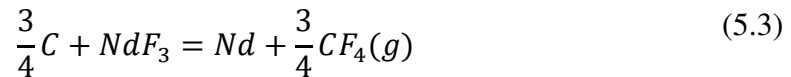
The standard decomposition voltage of the reaction $\Delta V_{d,1}^0$ is

$$\Delta V_{d,1}^0 = \frac{1}{n_1 F} \Delta G_1^o = -E_1^0 \quad (5.15)$$

Meanwhile, the equilibrium decomposition voltage of the reaction $\Delta V_{d,1}^{eq}$ is

$$\Delta V_{d,1}^{eq} = -E_1^0 - \frac{1}{2n_1 F} RT \ln a_{Nd_2O_3} \quad (5.16)$$

As for the decomposition of NdF₃ in the process, assuming the carbon is excessive, Reaction (5.3) takes place along with Reaction (5.1).



For Reaction (5.3), the decomposition voltage $\Delta V_{d,2}$ can be expressed as

$$\Delta V_{d,2} = \frac{1}{n_2 F} \left[\Delta G_2^0 + RT \ln \frac{\left(\frac{P_{CF_4}}{P^0}\right)^{\frac{3}{4}}}{a_{NdF_3}} \right] \quad (5.17)$$

where n_2 is the moles of the transferred electrons to obtain one mole of neodymium according to Reaction (5.3); ΔG_2^0 is the standard Gibbs free energy for Reaction (5.3); P_{CF_4} is the partial pressure of CF_4 ; a_{NdF_3} is the activity of neodymium fluoride in the melt. The activities of C and Nd are considered unity.

The standard decomposition voltage of the reaction $\Delta V_{d,2}^0$ is

$$\Delta V_{d,2}^0 = \frac{1}{n_2 F} \Delta G_2^0 = -E_2^0 \quad (5.18)$$

Again, the equilibrium decomposition voltage of the reaction $\Delta V_{d,2}^{eq}$ is

$$\Delta V_{d,2}^{eq} = -E_2^0 - \frac{1}{n_2 F} RT \ln a_{NdF_3} \quad (5.19)$$

To determine the order of the occurrence of the reactions mentioned above, the boundary condition for Reaction (5.3) to take over (5.1) is:

$$\Delta V_{d,2}^{eq} = \Delta V_{d,1}^{eq} \quad (5.20)$$

which gives

$$-E_2^0 - \frac{1}{n_2 F} RT \ln a_{NdF_3} + E_1^0 + \frac{1}{2n_1 F} RT \ln a_{Nd_2O_3} = 0 \quad (5.21)$$

Solving (5.21) gives

$$\ln \frac{a_{NdF_3}^2}{a_{Nd_2O_3}} = \frac{(E_1^0 - E_2^0) 2nF}{RT} \quad (5.22)$$

Substituting

$$E_1^0 = -1.211 V$$

and

$$E_2^0 = -2.769 V$$

for $T=1323.15 K$ ($1050\text{ }^\circ\text{C}$), we have

$$\ln \frac{a_{NdF_3}^2}{a_{Nd_2O_3}} = 81.990 \quad (5.23)$$

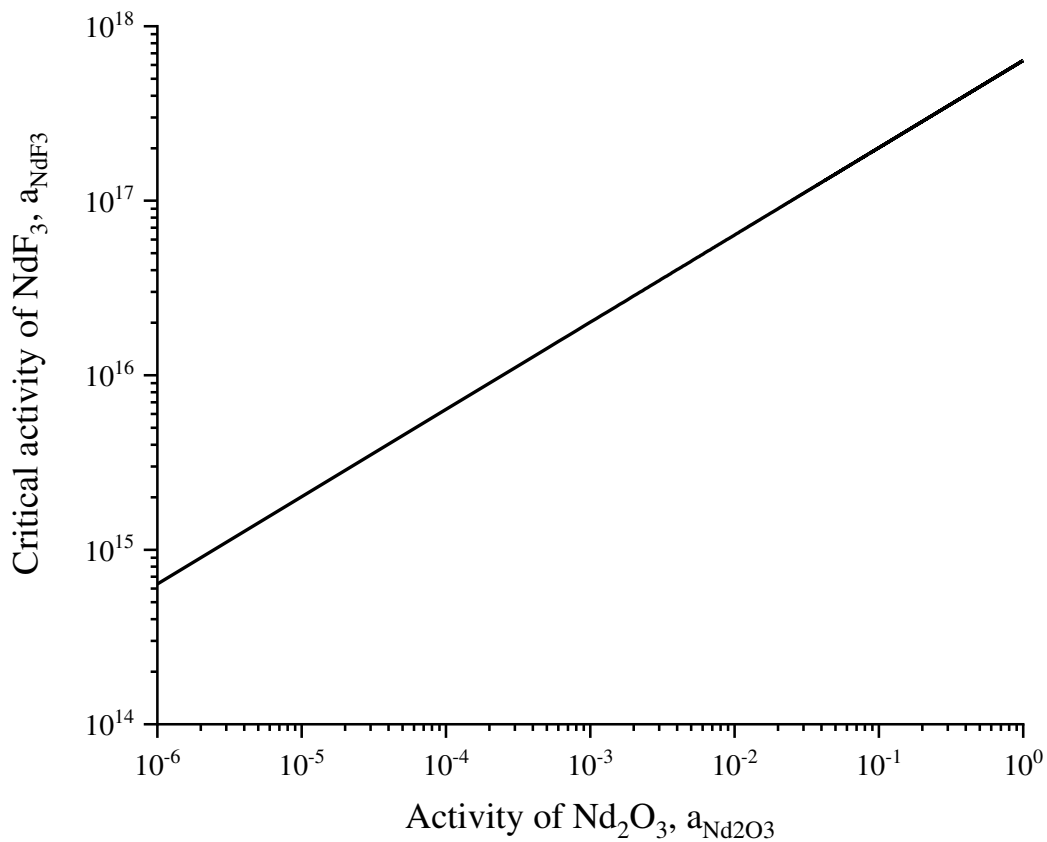


Figure 5-4 Thermodynamic calculation on the critical activity of NdF₃ for Reaction (5.3) to take over at different Nd₂O₃ activity level

Figure 5-4 presents the critical activity of NdF₃ for Reaction (5.3) to take over at various Nd₂O₃ level. This indicates it requires an extremely high level of activity for NdF₃ to dominate.

Therefore, the decomposition of Nd_2O_3 is thermodynamically favorable over that of NdF_3 with sufficient Nd_2O_3 activity.

As the current increases in the process, the involved reactions change at some certain points. At low current, neodymium oxide is the first thermodynamically available component in the system for decomposition. Only when current increases to a certain level (now defined as critical current, i_c) where the oxide is not sufficiently supplied at the electrodes, the decomposition of neodymium fluoride will co-occur. Because it needs significantly higher voltage to decompose lithium fluoride in the system, there is no need to discuss this case here.

When $i < i_c$, only Reaction (5.1) takes place in the electrolytic process, which is the desirable reaction for the electrolytic cell. The theoretical decomposition voltage for the electrolytic reaction ΔV_d can be, according to Nernst equation, expressed as:

$$\Delta V_d = \Delta V_{d,1} = \frac{1}{n_1 F} \left[\Delta G_1^o + \frac{1}{2} RT \ln \frac{\left(\frac{P_{\text{CO}}}{P^o}\right)^3}{a_{\text{Nd}_2\text{O}_3}} \right] = -E_1^o + \frac{1}{2n_1 F} RT \ln \frac{\left(\frac{P_{\text{CO}}}{P^o}\right)^3}{a_{\text{Nd}_2\text{O}_3}} \quad (5.24)$$

Accordingly, the standard decomposition voltage is

$$\Delta V_d^o = \frac{1}{n_1 F} \Delta G_1^o = -E_1^o \quad (5.25)$$

The equilibrium decomposition voltage is

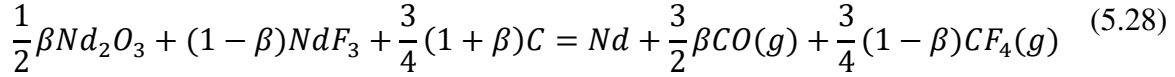
$$\Delta V_d^{eq} = \frac{1}{n_1 F} \left(\Delta G_1^o - \frac{1}{2} RT \ln a_{\text{Nd}_2\text{O}_3} \right) = -E_1^o - \frac{1}{n_1 F} RT \ln a_{\text{Nd}_2\text{O}_3} \quad (5.26)$$

When $i = i_c$, as discussed, the dissolution of Nd_2O_3 reaches its limit, and the decomposition of NdF_3 begins. As the current continues to increase, the overall reaction can be expressed as

$$\text{Reaction (5.27)} = \beta \text{ Reaction (5.1)} + (1-\beta) \text{ Reaction (5.5)} \quad (5.27)$$

where β is the mole fraction of element neodymium from the decomposition of Nd_2O_3 considering producing unit mole of neodymium overall.

Reaction (5.27) can be rewritten as



Thus

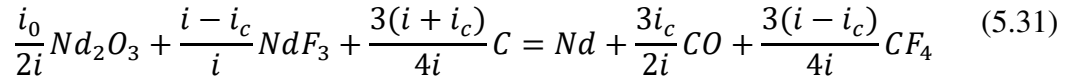
$$n_t = \beta n_1 + (1 - \beta)n_2 \quad (5.29)$$

where n_t is the mole amount of electron transfer per unit mole of neodymium product overall, which equals 3.

We can also obtain

$$\beta = \frac{i_c}{i} \quad (5.30)$$

Then Reaction (5.27) can be re-written as



Then we have

$$\Delta V_d = \Delta V_{d,t} = \beta\Delta V_{d,1} + (1 - \beta)\Delta V_{d,2} \quad (5.32)$$

Then it gives

$$\Delta V_d = \frac{i_c}{i}(E_2^0 - E_1^0) - E_2^0 + \frac{RT}{i} \left[\frac{i_c}{2n_1F} \ln \frac{\left(\frac{P_{\text{CO}}}{P^0}\right)^3}{a_{\text{Nd}_2\text{O}_3}} + \frac{i - i_c}{n_2F} \ln \frac{\left(\frac{P_{\text{CF}_4}}{P^0}\right)^{\frac{3}{4}}}{a_{\text{NdF}_3}} \right] \quad (5.33)$$

$$\Delta V_d^0 = \frac{i_c}{i}(E_2^0 - E_1^0) - E_2^0 \quad (5.34)$$

$$\Delta V_d^{eq} = \frac{i_c}{i}(E_2^0 - E_1^0) - E_2^0 + \frac{RT}{i} \left[\frac{i_c}{2n_1F} \ln \frac{\left(\frac{2i_c}{i + i_0}\right)^3}{a_{\text{Nd}_2\text{O}_3}} + \frac{i - i_c}{n_2F} \ln \frac{\left(\frac{i - i_c}{i + i_c}\right)^{\frac{3}{4}}}{a_{\text{NdF}_3}} \right] \quad (5.35)$$

When $i \gg i_c$, we obtain

$$\Delta V_d = \Delta V_{d,2} = \frac{1}{n_2 F} \left[\Delta G_2^o + RT \ln \frac{\left(\frac{P_{CF_4}}{P^o}\right)^{\frac{3}{4}}}{a_{NdF_3}} \right] = -E_2^o + \frac{1}{n_2 F} RT \ln \frac{\left(\frac{P_{CF_4}}{P^o}\right)^{\frac{3}{4}}}{a_{NdF_3}} \quad (5.36)$$

$$\Delta V_d^o = \Delta V_{d,2}^o = \frac{1}{n_2 F} \Delta G_2^o = -E_2^o \quad (5.37)$$

$$\Delta V_d^{eq} = \Delta V_{d,2}^{eq} = \frac{1}{n_2 F} (\Delta G_2^o - RT \ln a_{NdF_3}) = -E_2^o - \frac{1}{n_2 F} RT \ln a_{NdF_3} \quad (5.38)$$

5.4 Kinetics Considerations

Considering the NdF₃-LiF-Nd₂O₃ molten system, there are mainly five steps involved in the overall process:

- 1) Dissolution of neodymium oxide at the interface between the solid oxide and the bulk solution;
- 2) Dispersion of the dissolved oxide into the bulk solution, which maintains a saturated condition;
- 3) Diffusion and migration of neodymium-carrying ions and oxygen-carrying ions through the diffusional layer to the surface of the electrodes, respectively;
- 4) Neodymium oxide decomposition in the form of two half-cell reactions; and
- 5) The removal of the product metal and gases from the electrode surfaces into the metal collector at the bottom of the cell and the atmosphere at the top, respectively.

The current, which also represents the electrode reaction rate, is governed by the rates of the sequential steps. Upon the passage of faradaic current, the current remains the same. In a continuous electrolytic process, we assume the solution maintains the state of saturation with neodymium oxide and a fixed composition of fluorides.

Step 1: Dissolution of Nd₂O₃ into the bulk solution

At low current, the dissolution rate of the added oxide into the bulk solution, $\zeta_{d,m}$ (mole s^{-1}), is restrained due to the saturation state of oxide in molten salt solution. Then,

$$i = \zeta_{d,m} nF \quad (5.39)$$

where n represents moles of the transferred electrons per unit mole of the oxide, Nd_2O_3 , which is 6, and F is the Faraday constant, which is $96485.33289 \text{ C mol}^{-1}$.

It is assumed that the mass transfer in the bulk solution is sufficiently sustained to maintain the saturation state of the bulk solution. Only when the current gets as high as a certain point, i_c , the dissolution rate reaches its maximum, $\zeta_{d,m}^{max}$, which becomes independent of the solubility of the oxide in the solution, and instead determined by the variables such as temperature, the feeding method and particle size of the added oxide. Then, the critical current

$$i_c = \zeta_{d,m}^{max} nF \quad (5.40)$$

The electrolytic cell is operated at a fixed temperature above the melting point of neodymium. By reducing the particle size of the added oxide or placing more feeding points, the maximum dissolution rate can increase due to the increase of the contact surface area of the feed particles.

At higher current ($i > i_c$), the electrolytic cell will commence to decompose the second thermodynamically available component, NdF_3 . The neodymium product is the result of the decomposition of two components: Nd_2O_3 and NdF_3 . Therefore, the current, i , can be considered as the sum of two components:

$$i = i_c + i_{NdF_3} \quad (5.41)$$

where i_{NdF_3} is the current component contributing to the decomposition of NdF_3 .

Step 2: Mass Transfer of Dissolved Oxide into Bulk Solution

With the oxide dissolved through the interface between the added solid neodymium oxide and the bulk solution into the bulk solution, the dissolved oxide is transferred in the form of oxygen-carrying ions and neodymium ions, respectively, to the interface between the boundary layer of each electrode and the bulk solution. Assuming the mass transfer rate for the neodymium oxide is χ_{bulk} (mole s^{-1}), then we have

$$i = \chi_{bulk} nF \quad (5.42)$$

At low current, the mass transfer rate is determined by the demand for the oxide at the electrodes. With the mass transfer of the dissolved oxide, the bulk solution maintains saturated with the oxide. However, when the current reaches a high level where ζ_{bulk} increases to its maximum rate, ζ_{bulk}^{max} , the mass transfer of the dissolved oxide to the boundary layer is limited and the decomposition of the neodymium fluoride occurs along with that of the neodymium oxide. We obtain

$$i_c = \chi_{bulk}^{max} nF \quad (5.43)$$

At higher current, it gives

$$i = i_c + i_{NdF_3} \quad (5.44)$$

Step 3: Diffusion and migration of neodymium ions and oxygen-carrying ions through the diffusional layer to the surface of the electrodes, respectively

Adjacent to the electrodes, a thin diffusional layer (also called boundary layer) is formed due to the consumption of the oxide at the electrodes. We first consider the cathode; the situation for the anode will be similar.

In the cathodic diffusional layer, the current is attributed to three factors: the convection of the ions, the diffusional force due to the concentration gradient, and the ion migration because of the electric field throughout the layer. Consider an infinitesimal element of solution in the

diffusional layer at r . The cathode surface is negatively charged and available to provide electrons to reduce the positively charged neodymium ions.

For linear mass transfer, the current density J can be expressed as the sum of the three terms respectively relating to each component:

$$J = \sum_{i=1}^3 J_i \quad (5.45)$$

(1) Term J_1 relating to the convection

Due to convection in the solution, the charged species j obtains an initial momentum.

Term J_1 can be expressed as

$$J_1 = \sum_j v_j n_j q \quad (5.46)$$

where v_j is the initial velocity of the charged species j ; n_j is the charge density of j ; and q is the elementary charge, which equals $1.602\ 176\ 62 \times 10^{-19}$ C.

In this case, we are concerned with systems in which convection is absent, thus

$$J_1 = 0 \quad (5.47)$$

(2) Term J_2 relating to diffusion

At the surface of the electrode, the oxide is consumed, and a concentration gradient is formed from the bulk solution to the electrode surface through the diffusional layer. At the cathode, Term J_2 can be written as

$$J_2 = \sum_j D_j \frac{C_{j,r+\Delta r} - C_{j,r}}{\Delta r} z_j F \quad (5.48)$$

where D_j is the mass transfer diffusivity of charged species j in the molten salts; C_j is the concentration of species j in the solution; F is the Faraday constant, which is 96485.33289 C mol⁻¹.

J_2 can be rewritten in its differential form as

$$J_2 = \sum_j D_j \frac{\partial C_j}{\partial r} z_j F \quad (5.49)$$

Term J_2 is attributed to the concentration gradient from all species. In the process of the decomposition of Nd_2O_3 , the concentrations of the species except for Nd^{3+} can be considered constant throughout the diffusional layer.

(3) Term J_3 relating to migration

According to Ohm's law $R = E/I$, we have

$$\frac{1}{\kappa} \frac{\Delta r}{2\pi r h} = \frac{\Phi_{r+\Delta r} - \Phi_r}{2\pi r h J_3} \quad (5.50)$$

This can be expressed as

$$J_3 = \kappa \frac{\partial \Phi}{\partial r} \quad (5.51)$$

where κ is the electrical conductivity of the molten salts at the infinitesimal element; $\Phi_{r+\Delta r}$ and Φ_r represent the electrical potential at $r + \Delta r$ and r , respectively.

Now the current density J can be expressed as

$$J = \sum_j D_j \frac{\partial C_j}{\partial r} z_j F + \kappa \frac{\partial \Phi}{\partial r} \quad (5.52)$$

Because

$$J = \frac{i}{2\pi r h} \quad (5.53)$$

where h is the depth of the electrode submerged into the electrolyte, then it gives

$$i = 2\pi r h \left(\sum_j D_j \frac{\partial C_j}{\partial r} z_j F + \kappa \frac{\partial \Phi}{\partial r} \right) \quad (5.54)$$

Similarly, one can conclude that at the boundary layer nearby the anode, we obtain

$$i = 2\pi r h \left(\sum_m D_m \frac{\partial C_m}{\partial r} z_m F - \kappa \frac{\partial \Phi}{\partial r} \right) \quad (5.55)$$

where m represents the species in the anodic diffusional layer.

Step 4: Chemical reactions at the electrodes

The half-cell chemical reactions occur at the electrode surfaces once the oxygen-carrying ions arrives at the anode and the neodymium ion reaches the cathode. The primary reactions are expressed as (5.1) and (5.2). At high current, the secondary reaction for the decomposition of neodymium fluoride takes place as (5.3).

Step 5: Removal of products

While the metallic neodymium product leaves the cathode surface due to the gravitational force and accumulates at the bottom of the cell, the gas products (CO, CO₂, CF₄, etc.) are released from the anode surface due to the buoyant force exerted by the electrolyte and emits from the top surface of the melt.

The gas generated at the anode evolves at the surface of the electrode in the form of bubbles. When the bubble grows to the extent to which the contact angle for the gas bubble against the anode surface becomes 90°, the bubble is released from the surface of the anode. Then the bubble is subjected to the acceleration due to the buoyant force exerted by the melt and obtains a velocity to travel towards the upper end of the melt. When it reaches equilibrium (assuming the travel distance is sufficiently long for the bubble to be balanced with forces), the velocity of the bubble, v_t , reaches maximum and then keeps moving upward until hitting the surface of the melt and emitting into the atmosphere.

Research (Cassayre, Utigard et al. 2002) conducted to visualize gas evolution on the anode in molten salt electrolysis process shows that with the increase of the current the size of

the bubbles before release decreases in the electrolysis process and the release of the bubble from the anode becomes more efficient. The convection of the electrolyte near the anode may result in the collision of the gas bubbles through the removal path and the effect causes the combination of bubbles.

5.5 Electrolysis Model Establishment

5.5.1 Voltage drop between the anode and the cathode

Electrolysis model is establishment based on the voltage drop along the passage of faradaic current. The total cell voltage can be regarded as the sum of a series of voltage drops through the current path in the cell, and expressed as below:

$$\Delta V_{ac} = \Delta V_d + \eta + \Delta V_{bulk} + \Delta V_{ad} + \Delta V_{cd} + (R_s + R_{bubble})i \quad (5.56)$$

where ΔV_{ac} is the total cell voltage, ΔV_d is the theoretical decomposition voltage, η is the activation overpotential at the electrodes, ΔV_{bulk} is the voltage drop through the bulk solution, ΔV_{ad} is the voltage drop through the diffusion layer adjacent the anode, ΔV_{cd} is the voltage drop through the diffusional layer adjacent the cathode, R_s is the system resistance of the cell and R_{bubble} is the resistance due to the presence of the gas bubbles in the electrolysis process.

ΔV_d is determined by the thermodynamics study above. The activation overpotential η is assumed to be constant within a certain range in the current discussion according to the Butler-Volmer equation under the assumption that surface concentrations do not differ appreciably from the bulk values. The system resistance R_s can also be treated as constant.

As for the resistance associated with the presence of the gas bubbles R_{bubble} , a discussion is needed according to the current in the process. When the current is significantly low, R_{bubble} is minimal. As current increases, the reaction reaches equilibrium and the resistance can be considered as constant. At elevated current when the removal of the gas products becomes less

efficient, the gas bubbles accumulate at the surface of the anode and form an unwetting gas film which insulates the melt from the anode, causing a significant high resistance which results in an open circuit for the process. This phenomenon is known as anode effect.

The following paragraphs discuss the rest of the terms for the equation.

The Voltage Drop through the Diffusional Layers (ΔV_{ad} and ΔV_{cd})

In the diffusional layer for the cathode, we obtain according to (5.54)

$$\frac{i}{2\pi h} \frac{1}{r} dr = \sum_j D_j z_j F dC_j + \kappa d\Phi \quad (5.57)$$

Dividing each term by κ , the equation above can be rewritten as

$$\frac{i}{2\pi h} \frac{1}{\kappa} \frac{1}{r} dr = \frac{1}{\kappa} \sum_j D_j z_j F dC_j + d\Phi \quad (5.58)$$

Because the solubility of the neodymium oxide in the electrolyte is relatively low and the change on the electrical conductivity for the electrolyte saturated with the oxide is minimal, at the infinitesimal plane, $d\kappa$ is approximately zero and thus $d\frac{1}{\kappa} = 0$, we have

$$\frac{1}{\kappa} \frac{1}{r} dr = d\left(\frac{1}{\kappa} \ln r\right) - \ln r d\frac{1}{\kappa} = d\left(\frac{1}{\kappa} \ln r\right) \quad (5.59)$$

and

$$\frac{1}{\kappa} dC_j = d\left(\frac{1}{\kappa} C_j\right) - C_j d\frac{1}{\kappa} = d\left(\frac{1}{\kappa} C_j\right) \quad (5.60)$$

Hence, Equation (5.59) can also be rewritten as

$$\frac{i}{2\pi h} \frac{1}{\kappa} d\left(\frac{1}{\kappa} \ln r\right) = \sum_j D_j z_j F d\left(\frac{1}{\kappa} C_j\right) + d\Phi \quad (5.61)$$

r_{ab} is the radius of the interface between the boundary layer at the anode and the bulk solution and r_{cb} is for that of the cathode. Take integral of Equation (5.61) from $r = r_c$ to $r = r_{cb}$, and then we have

$$\int_{\frac{1}{\kappa_c} \ln r_c}^{\frac{1}{\kappa_{cb}} \ln r_{cb}} \frac{i}{2\pi h} d\left(\frac{1}{\kappa} \ln r\right) = \int_{\frac{1}{\kappa_c} C_{j,c}}^{\frac{1}{\kappa_{cb}} C_{j,cb}} \sum_j D_j z_j F d\left(\frac{1}{\kappa} C_j\right) + \int_{\Phi_c}^{\Phi_{cb}} d\Phi \quad (5.62)$$

Thus,

$$\frac{i}{2\pi h} \left(\frac{1}{\kappa_{cb}} \ln r_{cb} - \frac{1}{\kappa_c} \ln r_c \right) = \sum_j D_j z_j F \left(\frac{1}{\kappa_{cb}} C_{j,cb} - \frac{1}{\kappa_c} C_{j,c} \right) + (\Phi_{cb} - \Phi_c) \quad (5.63)$$

Meanwhile,

$$\kappa_{cb} = \kappa_{bulk} \quad (5.64)$$

$$C_{j,cb} = C_{j,bulk} \quad (5.65)$$

$$\Phi_{cb} - \Phi_c = \Delta V_{cd} \quad (5.66)$$

Thus,

$$\Delta V_{cd} = \frac{i}{2\pi h} \left(\frac{1}{\kappa_{bulk}} \ln r_{cb} - \frac{1}{\kappa_c} \ln r_c \right) - \sum_j D_j z_j F \left(\frac{1}{\kappa_{bulk}} C_{j,bulk} - \frac{1}{\kappa_c} C_{j,c} \right) \quad (5.67)$$

For the anode, similarly, we have

$$\Delta V_{ad} = -\frac{i}{2\pi h} \left(\frac{1}{\kappa_{bulk}} \ln r_{ab} - \frac{1}{\kappa_a} \ln r_a \right) + \sum_m D_m z_m F \left(\frac{1}{\kappa_{bulk}} C_{j,bulk} - \frac{1}{\kappa_a} C_{m,a} \right) \quad (5.68)$$

The Voltage Drop through the Bulk Solution (ΔV_{bulk})

According to the Ohm's Law, it gives in the bulk solution

$$i = 2\pi r h \kappa_{bulk} \frac{\partial \Phi}{\partial r} \quad (5.69)$$

It can be rewritten as

$$d\Phi = \frac{i}{2\pi h \kappa_{bulk}} \frac{1}{r} dr \quad (5.70)$$

Take integral from $r = r_{cb}$ to $r = r_{ab}$, and we have

$$\Delta V_{bulk} = \frac{i}{2\pi h \kappa_{bulk}} \ln \frac{r_{ab}}{r_{cb}} \quad (5.71)$$

Hence

$$\begin{aligned} \Delta V_c + \Delta V_a + \Delta V_{bulk} & \quad (5.72) \\ &= \frac{i}{2\pi h} \left(\frac{1}{\kappa_a} \ln r_a - \frac{1}{\kappa_c} \ln r_c \right) \\ &+ \sum_m D_m z_m F \left(\frac{1}{\kappa_{bulk}} C_{j,bulk} - \frac{1}{\kappa_a} C_{m,a} \right) \\ &- \sum_j D_j z_j F \left(\frac{1}{\kappa_{bulk}} C_{j,bulk} - \frac{1}{\kappa_c} C_{j,c} \right) \end{aligned}$$

Therefore, the inter-electrode voltage drop ΔV_{ac} can be expressed as

$$\Delta V_{ac} = \Delta V_d + \eta + \Sigma_m + \Sigma_j + [R_s + R_{bubble} + \frac{1}{2\pi h} \left(\frac{1}{\kappa_a} \ln r_a - \frac{1}{\kappa_c} \ln r_c \right)] i \quad (5.73)$$

where Σ_m represents the concentration term $\sum_m D_m z_m F \left(\frac{1}{\kappa_{bulk}} C_{j,bulk} - \frac{1}{\kappa_a} C_{m,a} \right)$ from the anode diffusional layer and Σ_j represents the concentration term $\sum_j [-D_j z_j F \left(\frac{1}{\kappa_{bulk}} C_{j,bulk} - \frac{1}{\kappa_c} C_{j,c} \right)]$ from the cathode diffusional layer.

Throughout the electrolytic process, only the negatively charged ion species are subjected to the concentration change in the anode diffusional layer while only the positively charged ion species are considered in terms of concentration changes in the cathode diffusional layer.

5.5.2 Discussion on ΔV_{ac}

When the current through the passage between the electrodes is small, starting from zero, the decomposition of the neodymium oxide occurs, and the controlling step is the chemical

reaction at the electrode surfaces. Other steps involved in the process can be considered very fast, which means the solution including the bulk part and the part in the diffusional layer is homogeneous. Both Term Σ_m and Term Σ_j equal to zero. Furthermore, $\kappa_a = \kappa_c = \kappa_{bulk}$.

Because the rate of the reaction is slow and the decomposition voltage ΔV_d is $-E_1^0 + \frac{1}{2n_1F} RT \ln \frac{(\frac{P_{CO}}{P^0})^3}{a_{Nd_2O_3}}$, the removal of the gas product is fast and P_{CO} closes to zero. Thus, ΔV_d has a value smaller than the equilibrium decomposition voltage.

The voltage drop ΔV_{ac} can be written as

$$\Delta V_{ac} = E_1^0 + \frac{1}{2n_1F} RT \ln \frac{(\frac{P_{CO}}{P^0})^3}{a_{Nd_2O_3}} + \eta + [R_s + R_{bubble} + \frac{1}{2\pi h} \frac{1}{\kappa_{bulk}} \ln \frac{r_a}{r_c}] i \quad (5.74)$$

With the increase of the current, the rate of the half reactions at the respective electrodes increases and the control step of the kinetics transitions to the diffusional step control. In the anode diffusional layer, only oxygen-carrying ions are expected to respond to the reaction and the concentration of the ion decreases from the bulk solution level, $C_{[O^{2-}],bulk}$, to zero. On the other hand, in the cathode diffusional layer, the concentration of Nd^{3+} at the anode surface decreases from the level saturated with oxide, $C_{Nd^{3+},bulk}$, to that of the plain fluoride salts, $C_{Nd^{3+}(salt)}$, while that at the bulk solution end remains the saturation level. Other cations remain a constant level. Thus, when the controlling step of the diffusional layers takes place, it gives

$$\Sigma_m = D_{[O^{2-}]} z_{[O^{2-}]} F \frac{1}{\kappa_{bulk}} C_{[O^{2-}],bulk} \quad (5.75)$$

where $D_{[O^{2-}]}$ is the diffusivity of the oxygen-carrying ions and $z_{[O^{2-}]}$ is the moles of charges in unit mole of oxygen-carrying ion with a negative value;

and

$$\Sigma_j = -D_{Nd^{3+}} z_{Nd^{3+}} F \left(\frac{1}{\kappa_{bulk}} C_{Nd^{3+},bulk} - \frac{1}{\kappa_{salt}} C_{Nd^{3+},salt} \right) \quad (5.76)$$

where $D_{Nd^{3+}}$ is the diffusivity of the neodymium ions and $z_{Nd^{3+}}$ is the moles of charges in unit mole of neodymium ion, which has a value of 3.

Both terms can be determined by the solubility of the neodymium oxide in the system.

The concentration factor terms decrease from the level of zero to a constant negative level under the diffusional control.

Meanwhile, because of the fast reaction effect, the decomposition voltage ΔV_d increases to the level of the equilibrium value. P_{CO} grows from around zero to unity, which causes the significant increase for the decomposition voltage. When P_{CO} becomes unity, the required decomposition voltage reaches its equilibrium level. That is, ΔV_d equals $-E_1^0 - \frac{1}{2n_1 F} RT \ln a_{Nd_2O_3}$.

When the current level reaches a point where the controlling step occurs in the diffusional layers, the voltage drop between the two electrodes can be expressed as

$$\begin{aligned} \Delta V_{ac} = & -E_1^0 - \frac{1}{2n_1 F} RT \ln a_{Nd_2O_3} + \eta + D_{[O^{2-}]} z_{[O^{2-}]} F \frac{1}{\kappa_{bulk}} C_{[O^{2-}],bulk} \\ & - D_{Nd^{3+}} z_{Nd^{3+}} F \left(\frac{1}{\kappa_{bulk}} C_{Nd^{3+},bulk} - \frac{1}{\kappa_{salt}} C_{Nd^{3+},salt} \right) + [R_s \\ & + R_{bubble} + \frac{1}{2\pi h} \frac{1}{\kappa_{salt}} \ln \frac{r_a}{r_c}] i \end{aligned} \quad (5.77)$$

In Equation (5.77), we define

$$\begin{aligned} \Sigma_1 = -E_1^0 - \frac{1}{2n_1F} RT \ln a_{Nd_2O_3} + \eta + D_{[O^{2-}]} Z_{[O^{2-}]} F \frac{1}{\kappa_{bulk}} C_{[O^{2-}],bulk} \\ - D_{Nd^{3+}} Z_{Nd^{3+}} F \left(\frac{1}{\kappa_{bulk}} C_{Nd^{3+},bulk} - \frac{1}{\kappa_{salt}} C_{Nd^{3+},salt} \right) \end{aligned} \quad (5.78)$$

and

$$S = R_s + R_{bubble} + \frac{1}{2\pi h} \frac{1}{\kappa_{salt}} \ln \frac{r_a}{r_c} \quad (5.79)$$

Then, Equation (5.77) can be rewritten as

$$\Delta V_{ac} = \Sigma_1 + Si \quad (5.80)$$

We notice that the terms in Σ_1 and S can be determined as constants. Therefore, ΔV_{ac} against i is a straight line with Σ_1 as the intercept and S as the slope. Define the geometry term G as the following equation for this model.

$$G = \frac{1}{2\pi h} \ln \frac{r_a}{r_c} \quad (5.81)$$

As the increase of the current continues, the equation above continues to work for the system until the point where a) the dissolution of the oxide or b) the transport of the dissolved oxide to the boundary layer reaches its maximum rate.

In the former case, considering the transport of the dissolved oxide is sufficiently fast, due to the dissolution rate limitation at the high current level, the oxide is not supplied sufficiently at the electrodes for the decomposition reaction and the redundant current triggers the decomposition of the next thermodynamically available component in the system, that is, neodymium fluoride. The occurrence of the neodymium fluoride decomposition can be delayed in the progress of increasing current by extending the limit for the oxide dissolution rate, which can be realized through preheating the oxide, changing the feeding method, adding feeding points, and reducing the particle size of the oxide feed, etc.

In the latter case, considering the dissolution rate of the oxide has not reaches its limit, the dissolved oxide is not able to transfer sufficiently fast to the diffusional layer and thus the oxide is not supplied sufficiently at the electrodes for the decomposition reaction at the elevated current level. The redundant current triggers the decomposition of neodymium fluoride. In this case, one can tune the electrolytic cell geometry to facilitate the mass transfer of the dissolve oxide. For example, reducing the electrode gap can shorten the travel distance for the ions to the electrode surfaces.

We define the current level where the decomposition of neodymium fluoride starts to occur as critical current (i_c). The ratio of the neodymium product resulting from the decomposition of neodymium oxide to that from neodymium fluoride can be expressed as

$$Ratio \frac{Nd(oxide)}{Nd(fluoride)} = \frac{i_c}{i - i_c} \quad (5.82)$$

where $Nd(oxide)$ is the moles of neodymium product resulting from the decomposition of the neodymium oxide and $Nd(fluoride)$ is that from the decomposition of the neodymium fluoride.

When the decomposition of neodymium fluoride occurs, two processes of reactions are of interest. The reaction involved is shown as Equation (5.31). The process leading to the decomposition of neodymium oxide is still considered diffusion-controlled while the other process leading to the decomposition of neodymium fluoride is controlled by the rate of the relevant chemical reaction. When $i - i_c$ is small and grows from zero, the removal of the gas product component (CF_4) at the anode is considered fast and P_{CF_4} is closed to zero. The decomposition voltage drop attributed to the decomposition of neodymium fluoride is at a level smaller than the equilibrium value. Thus,

$$\Delta V_d = \frac{i_0}{i} (E_2^0 - E_1^0) - E_2^0 + \frac{RT}{i} \left[\frac{i_0}{2n_1 F} \ln \frac{1}{a_{Nd_2O_3}} + \frac{i - i_0}{n_2 F} \ln \frac{\left(\frac{P_{CF_4}}{P^0}\right)^{\frac{3}{4}}}{a_{NdF_3}} \right] \quad (5.83)$$

At the same time, the concentration terms regarding to the NdF_3 decomposition remain zero. The voltage drop between the two electrodes can be expressed as

$$\begin{aligned} \Delta V_{ac} = & \frac{i_0}{i} (E_2^0 - E_1^0) - E_2^0 + \frac{RT}{i} \left[\frac{i_0}{2n_1 F} \ln \frac{1}{a_{Nd_2O_3}} + \frac{i - i_0}{n_2 F} \ln \frac{\left(\frac{P_{CF_4}}{P^0}\right)^{\frac{3}{4}}}{a_{NdF_3}} \right] + \eta \quad (5.84) \\ & + D_{[O^{2-}]} Z_{[O^{2-}]} F \frac{1}{\kappa_{bulk}} C_{[O^{2-}],bulk} \\ & - D_{Nd^{3+}} Z_{Nd^{3+}} F \left(\frac{1}{\kappa_{bulk}} C_{Nd^{3+},bulk} - \frac{1}{\kappa_{salt}} C_{Nd^{3+},salt} \right) + Si \end{aligned}$$

where P_{CF_4} is close to zero, which results in a decrease of the decomposition voltage term.

One expects a significant plunge at the critical current i_c . The plunge is slightly smoothed due to the small fraction of the fluoride decomposition at the beginning of the secondary reaction.

As $i - i_c$ continues to increase, the path for the decomposition of neodymium fluoride transitions to be diffusion control. During this stage, the decomposition voltage drop ΔV_d increases to its equilibrium level. Meanwhile, term $-D_{Nd^{3+}} Z_{Nd^{3+}} F \left(\frac{1}{\kappa_{bulk}} C_{Nd^{3+},bulk} - \frac{1}{\kappa_{salt}} C_{Nd^{3+},salt} \right)$ decreases to a more negative level as $-D_{Nd^{3+}} Z_{Nd^{3+}} F \frac{1}{\kappa_{bulk}} C_{Nd^{3+},bulk}$ while a new term as $D_{F^-} Z_{F^-} F \left(\frac{1}{\kappa_{bulk}} C_{F^-,bulk} - \frac{1}{\kappa_c} C_{F^-,c} \right)$ comes into being and decrease from 0 to $D_{F^-} Z_{F^-} F \left(\frac{1}{\kappa_{bulk}} C_{F^-,bulk} - \frac{1}{\kappa_{LiF}} C_{F^-(LiF)} \right)$. When the secondary process reaches to the diffusional control, the voltage drop between the two electrodes can be expressed as

$$\begin{aligned}
\Delta V_{ac} = & \frac{i_0}{i} (E_2^0 - E_1^0) - E_2^0 + \frac{RT}{i} \left[\frac{i_0}{2n_1F} \ln \frac{\left(\frac{2i_0}{i+i_0}\right)^3}{a_{Nd_2O_3}} + \frac{i-i_0}{n_2F} \ln \frac{\left(\frac{i-i_0}{i+i_0}\right)^{\frac{3}{4}}}{a_{NdF_3}} \right] + \eta \\
& + D_{[O^{2-}]Z_{[O^{2-}]}} F \frac{1}{\kappa_{bulk}} C_{[O^{2-}],bulk} + D_{F^-Z_{F^-}} F \left(\frac{1}{\kappa_{bulk}} C_{F^-,bulk} \right. \\
& \left. - \frac{1}{\kappa_{LiF}} C_{F^-(LiF)} \right) - D_{Nd^{3+}Z_{Nd^{3+}}} F \frac{1}{\kappa_{bulk}} C_{Nd^{3+},bulk} + Si
\end{aligned} \tag{5.85}$$

One should note that we assume the molten salt remains the constant composition in the bulk solution even if the decomposition of neodymium fluoride occurs.

When $i \gg i_c$, the decomposition voltage drop for the reaction involved in the process

ΔV_d equals $-E_2^0 - \frac{1}{n_2F} RT \ln a_{NdF_3}$. Thus, we obtain

$$\begin{aligned}
\Delta V_{ac} = & -E_2^0 - \frac{1}{n_2F} RT \ln a_{NdF_3} + \eta + D_{[O^{2-}]Z_{[O^{2-}]}} F \frac{1}{\kappa_{bulk}} C_{[O^{2-}],bulk} \\
& + D_{F^-Z_{F^-}} F \left(\frac{1}{\kappa_{bulk}} C_{F^-,bulk} - \frac{1}{\kappa_{LiF}} C_{F^-(LiF)} \right) \\
& - D_{Nd^{3+}Z_{Nd^{3+}}} F \frac{1}{\kappa_{bulk}} C_{Nd^{3+},bulk} + Si
\end{aligned} \tag{5.86}$$

We define

$$\begin{aligned}
\Sigma_2 = & -E_2^0 - \frac{1}{n_2F} RT \ln a_{NdF_3} + \eta + D_{[O^{2-}]Z_{[O^{2-}]}} F \frac{1}{\kappa_{bulk}} C_{[O^{2-}],bulk} \\
& + D_{F^-Z_{F^-}} F \left(\frac{1}{\kappa_{bulk}} C_{F^-,bulk} - \frac{1}{\kappa_{LiF}} C_{F^-(LiF)} \right) \\
& - D_{Nd^{3+}Z_{Nd^{3+}}} F \frac{1}{\kappa_{bulk}} C_{Nd^{3+},bulk}
\end{aligned} \tag{5.87}$$

We notice that terms in Σ_2 are found constant, and Equation (5.86) can be rewritten as

$$\Delta V_{ac} = \Sigma_2 + Si \tag{5.88}$$

Equation (5.88) indicates that when $i \gg i_c$, the function of ΔV_{ac} against i is a straight line with Σ_2 as the intercept and S as the slope.

5.5.3 Anode effect

In the progress of increasing current, the current density at the anode increases, which means the generation of the gas product occurs more rapidly. When the chemical reactions reach their equilibria, the rate of gas products leaving the molten salts equals the generation rate at the anode. When the current increases to a certain amount, due to the surface condition of anode, the bubble size reaches its minimum limitation, and the rate of gas products leaving the salts becomes smaller than that of them generating at the anode, which results in the accumulation of the gas(es) at the electrode. The accrued gas forms an unwetting film against the surface of the anode and then insulates electrolyte from the anode. This phenomenon is known as anode effect. The anode effect can occur at any stage discussed above as soon as the inefficient gas removal at the anode occurs.

5.5.4 $\Delta V_{ac} - i$ Diagram Development

According to the discussion above, we obtain a diagram as Figure 5-5 to illustrate the relationship between the inter-electrode voltage drop ΔV_{ac} and the current, i . In this diagram, ΔV_{ac} is a function of i . The diagram depicts the interelectrode voltage drop between the anode and the cathode against the current in the molten fluoride electrolysis system.

At Point a, the electrolysis circuit is closed and the electrolytic reaction is triggered with a small current. The required ΔV_{ac} is relatively lower than that intercept value obtained by extrapolating Line cb due to that fact the reaction at this point does not achieve equilibrium and the partial pressure of generated carbon monoxide is close to zero. The rate of corresponding chemical reaction at low current level is relatively lower than that of the rest kinetic steps, and

thus along Line ab the controlling step of the process is the chemical reaction, which transitions to the diffusional control at Point b.

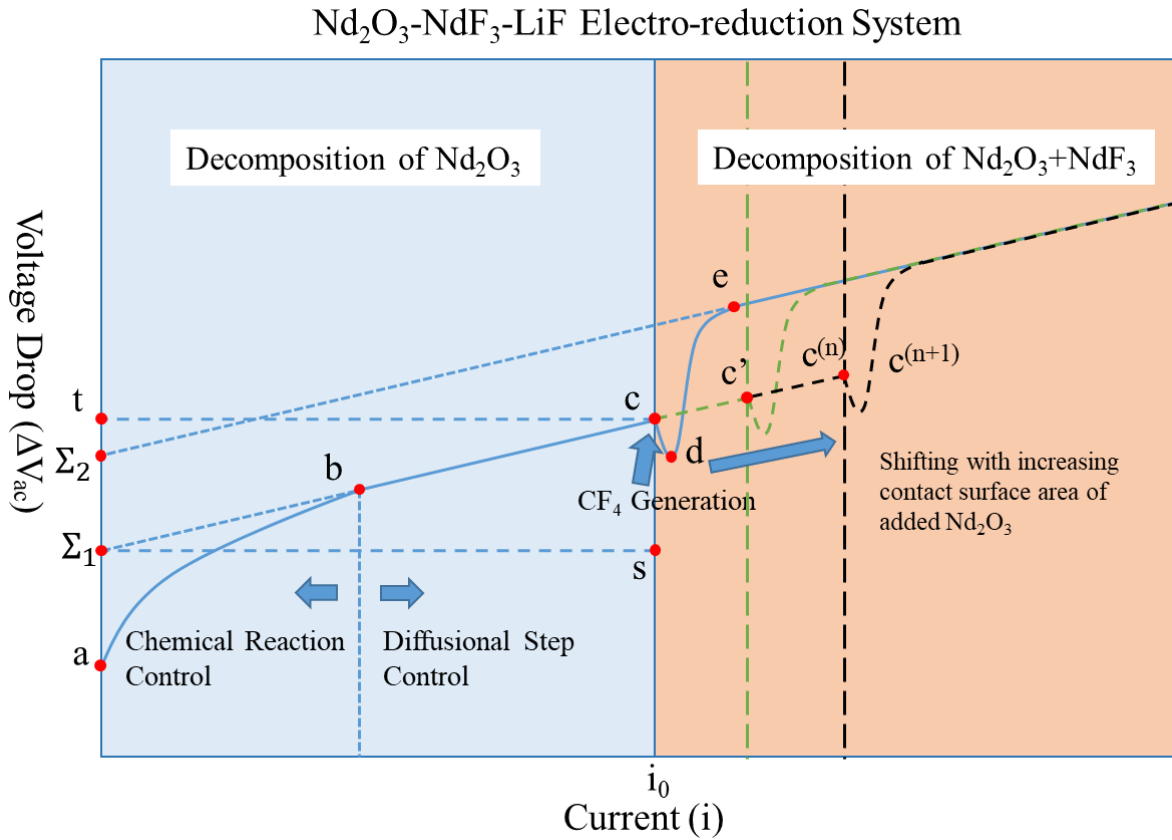


Figure 5-5 Schematic of inter-electrode voltage drop (ΔV_{ac}) against current (i) in the Nd₂O₃-NdF₃-LiF electro-reduction system

The rate of the chemical reaction involved increases with the current. When it reaches Point b, the diffusional layers at the anode and the cathode become stable. This means both the half reactions at the surfaces of the electrodes consume the corresponding ions so efficiently that the concentration of the overall neodymium oxide at the electrode surfaces equals zero and the other side of the diffusional layers which are near the bulk solution remains at the saturation

state of the oxide. The mass transfer throughout the diffusional layer limits the process and this state maintains from Point b to Point c. From Point b to Point c, the voltage drop can be expressed as Equation (5.80). In this equation, one can see that intercept term, Σ_1 , can be determined as a constant, and so does the slope term, S. Therefore, the curve is expected to be a straight line from Point b to Point c.

The dissolution rate of the neodymium oxide reaches the maximum value at Point c. Due to the lack of sufficient supply of the oxide to the boundary layers as the current continues to increase, the decomposition of neodymium fluoride starts and the reaction results in the generation of CF_4 . Point c corresponds to the critical current, i_c . From Point c to Point d, the voltage drop is determined by Equation (5.84). At Point d, the secondary reaction of the NdF_3 decomposition reaches equilibrium state. From Point d to Point e, the voltage drop can be determined by Equation (5.85). At Point e where it represents $i \gg i_c$, the voltage drop can be expressed as Equation (5.88).

When increasing the contact of the surface area of the added neodymium oxide with bulk solution by decreasing the particles size of the oxide, we obtain an increased maximum dissolution rate for the oxide. Point c is expected to shift along the extrapolative line of Line bc to Point c' and furthermore to Point $c^{(n)}$. At Point $c^{(n)}$, the particle size of the added oxide is decreased to the extent where the maximum dissolution rate of the oxide is realized at the same time that it reaches the maximum mass transfer rate for the dissolved oxide to be dispersed into the bulk solution and reach to the boundary layer to supply for the reaction. With further decrease on the particle size of the neodymium oxide, Point $c^{(n+1)}$ overlaps with Point $c^{(n)}$ instead of shifting further.

5.6 Parameters

Based on the mathematical model we have developed, the following paragraphs discuss the parameters that are regarded of importance in the industrial practice of neodymium electrolysis.

5.6.1 Operating temperature

Operating the electrolytic cell at a temperature where rare earth elements can be reduced as liquid state facilitates the separation of the product metal from the electrolyte, which minimizes the contamination of the reduced metal. Furthermore, this enables continuous operation of the electrolytic cell and maximizes production capacity.

5.6.2 Solubility of neodymium oxide

The solubility of the neodymium oxide is of importance in the electrolysis process. As the model indicates, the solubility of the oxide in the molten fluoride affects a) the equilibrium decomposition voltage of the reaction and b) the concentration terms, Σ_m and Σ_j , at the operating conditions.

The higher the solubility of the neodymium oxide in the salts the higher the activity of the oxide in the fluoride is, which results in lower equilibrium decomposition voltage. On the other hand, the concentration terms are more negative at higher solubility, which contributes to a lower voltage drop for the electrolysis process. Therefore, the overall effect of elevated solubility is to reduce the cell voltage for the electrolysis process, which is favorable.

5.6.3 Density and viscosity

The density and the viscosity of the molten salt have impact on the process mainly in two aspects. One is to affect the removal rate of the neodymium product from the cathode. The other

is affect the removal rate of the product gases from the anode. Both two aspects are critical in terms of the continuous process for production.

5.6.4 Electrical conductivity

It is noted that in Equation (5.80), as the electrical conductivity of the saturated electrolyte increases, the slope of Line bc, S , decreases and so does the cell voltage drop. A higher electrical conductivity is favorable in the process to reduce energy consumption. On the other hand, the electrical conductivity of the molten salt impacts the resistance of the melt and thus the Joule heat which is required to balance to heat loss in the process. The higher the electrical conductivity, the lower the resistance of the melt and the less the Joule heat is generated by the melt. The process can be self-sustaining in terms of melt temperature unless the Joule heat is sufficient to offset the heat loss.

5.6.5 Dissolution rate of neodymium oxide

The dissolution rate of neodymium oxide represents the effectiveness of the supply for the oxide from its source. It is restrained by the saturation state of the bulk solution when the current is lower than the critical current, i_c . Only at i_c , the dissolution rate reaches its maximum value and the supply of the oxide from the dissolution culminates. As the current further increases, the decomposition of neodymium fluoride occurs to offset the insufficient supply of neodymium oxide for the reaction.

It is worthwhile to note that the unit for the dissolution rate we discuss here is mole per second. One of the most effective approach of increasing the maximum dissolution rate of the oxide is to increase the contact surface area between the particle and the electrolyte per unit time, such as by adding more feeding points and reducing the particle size of the feed oxide.

5.6.6 Cell geometry

The configuration of the cell plays a substantial role in the electrolysis process. In Equation (5.80), the term $\frac{1}{2\pi h} \ln \frac{r_a}{r_c}$ (now defined as the geometry term, G) is shown to impact the slope of Line bc, S . The value of S increases with G , and hence, a small G is favorable to improve the process. Based on the expression of the term, G , it indicates that one can tune the term by increasing the depth of the electrolyte or/and decreasing the inter-electrode gap. The geometry term, G , differs for different types of electrolysis cells.

5.6.7 Heat Balance

A continuous electrolysis process to produce metallic neodymium requires to be self-sustaining in terms of operating temperature. The Joule heat due to the resistance of the salt is generated to balance the heat loss. In the $\Delta V_{ac} - i$ diagram, the Joule heat can be calculated as Si^2 at operating current, i along Line bc, and the area of $tos\Sigma_1$ represents this value.

5.6.8 PFCs Concentration in Offgas

The emission of PFCs is under restrict control to meet the emission regulation. The generation of PFCs from the electrolysis process is undesirable and the operating conditions are required to be adjusted when it occurs. The mathematical model developed in this chapter provides insights to enable one to use the offgas information to adjust the conditions in a proper manner to reduce, if not to eliminate, the PFCs generation.

We define

$$Y_{F/O} = \frac{X(F, PFCs)}{2X(O, CO_x)}$$

where $X(F, PFCs)$ represents the molar concentration of fluorine element in the offgas from PFCs generated from the electrolysis process and $X(O, CO_x)$ represents the molar concentration of oxygen element in the offgas from CO and CO₂.

According to the model, it gives

$$\gamma_{F/O} = \frac{i - i_c}{i_c}$$

where i is the operating current.

Then, we can determine the critical current as

$$i_c = \frac{i}{1 + \gamma_{F/O}}$$

With $\gamma_{F/O}$ determined, the current can be reduced to the critical current to prevent the generation of PFCs.

5.7 Conclusion

A mathematic model has been established and a diagram is used to illustrate the model in the discussion above. The relationship between the inter-electrode voltage drop and the current is shown to be determined by multiple parameters: theoretical decomposition voltage, activation overpotential, diffusivity of the ions, solubility of neodymium oxide, cell geometry, electrical conductivity of the electrolyte, density of the electrolyte, viscosity of the electrolyte, maximum dissolution rate of neodymium oxide in the melt and maximum mass transfer rate of the oxide into the bulk solution, etc.

The mathematical model can be used as a tool to conduct computational simulation on the electrolysis process to produce neodymium. The model can also be used for other similar electrolysis system such as for aluminum molten salt electrolysis.

The objectives to optimize the cell conditions and parameters are a) to increase the energy efficiency; b) to increase production capacity and c) to control the emission of perfluorocarbon gases. With the discussion above, the author concludes some thoughts on optimizing the electrolysis cell as follows:

- (1) In order to fulfil the goal of maximizing the capacity of the metal production and the energy efficiency, one should design the electrolytic cell and the molten salt in a way to adjust Point c to the further right bottom in the diagram. At the optimized Point c⁽ⁿ⁾, the maximum dissolution rate of the oxide equals the maximum mass transfer rate of the dissolved oxide into the bulk solution, that is, $\zeta_{d,m}^{max} = \chi_{bulk}^{max}$.
- (2) When the electrolytic process is operated at the current level less than the critical current, i_c , the generation of the perfluorocarbon gases can be avoided effectively. The optimal operating current for the cell is the corresponding critical current, i_c .
- (3) Operating the electrolysis process at the optimal capacity with the critical current, i_c is under the assumption that the anode effect does not occur on this condition. To operate the electrolytic process continuously, anode effect should be avoided so that the operating current, i , should be less than the anode-effect triggering current, i_{max} . If $i_c < i_{max}$, the optimal operating current is i_c to avoid the PFC generation and maximize production capacity; otherwise, the optimal operating current is i_{max} .
- (4) By adjusting the composition of the molten fluoride and the operating temperature, one can obtain a low intercept, Σ_1 , and a small slope, S , for Line bc.
- (5) Optimizing the depth of the melt and geometry of the cell, etc.

CHAPTER 6

MATHEMATICAL MODEL VALIDATION AND ELECTROWINNING OF NEODYMIUM IN THE NdF_3 -LiF SYSTEM

6.1 Introduction

This chapter aims to validate the mathematical model via experiments in the NdF_3 -LiF electrolyte system and carry out experiments to illustrate the effect of the anode surface area and the electrode distance on the electrolysis process. An experimental apparatus was designed and constructed to conduct the testwork of interest. First, a detailed description of the design of the experimental setup is given. After that, the experimental procedure is explained and then the results are presented with a discussion. Finally, conclusions are made regarding this chapter.

6.2 Experimental setup

A new experimental apparatus was designed and constructed to electro-reduce the neodymium oxide in the molten fluoride salts. Shown in Figure 6-1, which is not to scale, the heart of the apparatus is the electrolytic cell consisted of graphite anodes, one tungsten cathode, a tungsten collecting crucible and a graphite crucible. The temperature of the melt was determined by a thermocouple, Type K, protected by a closed-one-end Inconel tube when immersed in the melt. The graphite crucible was placed in the center of the stainless-steel canister and separated from the canister by a hot-pressed boron nitride plate to electrically insulate the canister during the electrolysis. Boron nitride has extremely high electrical resistance and excellent thermal conductivity.

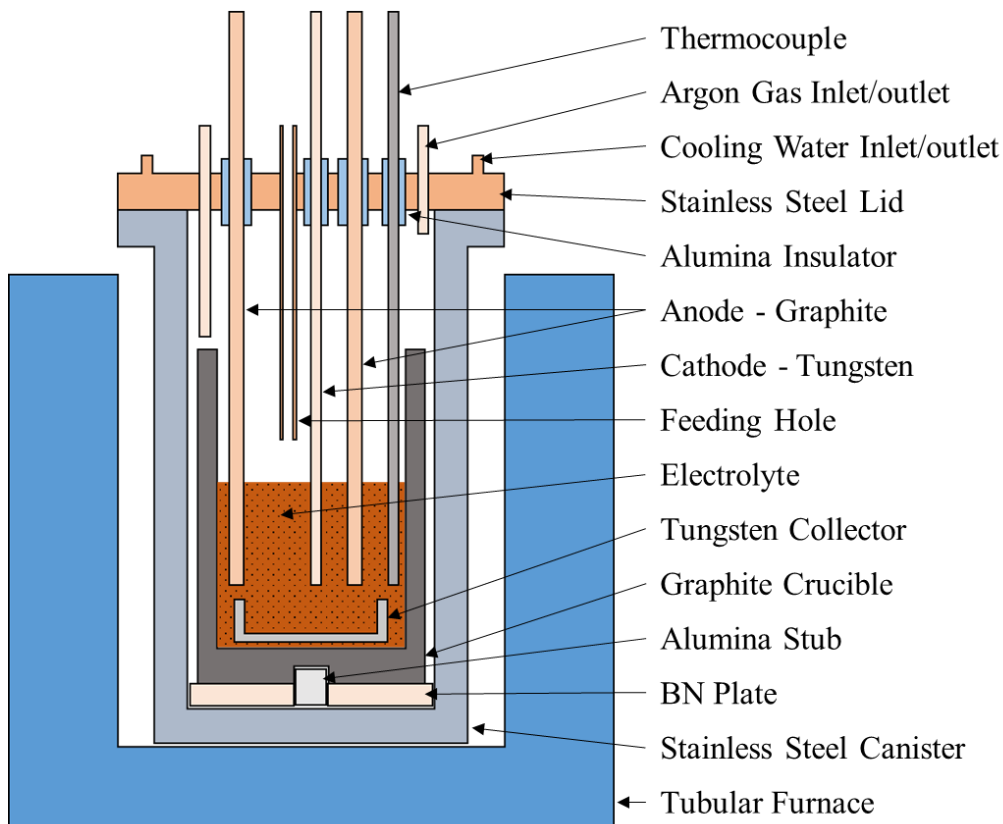


Figure 6-1 Schematic of the electrolytic cell setup

The anodes were made of graphite with purity of 99.99%, 9.525 mm in diameter and 61 cm in length, and the cathode was made of tungsten with purity of >99.95% and the same dimension as the anodes. The collecting crucible was machined out of tungsten (purity >99.95%) and the dimension was 101.6 mm OD X 91.4 mm ID X 33.0 mm tall X 5.1 mm deep with the inner wall tapered by 0.5 degree. The electrodes and the thermocouple were electrically insulated from the cell lid with alumina tubes of proper sizes. They were all movable through the use of two set screw shaft collars on each.

A graphite crucible of Grade GS served as the container of the. The crucible measured 132.1 mm OD X 121.9 mm ID X 228.6 mm tall X 203.2 mm deep. The inner wall was tapered by 0.5 degree to facilitate the removal of the fused salt.

The upper part of the canister is enclosed by a stainless-steel lid (SS316) with fittings attached and drilled through. A copper O-ring was placed in between to seal the flange. The design of the configuration of the lid is shown in Figure 6-3. The cell was purged with argon (99.998% purity) to displace the air in the cell through the inlet/outlet fittings. The coil made from a stainless-steel tube and attached to the lid was used to cool the lid and prevent it from overheating. The flow rate of the cooling water was adjusted to maintain the melt within the target temperature range.

A tubular furnace (Series CV12.5, Mellen Inc.) was used to heat the electrolyte cell to the target temperature and the temperature of the furnace was measured with a Type S thermocouple. The controller to the furnace communicated with a PC computer and the heating process was programmed and controlled via the PC. The thermocouple measuring the melt temperature was allowed to switch and connect to the controller so that the melt temperature was controlled with more accuracy. Once the melt thermocouple was switched, the furnace temperature was monitored through a temperature scanner (DP100AM, Omega Engineering) to protect the furnace, and an over temperature alarm would be triggered if the furnace was heated to above its limit temperature.

The electrical circuit for the electrolytic cell is illustrated in Figure 6-2. A DC power supply (XFR 20-60, Xantrex International) was adopted for the electrolytic cell system to provide direct current. The control over the current and voltage was achieved by manual manipulation. A calibrated shunt ($R_s = 0.001 \text{ ohm}$, 50 mV/50A) was installed in the circuit to determine the current with the voltage detection by a potentiostat. In order to monitor and collect the current/voltage data for the process, two Gamry Potentiostat/Galvanostat/Zero Resistance Ammeters (Interface 1000E and Interface 1010E, Gamry Instrument, USA) were employed to

measure the voltages. V_s and V represents the voltages over the shunt and the electrolytic cell, respectively. The current of the circuit, i , is determined by $i = V_s/R_s$. A $V - i$ diagram can be obtained during the electrolytic process. Figure 6-4 and Figure 6-5 are the pictures of the apparatus for the electrolysis cell.

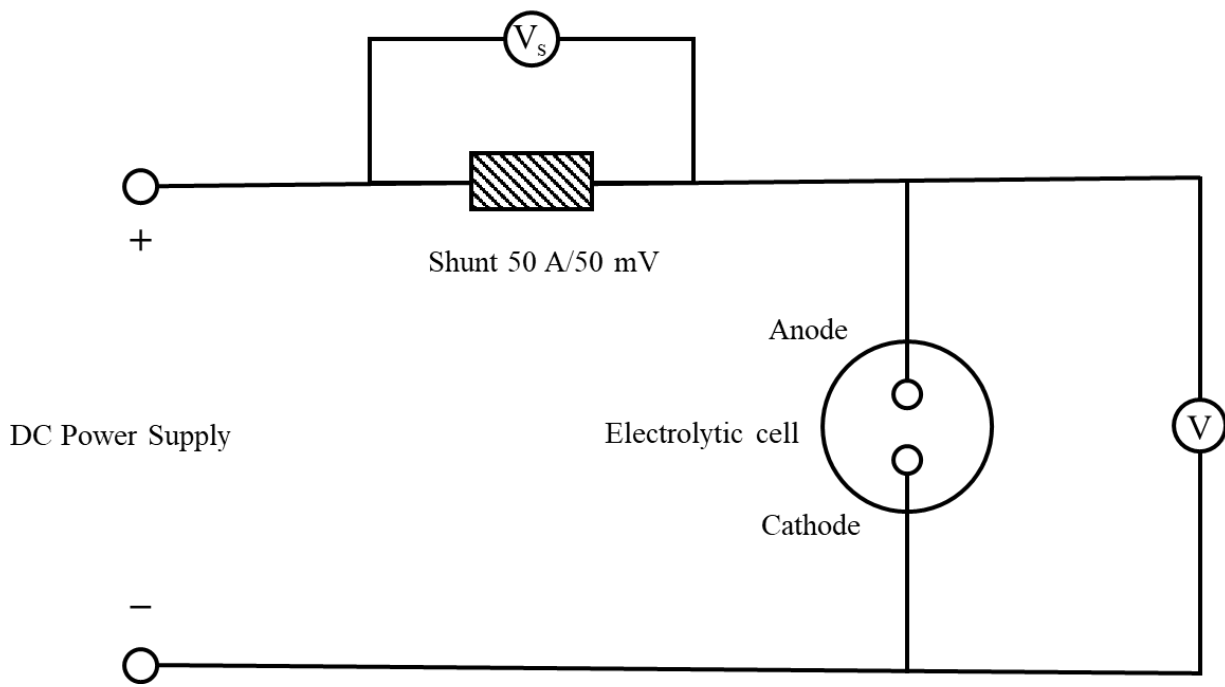


Figure 6-2 Electrical circuit schematic for the electrolytic cell

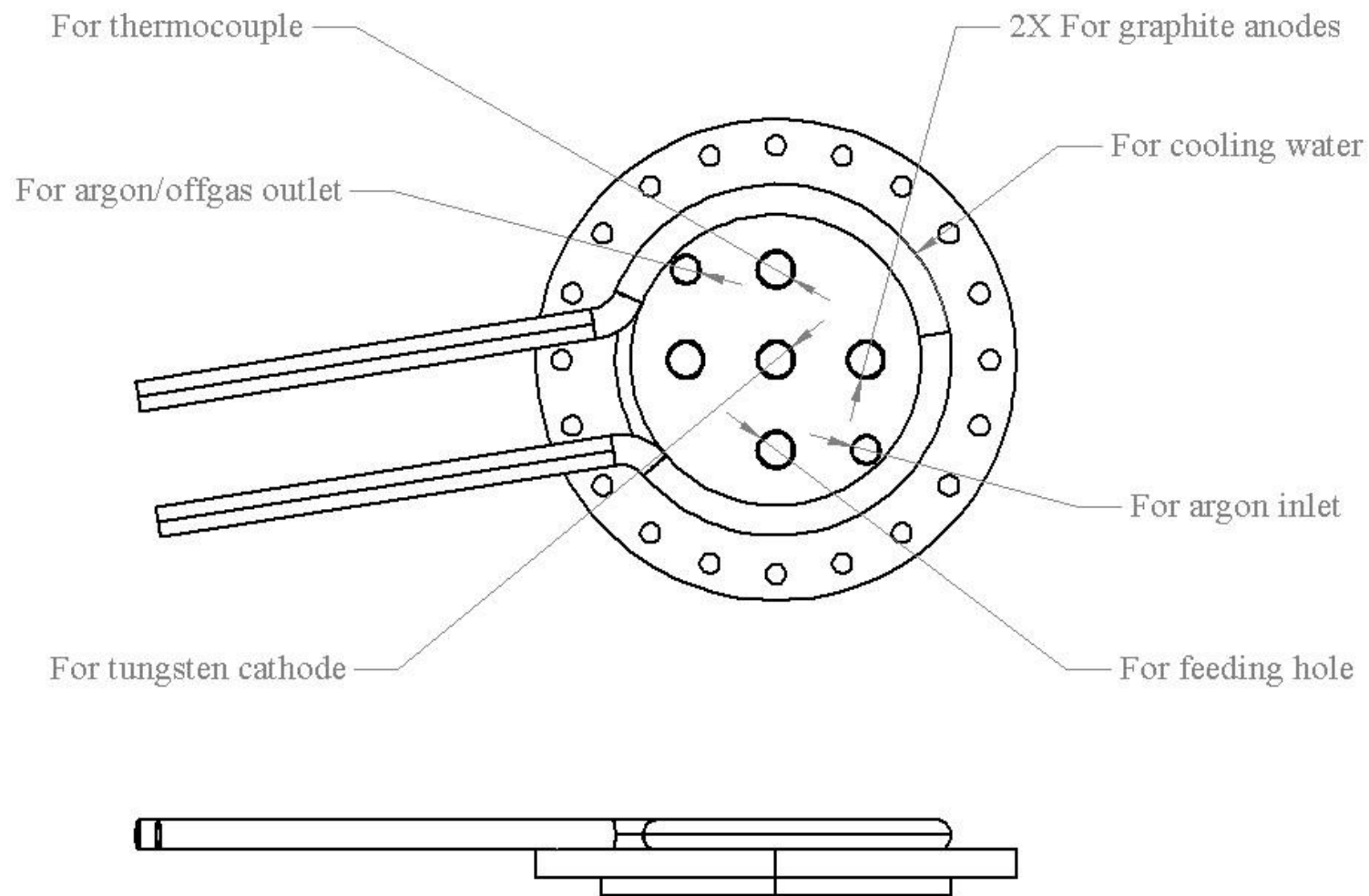


Figure 6-3 Configuration of cell lid for electrolysis cell (distance between anode and cathode: 1.5 inches (3.81 cm); electrode diameter: 3/8 inch (0.9525 cm))

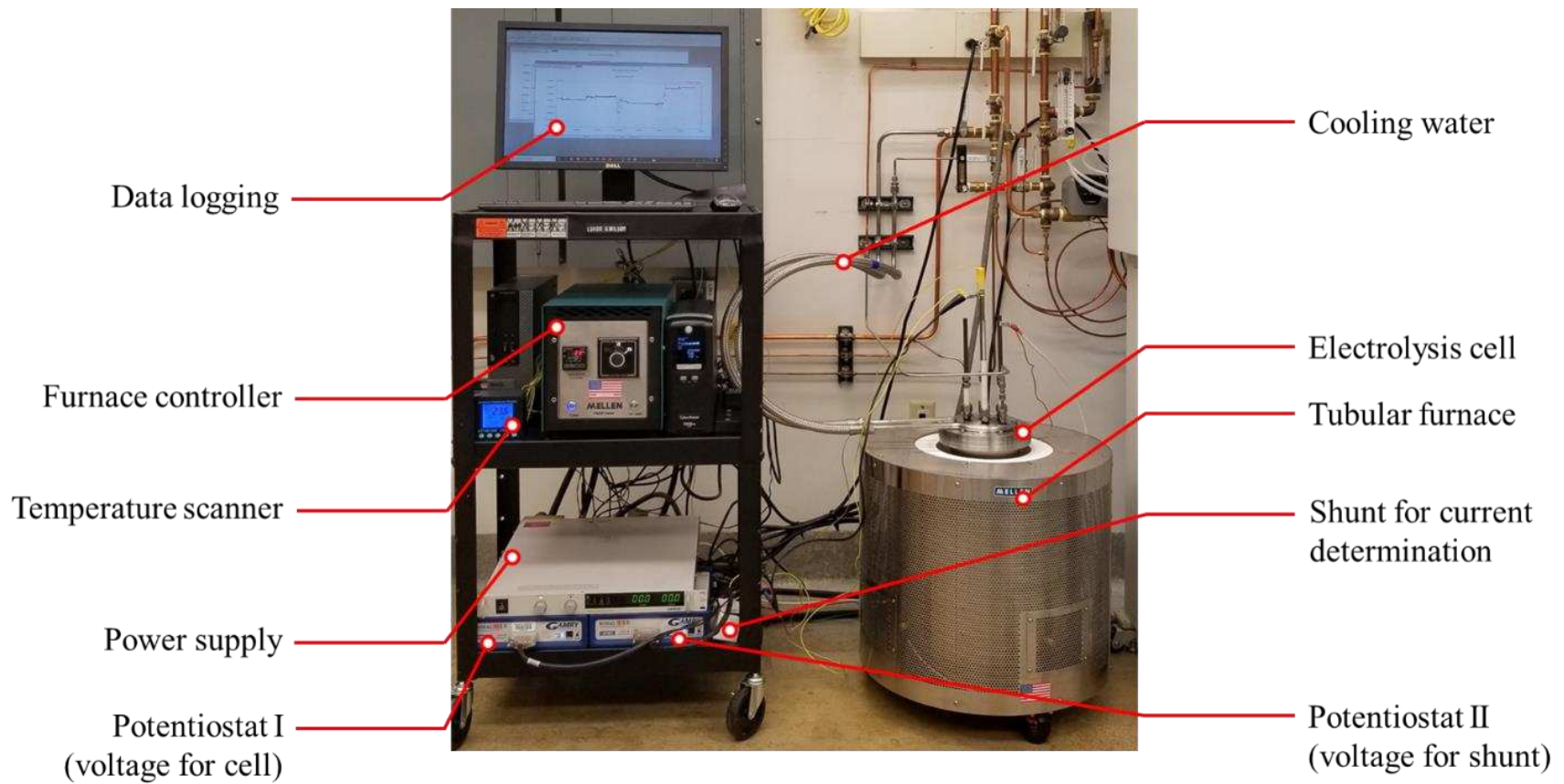


Figure 6-4 Setup of the electrolysis test system

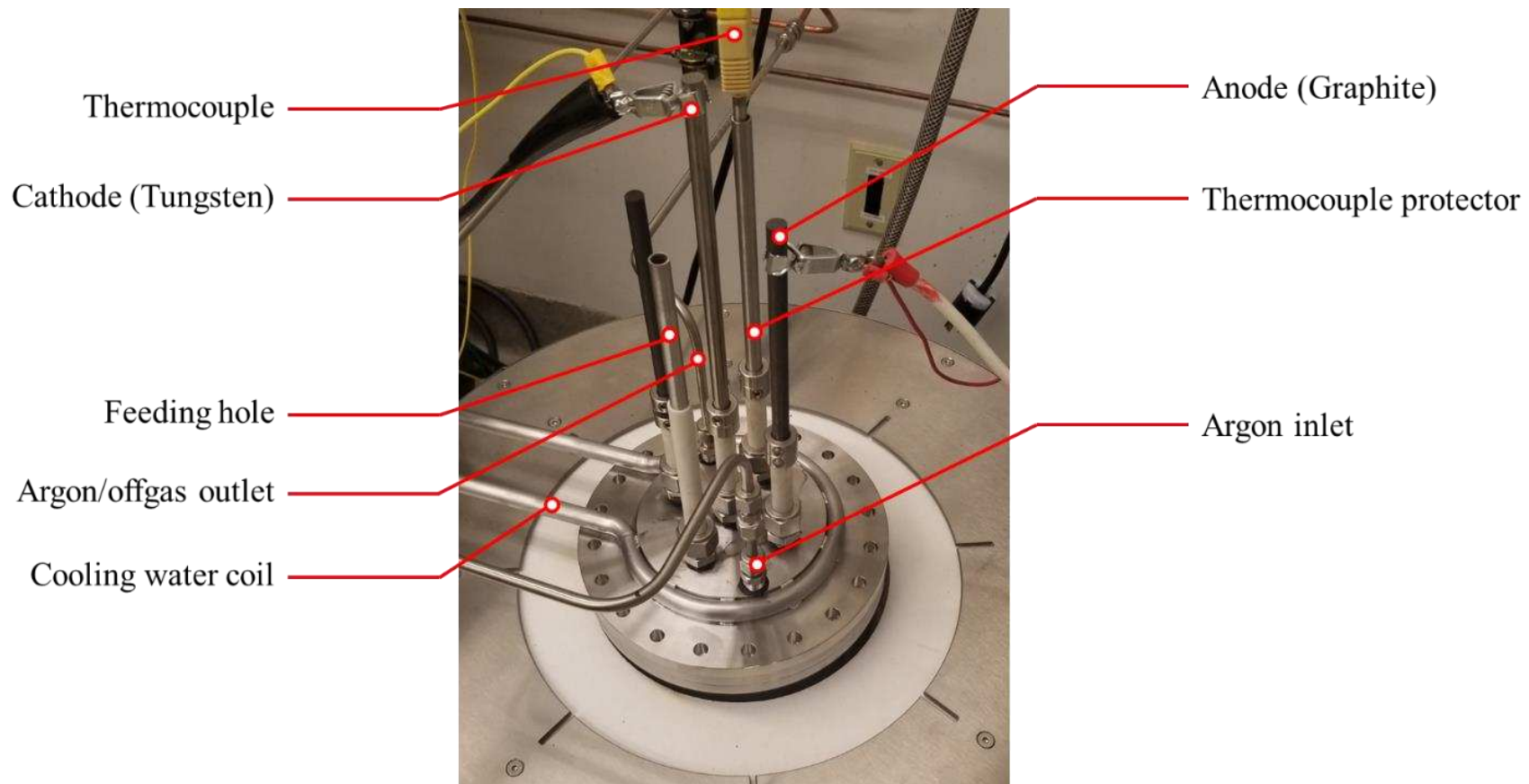


Figure 6-5 Photograph of the configuration of the electrolytic cell

6.3 Experimental procedures

6.3.1 Sample preparation

Drying chemicals. Weigh proper amount of NdF_3 , LiF and Nd_2O_3 separately and dry the sample in the oven at $200\text{ }^\circ\text{C}$ overnight.

Mixing salts. Mix the fluorides based on the required electrolyte composition by adding the chemicals in alternating layers.

6.3.2 Operational procedures

The mixed fluoride salt was loaded in the graphite crucible, which was then placed in the center of the canister. The cell was assembled as Figure 6-1 illustrates except that the electrodes and the thermocouple were held above the sample. The controller was programmed to heat the furnace to $200\text{ }^\circ\text{C}$ and hold the temperature for two hours to remove the moisture in the sample. After that, the cell was purged with argon as protective gas constantly. The furnace was heated to 500 K h^{-1} to $1050\text{ }^\circ\text{C}$ and held this temperature for two hours to allow the salts to melt.

The electrodes and the thermocouple were lowered to positions in the melt and the controller setting was changed to switch to allow the melt thermocouple signal to be used to control the heating process of the furnace. The temperature of the furnace chamber was continued to be monitored to prevent overheating.

The oxide(s) weighing 3 wt% of the melt was added through the feeding hole. When the melt temperature reached $1050\text{ }^\circ\text{C}$ and was then held for equilibrium for two hours.

The circuit for the test was connected according to the demonstration in Figure 6-2. Electrolysis was conducted to produce rare earth metals. In a continuous electrolysis process, the corresponding oxide was added consistently according to the theoretical consumption of the

oxide while electrowinning. An assumed current yield of 100% was used. In the actual electrolysis especially in large scale, there is little electronic conduction and the recombination effect of CO/CO₂ on the metal will reduce the production rate and hence the current yield.

Current or voltage was adjusted for the electrolysis. During the electrolysis tests, the voltages over the shunt and the electrolysis cell were measured and recorded by the Gamry potentiostats. The current passing through the circuit was determined as the voltage over the shunt divided by its known value of resistance.

6.4 Experimental results and discussion

6.4.1 Scoping study for electrolysis tests

A series of scoping studies were carried out with the electrolysis cell with NdF₃-LiF molten salt of 85 wt% NdF₃. The input of NdF₃ (99.5% purity) was 2290.3 grams and that of LiF was 404.5 grams. 3 wt% Nd₂O₃ were added to the salt to saturate the fluoride before the electrolysis. The depth of the melt was about 60 mm in the graphite crucible. The conditions for the tests are listed in Table 6-1. In the experiments, the current increased by a certain ramp (here one amp. per minute). Neodymium oxide was added to the melt simultaneously to compensate for its consumption during electrolysis, the amount of which was determined stoichiometrically according to the instantaneous current. The oxide was added every 30 seconds. The values of current and cell voltage were monitored and recorded real time.

Figure 6-6 through Figure 6-8 depict the cell voltage change with increasing current for the tests. The curve patterns of the cell voltages against current in the figures are congruent with that of the proposed mathematical model in CHAPTER 5 (Figure 5-5). As stated in the model, when the current is small, the decomposition of Nd₂O₃ does not reach equilibrium due to the low partial pressure of the produced carbon monoxide at the anode surface, resulting in a relatively

smaller value of decomposition voltage. After the anode surface is completely occupied by the decomposition half reaction, the partial pressure of CO equals unity and the reaction reaches equilibrium. The cell voltage increases proportionally with the increase of current until either the decomposition of NdF_3 is triggered or the anode effect occurs. The former case happens with the insufficient supply of Nd_2O_3 to compensate for the electron transfer reaction with high current. The corresponding current at the beginning of the NdF_3 decomposition is defined as critical current (i_c). The cell voltage drops by a distinct amount due to the lack of equilibrium for the NdF_3 decomposition reaction at a low redundant current level. The incipience of anode effect terminates the cell reaction at a current defined as limiting current (i_{max}). The limiting current can be smaller than the critical current (as shown in Figure 6-7 and Figure 6-8), or it can be greater than the critical current (as shown in Figure 6-6). Similar observations were reported by Keller and coworkers (Keller and Larimer 1997), as shown in Figure 6-9. The generation of CF_4 was observed when current was exceeding the critical current.

Table 6-1 Experiment conditions for scoping study tests of neodymium electrolysis: 85 wt% NdF_3 , 1050 °C

Exp. No.	Cathode depth, h_c (cm)	Anode depth, h_a (cm)	Anode number	Anode surface area, A (cm^2)	Current ramp (A/min)
1	3.8	2.8	2	16.75	1
2	3.8	3.8	2	22.73	1
3	3.8	2.8	1	8.37	1

The analysis results for the curves obtained in the scoping tests are listed in Table 6-2. Point a represents the start of electrolysis at $i = 0$. Point b marks when the decomposition of

Nd_2O_3 reaches equilibrium. Point c is the point at which the decomposition of NdF_3 commences.

Point m is the case when the anode effect occurs. Line bc or bm is expressed as

$$\Delta V_{ac} = \Sigma_1 + Si$$

where Σ_1 is the intercept and S is the slope of the line.

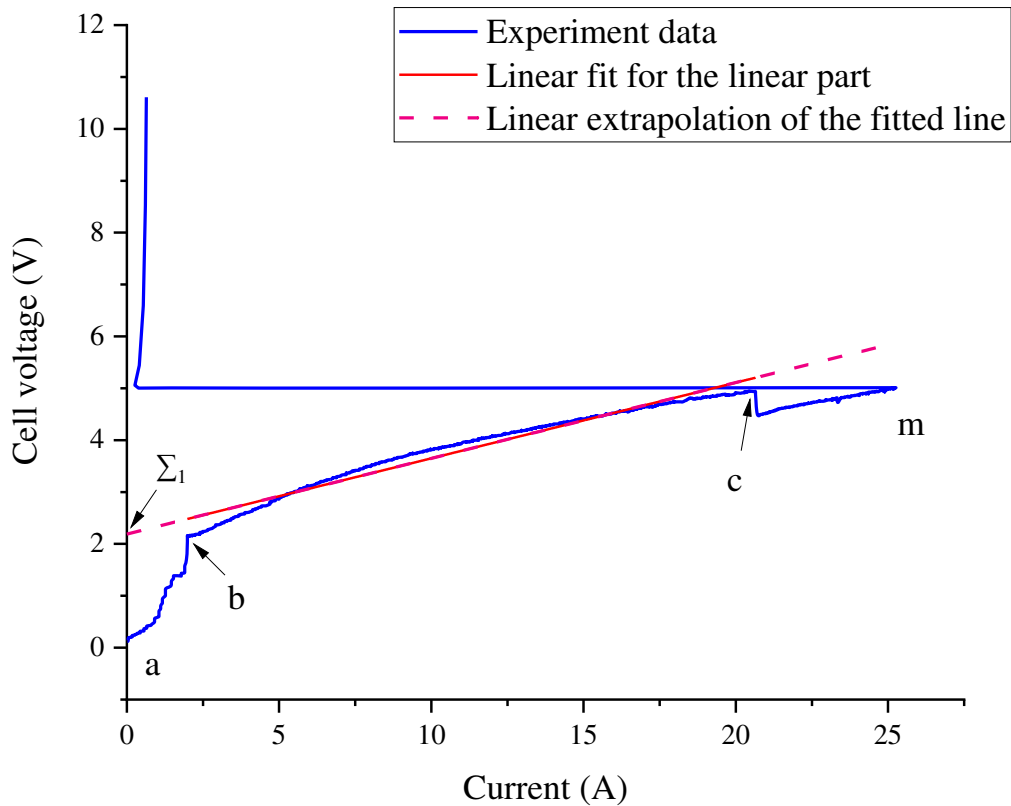


Figure 6-6 Cell voltage curve with increasing current (Exp. 1: two anodes, 2.8 cm submerged depth)

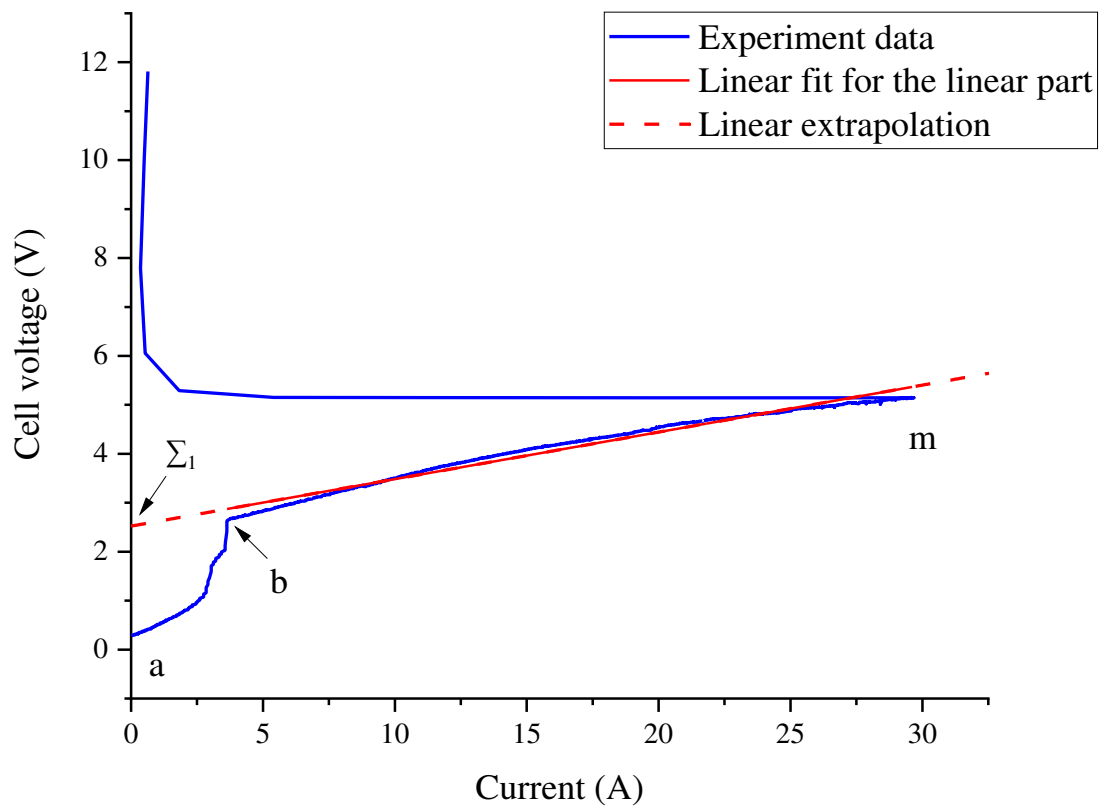


Figure 6-7 Cell voltage curve with increasing current (Exp. 2: 2 anodes, 3.8 cm submerged depth)

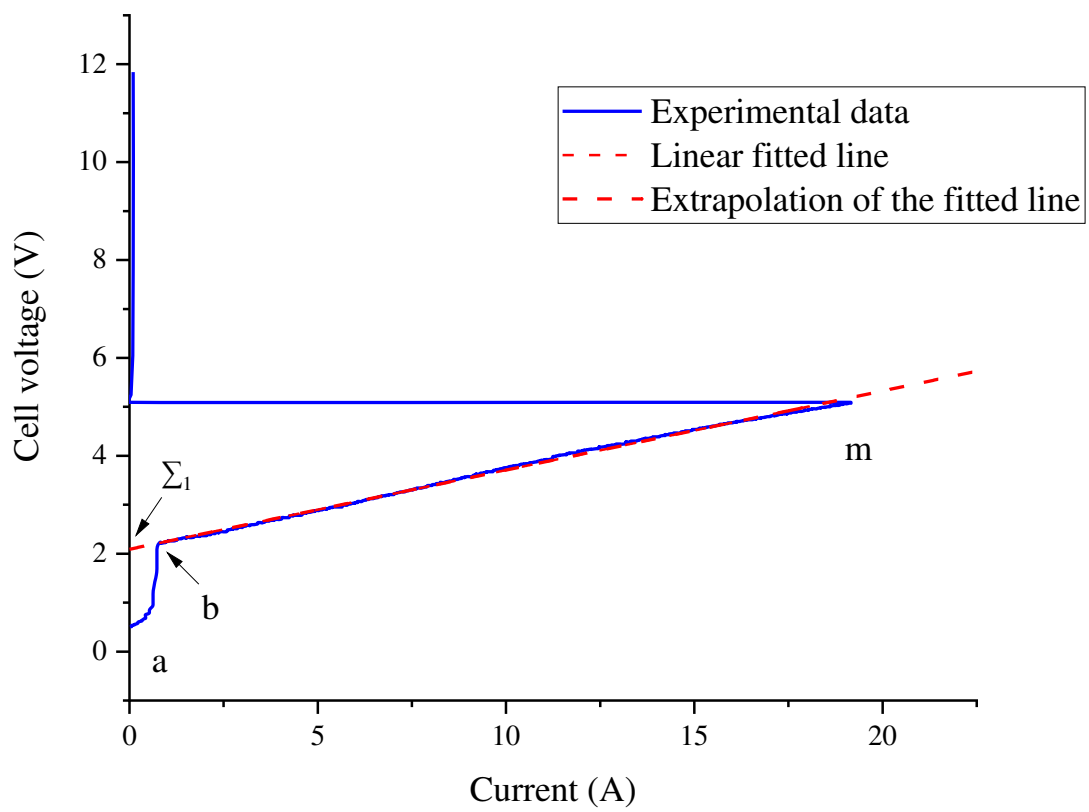


Figure 6-8 Cell voltage curve with increasing current (Exp. 3: 1 anodes, 2.8 cm submerged depth)

Table 6-2 Analysis results for scoping study tests of neodymium electrolysis: 85 wt% NdF₃, 1050 °C

Exp. No.	Linear line			Point b			Point c		Point m		Anode effect current density (A cm ⁻²)
	Intercept, Σ_1 (V)	Slope, S (ohm)	Adj. R-Square	Current (A)	Voltage (V)	Current Density (A cm ⁻²)	Current (A)	Voltage (V)	Current (A)	Voltage (V)	
1	2.19014	0.14579	0.96801	1.987	2.112	0.120	20.659	4.934	25.31	5.003	1.509
2	2.52273	0.09602	0.97893	3.641	2.629	0.162	-	-	29.66	5.146	1.306
3	2.09128	0.16167	0.99774	0.788	2.216	0.097	-	-	19.16	5.093	2.288

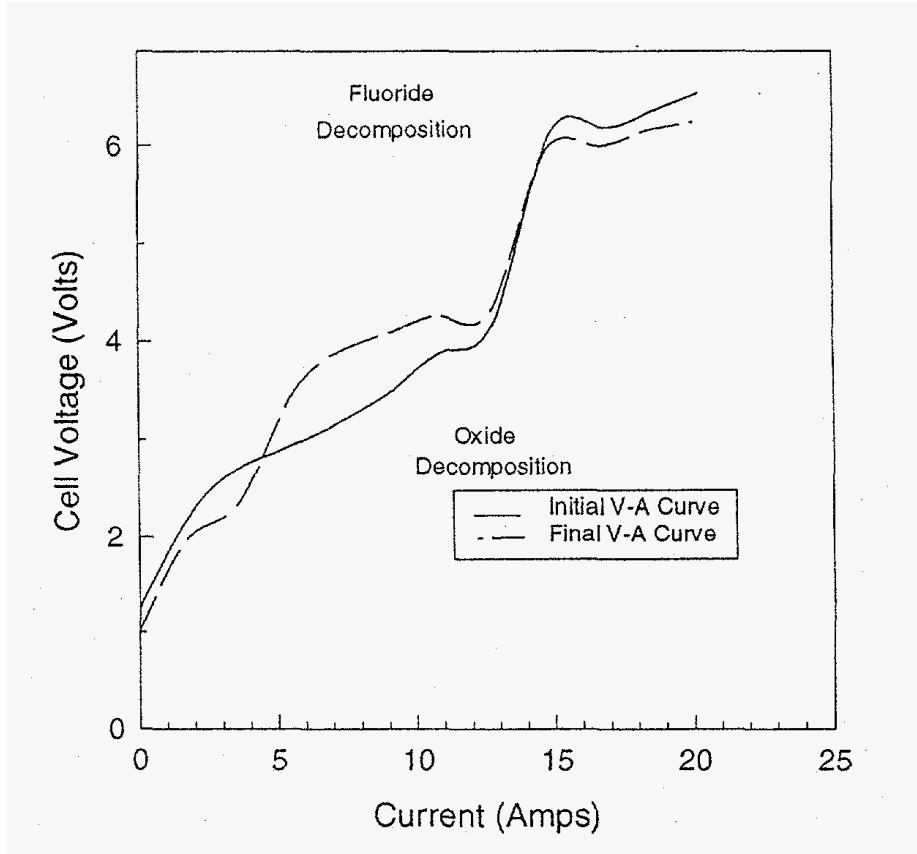


Figure 6-9 Current-voltage characteristics (Keller and Larimer 1997): Nd_2O_3 fed into the NdF_3 - CaF_2 - LiF (60-20-20 wt%) salt for electrolysis, 920 °C

In Figure 6-6 (Experiment 1), at voltage 0.19V (point a), the electrical circuit is closed with the initiation of the decomposition of Nd_2O_3 . With the increase of the current, from point a to point b, the controlling step of the process rate transitions from the decompositional chemical reaction to the diffusion throughout the diffusional layers. A straight line is observed from point b to point c, within the range of which the decomposition of Nd_2O_3 continues with the increase of the current. The required amount of Nd_2O_3 is dissolved and transferred to the electrodes sufficiently for the reaction. Line bc in this experiment was linear fit to an equation as follows:

$$\Delta V_{cell}(V) = 2.19014 + 0.14579 \times i(A)$$

However, at point c, either the dissolution rate of the oxide or the mass transfer rate for the dissolved Nd_2O_3 reaches the maximum level at this critical current (20.65 A) so that the abundant current results in the decomposition of NdF_3 simultaneously as the current increases. Thus, point c represents the initial occurrence of the decomposition of NdF_3 . The voltage is observed with a distinct drop at point c due to the low partial pressure of the gas product (CF_4) at the initial current level for the NdF_3 decomposition. The percentage of the NdF_3 decomposition increased with the current. With the current exceeds 25.26 A, a sudden plummet of current occurs, and no current is detected even though the voltage is increased. This is attributed to the extremely rapid generation of gas products (CO , CO_2 , and CF_4). The off gases are not able to be effectively released from the electrolyte and partially trapped at the anode. The accumulated gas forms a film that insulates the electrolyte from the anode and causes the termination of the electrolysis process.

The situations for Experiment 2 and 3 are similar except that there is no occurrence of Point c before the anode effect commences. The feeding methods for those experiments are the same. An explanation for no presence of Point c in Figure 6-7 (Experiment 2) at 20.65 A as it is for Experiment 1 is that the Nd_2O_3 powder fed into the melt was too fine ($<52 \mu\text{m}$). This caused that the added powder floats on top of the melt and with the interference of the injected argon the powder may suspends over the melt. Inconsistency of the amount of contact surface areas resulted in the difference between the two experiments regarding the occurrence of Point c.

As can be seen from Figure 6-10, the equilibrium current at Point b increases with increasing anode surface area. It is reasonable because the more anode surface area the higher current throughput it takes to make complete use of the surface to produce gas products and for the reaction to reach equilibrium.

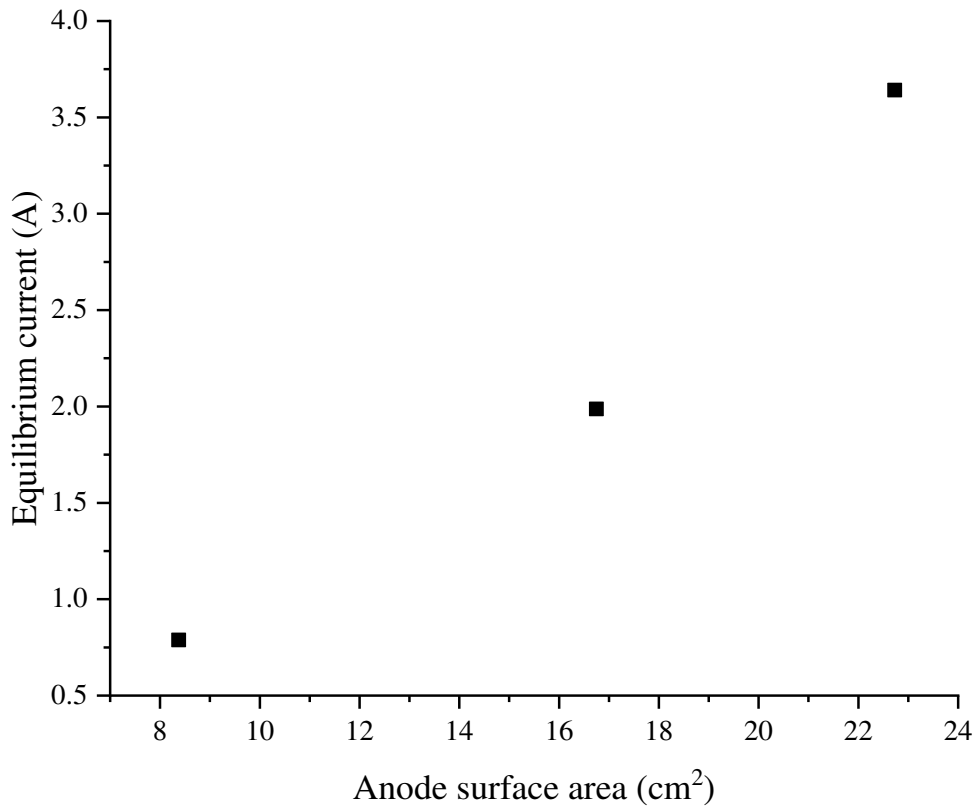


Figure 6-10 Analysis for the equilibrium current (Point b) with changing anode surface area

Figure 6-11 illustrates the impact of the anode surface area on the limiting current. As shown in the figure, the limiting current increases linearly with the anode surface area. A linear least square regression is carried out for the result and it demonstrates a high correlation for the linear relationship with R-square up to 0.9999.

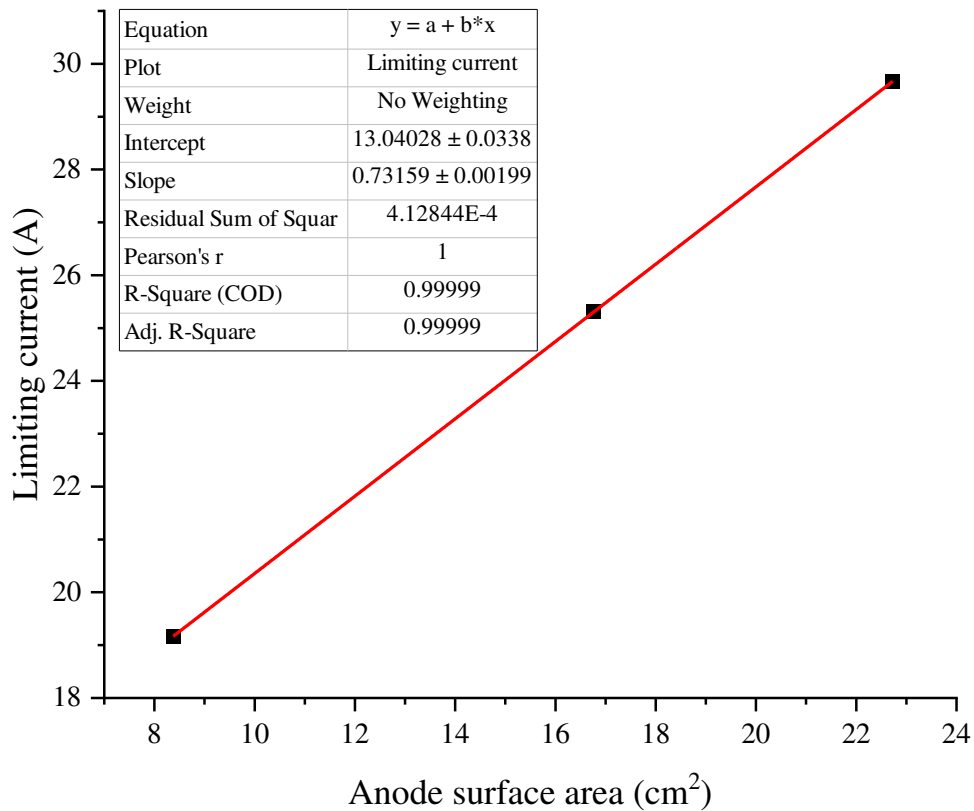


Figure 6-11 The limiting currents for the scoping study electrolysis tests with changing anode surface area

6.4.2 Impact of anode surface area on the electrolysis process

The impact of the anode surface area on the electrolysis process was studied by varying the submerged depth of the anode in the melt. In this group of experiments, the content of NdF_3 in the $\text{NdF}_3\text{-LiF}$ salt was 85 wt%. Nd_2O_3 was added to saturate the salt at $1050\text{ }^\circ\text{C}$ with 3 % of the total fluoride mass. During the electrolysis process, the current was controlled with a ramp of three amperes per minute from zero until it reached its limiting current for anode effect. Nd_2O_3 was continuously fed into the melt at a rate calculated to compensate stoichiometrically for the oxide consumption at the electrodes. The values of the current and cell voltage were monitored

and recorded real time. Table 6-3 lists the experimental parameters for this group of experiments. From Experiments 9 to 15, the graphite anode was used adjusted to different depths into the melt. In Experiment 16, two anodes were used.

Table 6-3 Experiment conditions for anode surface area study tests of neodymium electrolysis: 85% NdF₃, 1050 °C

Exp. No.	Cathode depth, h_c (cm)	Anode depth, h_a (cm)	Anode number	Anode surface area, A (cm ²)	Current ramp (A/min)
9	6.5	1.1	1	3.29	3
10	6.5	1.9	1	5.68	3
11	6.5	2.6	1	7.78	3
12	6.5	3.6	1	10.77	3
13	6.5	4.3	1	12.86	3
14	6.5	5.5	1	16.45	3
15	6.5	6.5	1	19.44	3
16	6.5	6.5	2	38.88	3

Figure 6-12 and Figure 6-14 illustrate the cell voltage change with varying current. The current density is analyzed for Exp. 9 to 15 in Figure 6-13. Table 6-4 lists the analysis results to interpret the figures.

As can be seen in Figure 6-12 and Figure 6-14, the equilibrium currents for each experiment increased with increasing submerged depth of the anodes. There is no indication of NdF₃ decomposition because the straight line between the equilibrium point and the limiting current is not interrupted. The limiting current and the corresponding cell voltage both increase with the submerged depth of the anode.

In Table 6-4, it is found that the values of Σ_1 fluctuate from 1.62 V to 2.12 V and the average of Σ_1 is 1.817 V with standard deviation of 0.162 V. The current density at the onset of the anode effect increases with the anode surface area varying within a low range from 1.30 A cm⁻² to 1.71 A cm⁻² with an average of 1.54 A cm⁻² when the surface area reaches about 10 cm².

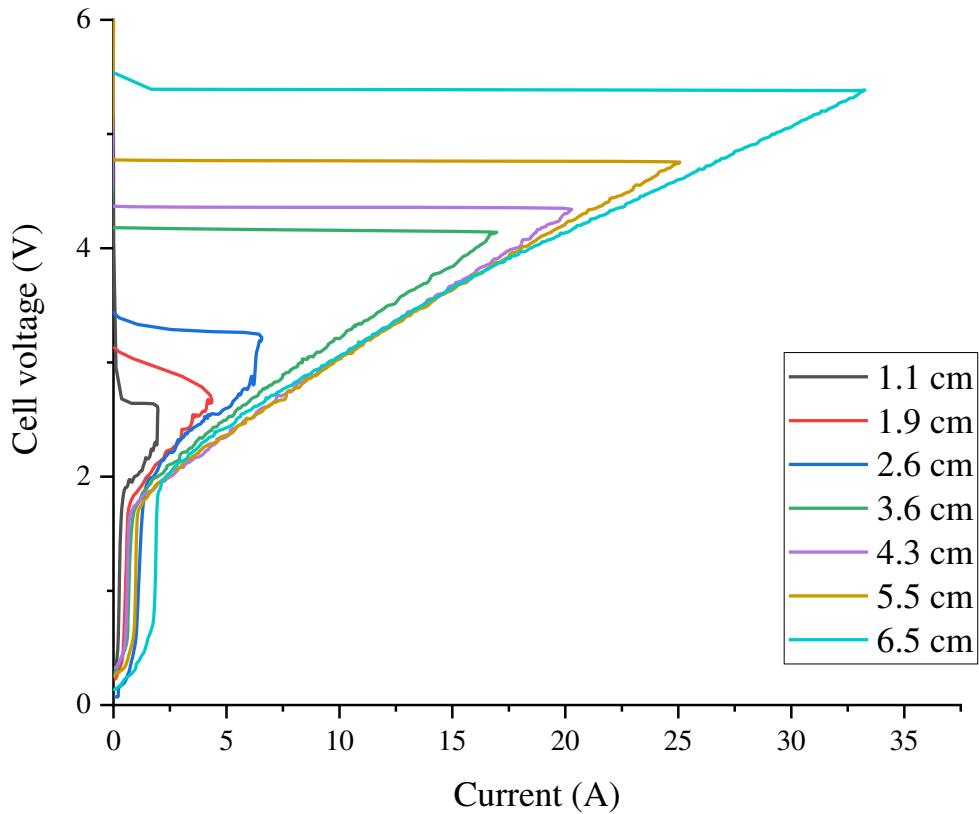


Figure 6-12 Cell voltage change with the change of current (Exp. 9 – 15)

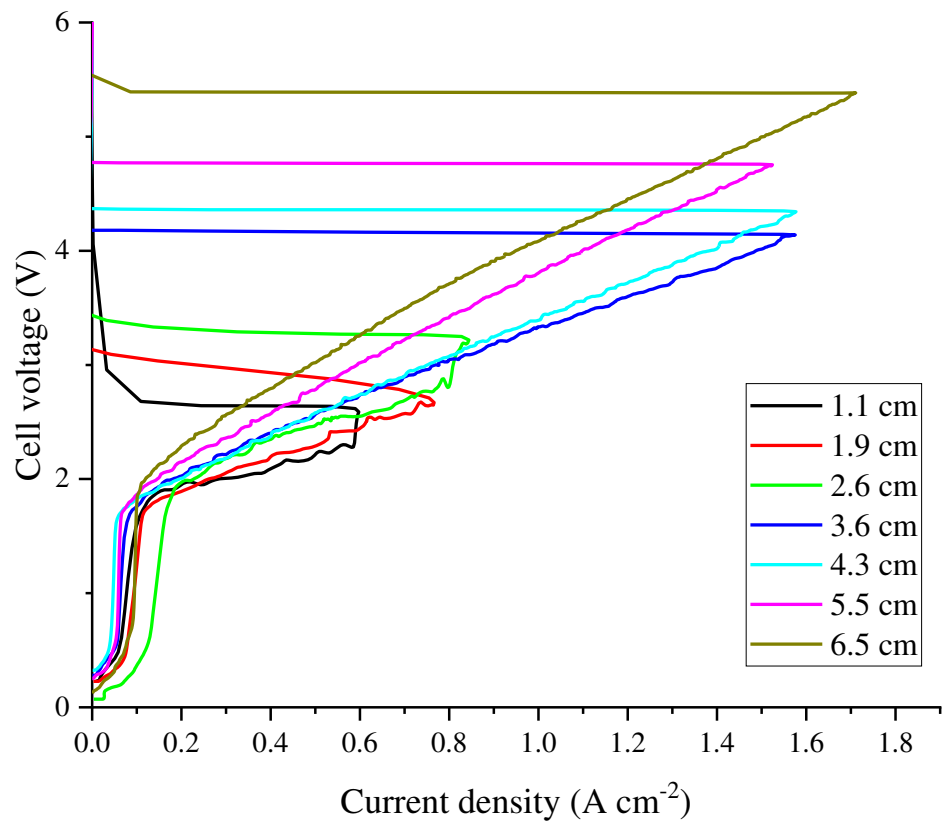


Figure 6-13 Cell voltage at varying current density (Exp. 9 – 15)

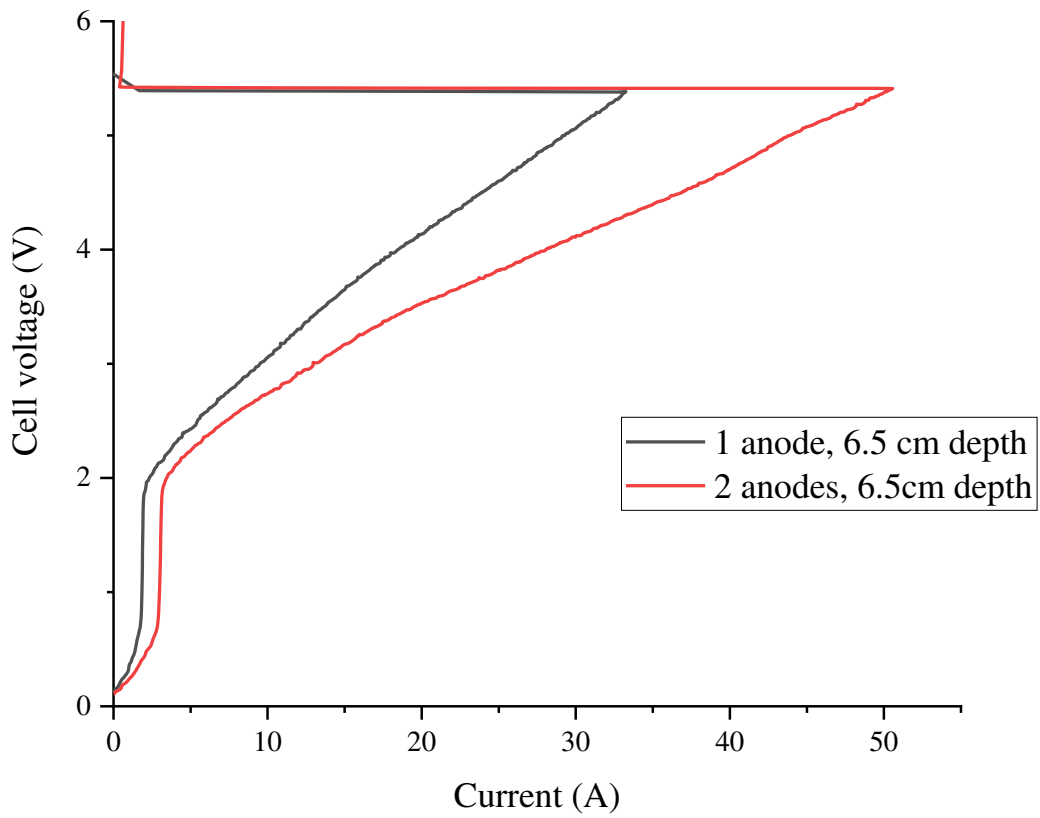


Figure 6-14 Cell voltage with changing current (Exp. 15 vs. Exp. 16)

Table 6-4 Analysis results for electrolysis experiments

Exp. No.	Linear line					Point m		Anode effect current density (A cm ⁻²)
	Intercept, Σ_1 (V)	Standard error for Σ_1 (V)	Slope, S (ohm)	Standard error for S (ohm)	Adj. R-Square	Current (A)	Voltage (V)	
9	1.72899	0.00768	0.29063	0.00587	0.97648	1.965	2.589	0.60
10	1.62385	0.00516	0.24619	0.0019	0.99262	4.355	2.67	0.77
11	1.77086	0.00923	0.17527	0.00237	0.96917	6.574	3.222	0.85
12	1.80219	0.003	0.13958	3.09E-04	0.99712	16.96	4.139	1.58
13	1.70723	0.002	0.13093	1.69E-04	0.99877	20.28	4.342	1.58
14	1.78587	0.00266	0.12123	1.78E-04	0.99805	25.07	4.753	1.52
15	1.99889	0.00437	0.10424	2.19E-04	0.99474	33.26	5.383	1.71
16	2.11839	0.00352	0.06585	1.19E-04	0.99439	50.57	5.411	1.30

Figure 6-15 depicts the limiting current changes with the anode surface area for the experiment. As can be seen, it increases with the surface area but not linearly throughout the range of the area studied. We notice that the cathode is stationary throughout the tests. For the anode submerged in the range of first half of the cathode depth, the relationship between the limiting current and the surface is linear. This remains true for the second half of the cathode depth range but the linear relationship varies. When the depth of the anodes is levelled with that of the cathode, a change of the slope for the linear relationship is observed. The explanation for this might be that the electrical field between the anode and cathode varies with changing anode depth and when the change becomes significant, it affects the linear relationship.

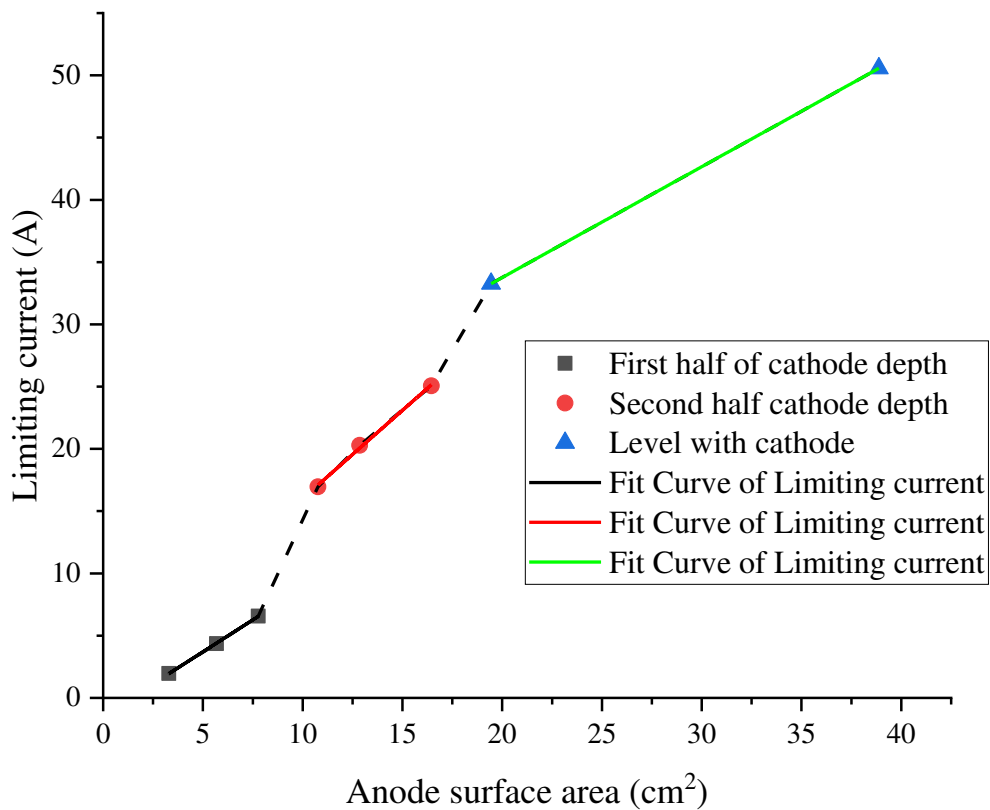


Figure 6-15 Limiting current changes with anode surface area

As defined in CHAPTER 5, the geometry term of the electrolysis cell, G , is the equivalent electrode distance divided by the equivalent cross-sectional area. The unit of G is cm^{-1} .

¹. In the mathematical expression of the model, it gives

$$S = \frac{G}{\kappa_{\text{salt}}} \quad (6.1)$$

Then, Equation (6.1) can be rewritten as

$$G = S\kappa_{\text{salt}} \quad (6.2)$$

With the slope information listed in Table 6-4, the values of the geometry term, G , were calculated according to Equation (6.2). The electrical conductivity of the salt was measured in CHAPTER 4 with a value of $4.908 \text{ ohm}^{-1} \text{ cm}^{-1}$. The values of G are listed in Table 6-5.

Table 6-5 Calculated parameters for electrolysis test results

Exp. No.	Overall overpotential, η_{overall} (V)	Geometry term, G (cm^{-1})	Thermal energy generated at limiting current, ΔH (J s^{-1})	Theoretical limiting current energy efficiency, μ_{max} (%)
9	0.399	1.427	1.12	77.94
10	0.294	1.208	4.67	59.84
11	0.441	0.860	7.57	64.24
12	0.472	0.685	40.15	42.81
13	0.377	0.643	53.85	38.85
14	0.456	0.595	76.19	36.06
15	0.669	0.512	115.31	35.59
16	0.788	0.323	168.40	38.46

The geometry term G varies with the change of the relative position of the electrodes. Define γ as the depth ratio of anode to cathode. When $0 < \gamma < 1$, an infinitesimal on the direction of electrode distance is taken to calculate the geometry term G and it gives

$$dG = \frac{d l_x}{h_c(1 - \frac{1-\gamma}{l})l_x} \quad (6.3)$$

With the integral taken from electrode distance 0 to l for the equation above, we have

$$G = \frac{l \ln \gamma}{D h_c (\gamma - 1)} \quad (6.4)$$

For $\gamma = 1$, it gives

$$G = \frac{l}{D h_c} \quad (6.5)$$

With the electrical conductivity known, Equation (6.2) is used to determine the slope of line bm for each case. Figure 6-16 compares the calculated slope results based on Equation (6.4) and those collected from the experimental results. It indicates that the results calculated with the equations we proposed show good congruence with the experimental results, which means that the entire depth of the cathode contributes to the half-cell reaction and thus the charge distribution on the surface of the anode is not uniform. It is reasonable to argue that due to the unevenness of the anode and the cathode in depth when $0 < \gamma < 1$, there is a charge density gradient from the top of the submerged anode part to the bottom at the surface of the anode, and the bottom surface area obtains the highest charge density as the current goes through. Hence, the current density at the bottom surface of the anode is the highest and it decreases gradually from the bottom to the top submerged surface area.

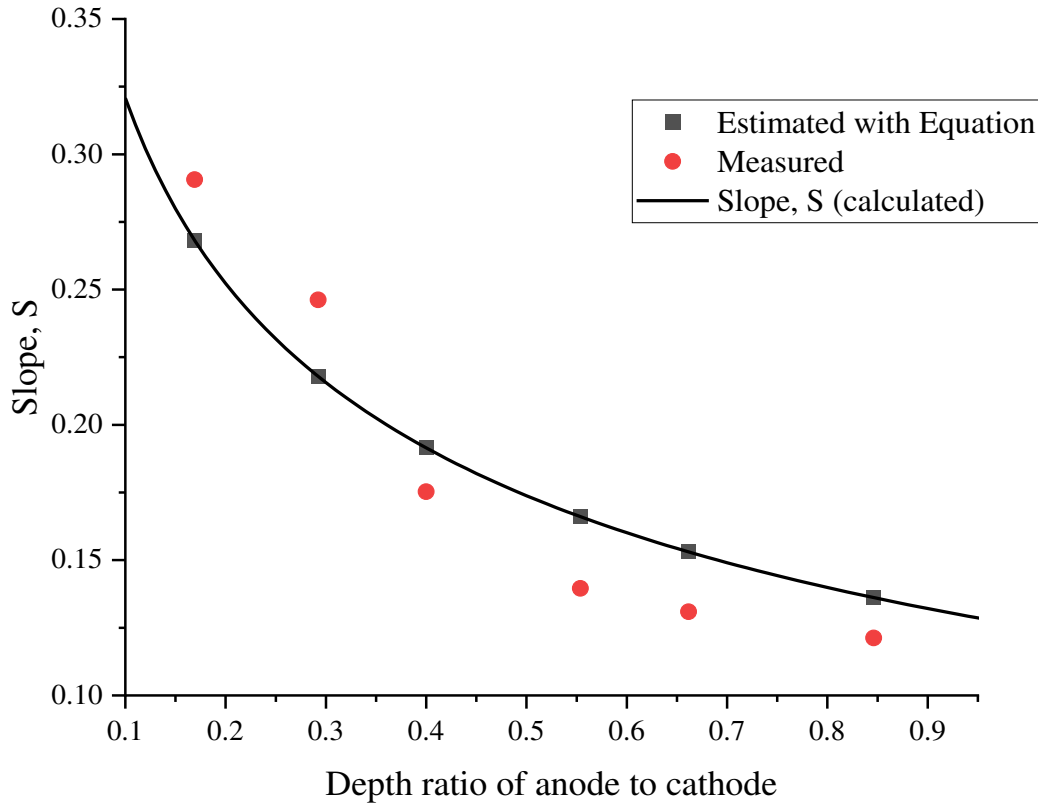


Figure 6-16 The comparison of the slopes for each case in the experiments between the calculated results using Equation (6.4) and the experimental results.

Overall overpotential is defined as

$$\eta_{overall} = \Sigma_1 - \Delta V_d^{eq} \quad (6.6)$$

where ΔV_d^{eq} is the equilibrium decomposition voltage of the reaction. In this group of experiments, it represents that of Nd_2O_3 and is determined by the following equation:

$$\Delta V_d^{eq} = \Delta V_d^0 - \frac{1}{n_1 F} RT \ln a_{\text{Nd}_2\text{O}_3} \quad (6.7)$$

It is assumed that the activity coefficient for Nd_2O_3 in the salt is unity. Then, it gives

$$a_{\text{Nd}_2\text{O}_3} = X_{\text{Nd}_2\text{O}_3}$$

Substituting

$$X_{Nd_2O_3} = 0.391$$

we have

$$\Delta V_d^{eq} = 1.330 V$$

Then the values for the overall overpotential for each electrolysis condition are calculated by Equation (6.6) and listed in Table 6-5.

Figure 6-17 depicts the change of limiting cell voltage against the anode surface area. The results are fitted with the Boltzmann equation as follows:

$$\Delta V_{max} = A2 + \frac{(A1 - A2)}{1 + e^{\frac{A-x0}{dx}}} \quad (6.8)$$

where ΔV_{max} is the limiting cell voltage at limiting current, A is the anode surface area and A1, A2, x0 and dx are the corresponding coefficients for Boltzmann fitting. It is noticed that high correlation is achieved with the Boltzmann fit as R-square equals 0.99971.

This equation describes that the limiting current is anode surface area dependent. It is noticed that the term A1 in the equation is 2.024 ± 0.586 , which is close to the average of Σ_1 (1.817 ± 0.162). Σ_1 is the theoretical potential for the electrolysis to be triggered for equilibrium state. Thus, $A2 = \Sigma_1$. A2 is the value when the curve levels out, which represents the maximum limiting current of the cell, marked as V_p here. The meaning of x0 in the equation is the anode surface area at which the increasing rate of the limiting voltage reaches maximum. This anode surface area is defined as A_m .

Furthermore, term dx is the slope which describes the steepness of the curve, with a larger value denoting a shallow curve, and here we note it as σ . Define σ as the product of the electrode distance, l , and the diameter of the anode, D. Because when the electrode distance is

fixed, the anode surface area is changed with changing the depth of the anode, and this result in the increase of the amounts of melt between the anode and cathode for the current to run through and thus the increase of limiting voltage. The equivalent surface area for this path equals the product of the diameter of the anode and the depth. Thus, the physical meaning of the defined σ is the rate of equivalent volume change. In this group of experiment, it gives

$$\sigma = 3.629 \text{ cm}^2$$

which equals the coefficient in the fitted curve (3.58693 ± 1.10972).

As discussed before, in Figure 6-15, the linearity between the limiting current and the anode surface area is subject to a noticeable change at the level of half cathode depth. At the half cathode depth, the surface area reads 9.72 cm^2 , which matches with the value of x_0 (9.88307 ± 1.53231) in the fitted equation. Interesting, the equation shows the slope of the curve at x_0 culminates, which means the transition at the half cathode depth is captured at this position. Note A_h as x_0 for this equation. Then the physical meaning of A_h is the anode surface area of anode half the cathode depth.

Therefore, a mathematical model of limiting voltage against anode surface area is developed with a Boltzmann fit by rewriting Equation (6.8) as

$$\Delta V_{max} = V_p + \frac{(\Sigma_1 - V_p)}{1 + e^{\frac{A - A_h}{\sigma}}} \quad (6.9)$$

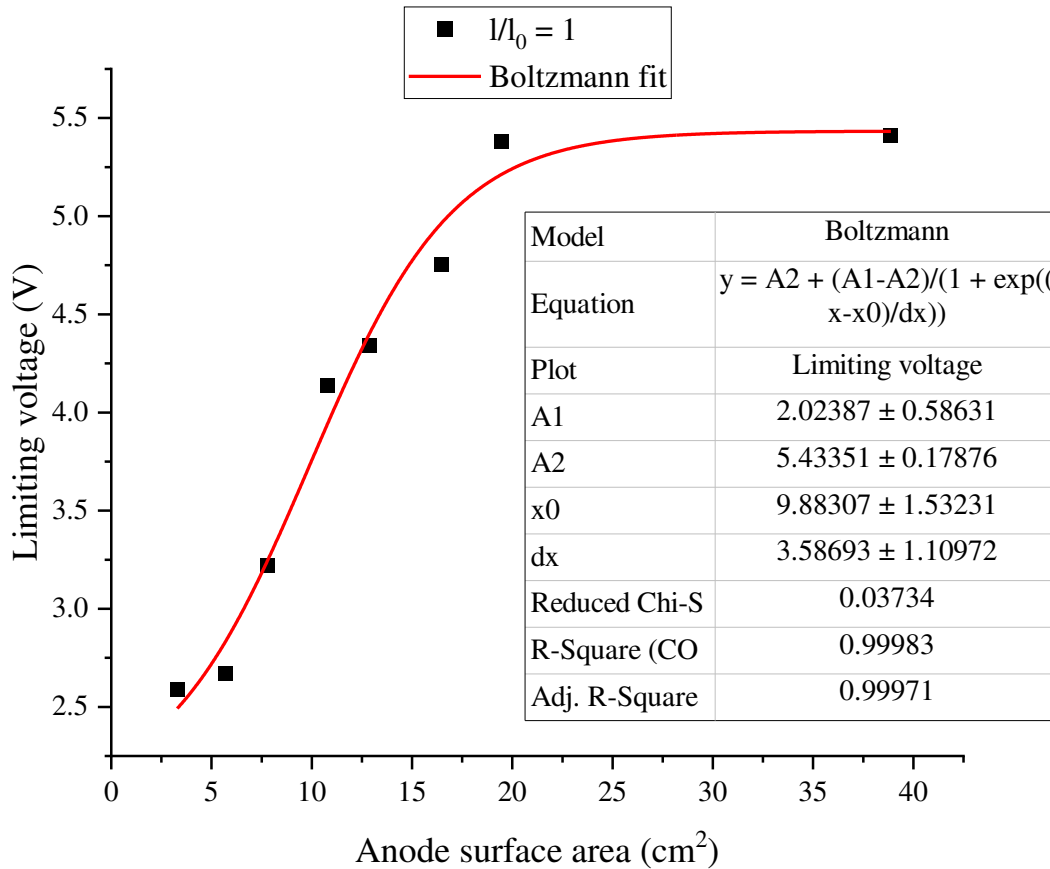


Figure 6-17 Limiting voltage changes with increasing anode surface area (Electrode distance: $l = l_0$ (3.81 cm))

More discussion is needed for Figure 6-17 as different situations are involved with increasing anode surface area. From Experiments 9 to 15 ($3.29 \text{ cm}^2 < A < 19.44 \text{ cm}^2$), one anode was used, and the anode surface area increases with the submerged depth of the anode until the anode depth levels with that of the cathode at 6.5 cm. Significant electric field structure change at half cathode depth and the effect on the limiting voltage can be expressed in Equation (6.9).

In Figure 6-17, the limiting voltage levels out at 19.44 cm^2 , from which anodes were added symmetrically into the cell. The same limiting voltages from 19.44 cm^2 (one anode at cathode depth) to 38.88 cm^2 (two anodes at cathode depth) were observed and this is because

that the symmetrical anodes are equivalent to paralleled electrical elements. In the future discussion, one should be aware of this difference between the case with anode surface area less than 19.44 cm and that with larger anode surface area and that Equation (6.9) is only valid when the anode surface area changes with changing its depth within the cathode depth range. When the anode levels with the cathode at the bottom, the limiting voltage is V_p .

Consider the depth ratio of anode to cathode, γ , for the discussion of changing the anode depth within the cathode depth range. Then, Equation (6.9) is rewritten as

$$\Delta V_{max} = V_p + \frac{(\Sigma_1 - V_p)}{1 + e^{\frac{\pi(\gamma-0.5)h_c}{l}}} \quad (6.10)$$

where h_c is the depth of the fixed cathode, and l is the electrode distance.

At $\gamma = 1$, it gives

$$\Delta V_{max} = V_p$$

Based on Equation (6.10), the limiting current, i_{max} , can be determined by the following equation for $0 < \gamma < 1$.

$$i_{max} = i_{max}^0 \frac{\gamma - 1}{\ln \gamma} \left[1 - \frac{1}{1 + e^{\frac{\pi(\gamma-0.5)h_c}{l}}} \right] \quad (6.11)$$

where i_{max}^0 is the limiting current when the anode levels with the cathode in depth.

The limiting current is calculated and compared with the experimental results in Figure 6-18. It indicates that high congruence is achieved between the calculated results and the experimental results.

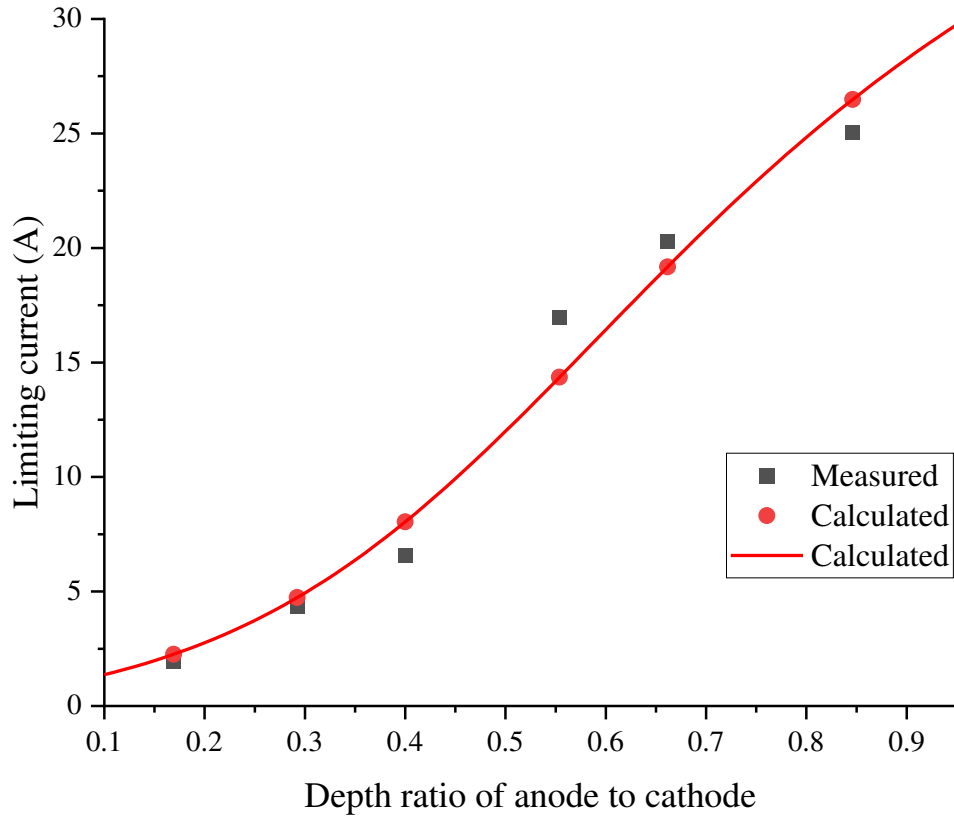


Figure 6-18 Comparison on the limiting current with varying depth ratio of anode to cathode between the experimental results and the calculated results according to Equation (6.11)

Furthermore, the limiting current density can be calculated using the following equation based on the limiting current:

$$J_{max} = J_{max}^0 \frac{(\gamma - 1)}{\gamma \ln \gamma} \left[1 - \frac{1}{1 + e^{\frac{\pi(\gamma - 0.5)h_c}{l}}} \right] \quad (6.12)$$

where J_{max}^0 is the limiting current density when the anode levels with the cathode in depth.

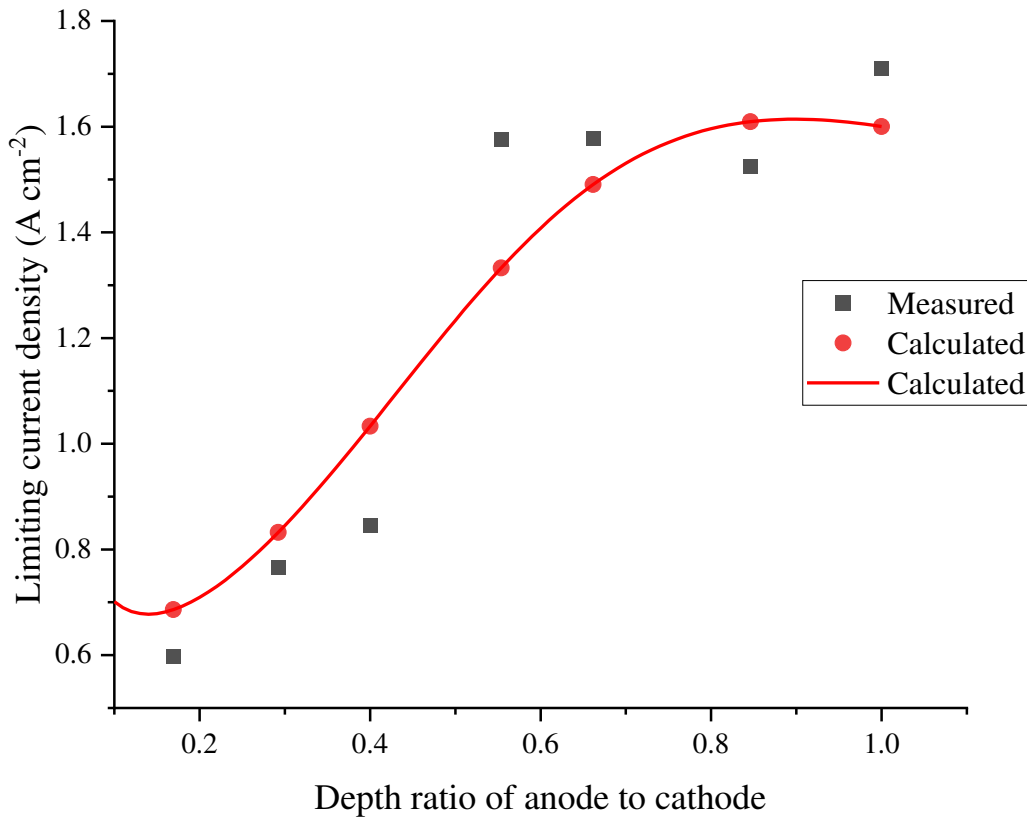


Figure 6-19 Comparison on the limiting current density with varying depth ratio of anode to cathode between the experimental results and the calculated results according to Equation (6.12)

Figure 6-19 compares the limiting current density between the experimental results and the calculated results according to (6.12). It is shown that good congruence is achieved between the experimental results and the calculated data. When the depth ratio of anode to cathode is small, it appears the limiting current density is decreased. An explanation to this is that because of lack of uniformity of the charge density at the anode surface, the current density at the surface correspondingly varies with the depth of the anode surface. The lower the anode surface, the higher the current density is. With the increase of current in the cell circuit, the current density

increases. When the current density at the bottom surface of the anode reaches its maximum level, the bottom surface is covered with the gas product and partial anode effect is achieved. With the current continuing to increase, the covered surface spreads from the bottom to the submerged top rapidly until all the surface of the submerged part of the anode is blocked by the gas products as complete anode effect occurs. The limiting current density is the average current density at the limiting current. The smaller the depth ratio of anode to cathode, the more significant the charge density gradient from the submerged top of the anode to cathode is. Therefore, the limiting current density at low γ levels gives a lower limiting current density.

As discussed in CHAPTER 5, the electrolysis should be carried out under conditions along Line bc (for this group of experiments, it is Line bm as the anode effect occurring at Point m terminates the process). To simplify the discussion here, it is assumed that the cell is thermally self-sustaining under any conditions, which means the heat loss of the cell equals the thermal energy released from the cell due to electrical resistance. The energy efficiency of the cell for conditions along Line bm can be determined by the following equation:

$$\mu(\%) = \frac{\Sigma_1}{\Delta V_{ac}} \times 100 \quad (6.13)$$

In Equation (6.13), along Line bm, the energy efficiency of the cell decreases with the increase of current. In practice, maximum throughput is desirable for neodymium production. When at limiting current, i_{max} , it gives the theoretical limiting current energy efficiency for each cell

$$\mu_{max}(\%) = \frac{\Sigma_1}{\Delta V_{max}} \times 100 \quad (6.14)$$

The values of the thermal energy generated at the limiting current, ΔH , and those of the theoretical limiting current energy efficiency, μ_{max} , are calculated and listed in Table 6-5. ΔH increases with the anode surface area because the limiting current increases.

According to Equation (6.10) and Equation (6.13), it is shown that the theoretical limiting current energy efficiency can be determined by the following equation:

$$\mu_{max}(\%) = \mu_{max}^0 + \frac{100 - \mu_{max}^0}{1 + \frac{100}{\mu_{max}^0} e^{\frac{(\gamma-0.5) \times \pi \times h_c}{l}}} \quad (6.15)$$

where μ_{max}^0 is the theoretical limiting current energy efficiency when the anode levels with the cathode.

Figure 6-20 compares the theoretical limiting current energy efficiency between the experimental results and the calculated results according to (6.15). Again, high congruence is shown to be achieved.

Figure 6-20 catches our attention and it demonstrates that the level-out position of anode gives the lowest theoretical limiting current energy efficiency and by raising the anode one can increase the theoretical limiting current energy efficiency. For the discussion of energy efficiency, the theoretical limiting current energy efficiency at half cathode depth is defined as theoretical half depth energy efficiency, and noted as μ_h . The reason this point is picked is that this represents the inflection point of the Boltzmann plot and it corresponds to the maximum change rate of the theoretical limiting current energy efficiency over anode surface area, and when $\gamma < 0.5$, the limiting current density decreases significantly.

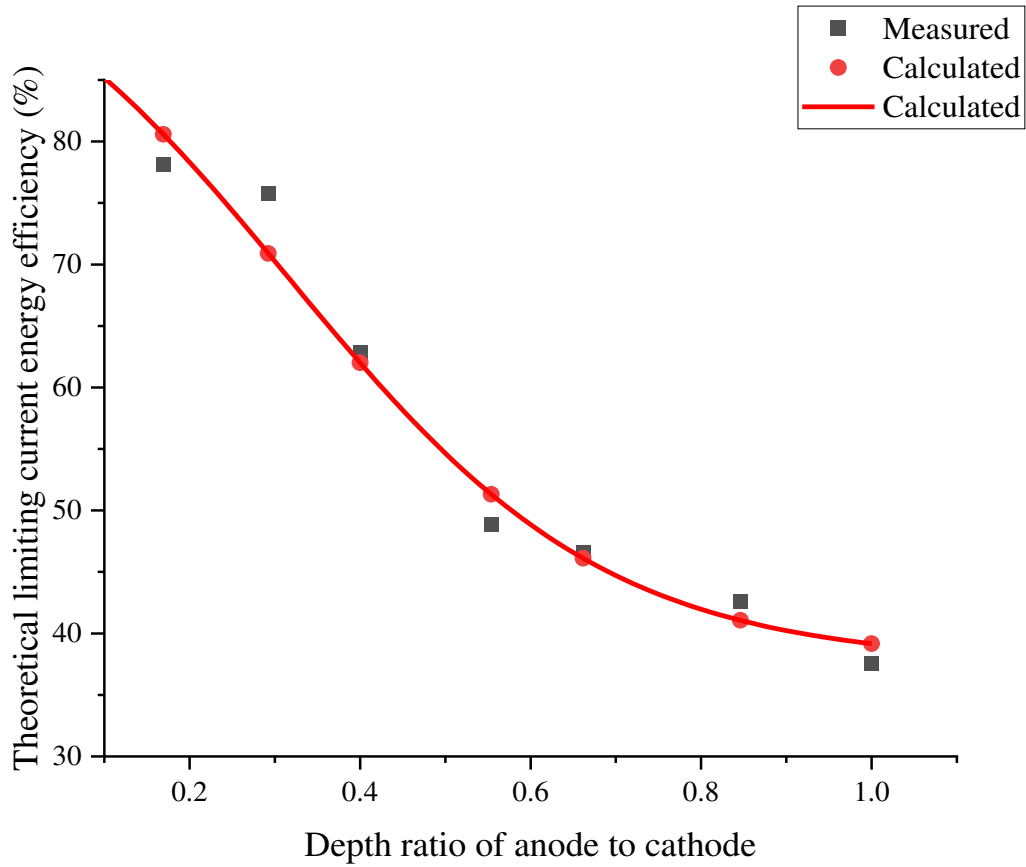


Figure 6-20 Comparison on the theoretical limiting current energy efficiency with varying depth ratio of anode to cathode between the experimental results and the calculated results according to Equation (6.15) (6.11)

Therefore, the following equation gives the mathematical expression of μ_h at $\gamma = 0.5$:

$$\mu_h(\%) = \frac{100 + \mu_{max}^0}{2} \quad (6.16)$$

In this group of experiments, it gives $\mu_h=68.7\%$ and this means that by raising the anode from the cathode level to the half depth of cathode level, the theoretical limiting current energy efficiency increases from 37.06% to 68.7% by 83.91%. The disadvantage of this change is that it decreases the anode surface area and thus the limiting current, which results in the reduction on

throughput. However, this issue can be addressed by adding more anodes into the cell symmetrically.

Besides the theoretical significance, this finding is of technical importance. It suggests that positioning the anode above the level of cathode provides significant potential to increase energy efficiency. Considering it possibly results in insufficient use of the salt in a conventional cell configuration, a cone design of electrolysis or other cell types with radially decreasing depth to the bottom is recommended based on the result of this study.

6.4.3 Impact of electrode distance on the electrolysis process

Electrode distance is a very important parameter for the electrolysis process. The configuration of the cell in the experiments limits its capability to study the cases for varying electrode distance. With the results and discussion presented in the last section, we can make the following assumptions the electrolysis process with varying electrode distance:

- (1) The limiting current is a function of the anode depth in the cell. Within the depth range from zero to the cathode depth, anode effect occurs at the same limiting current as observed in the experiments at electrode distance, l_0 , under the same depth.
- (2) The non-resistance potential Σ_1 remains the same as at electrode distance, l_0 .
- (3) There exists a linear relationship between the cell voltage and current from equilibrium current to the limiting current.
- (4) The slope of Line bm is positively proportionate to electrode distance.

Therefore, for a different electrode distance, l ($l > D$), it gives

$$\Delta V_{max} = \Sigma_1 + Si \quad (6.17)$$

If we note the values from the results at electrode distance, l_0 , with a subscript of 0. We

have

$$\Delta V_{max} = \frac{l}{l_0} \times (\Delta V_{max(0)} - \Sigma_1) + \Sigma_1 \quad (6.18)$$

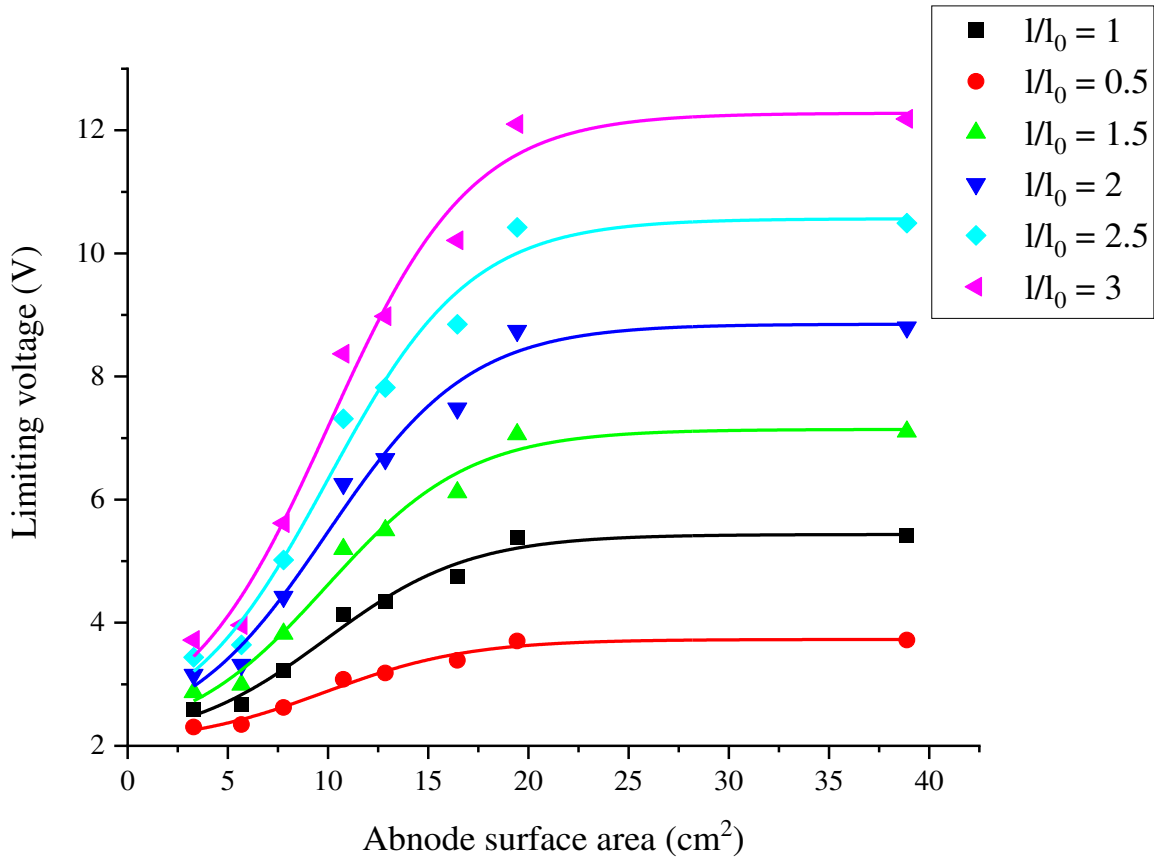


Figure 6-21 Limiting voltage changes with increasing anode surface area considering varying electrode distance

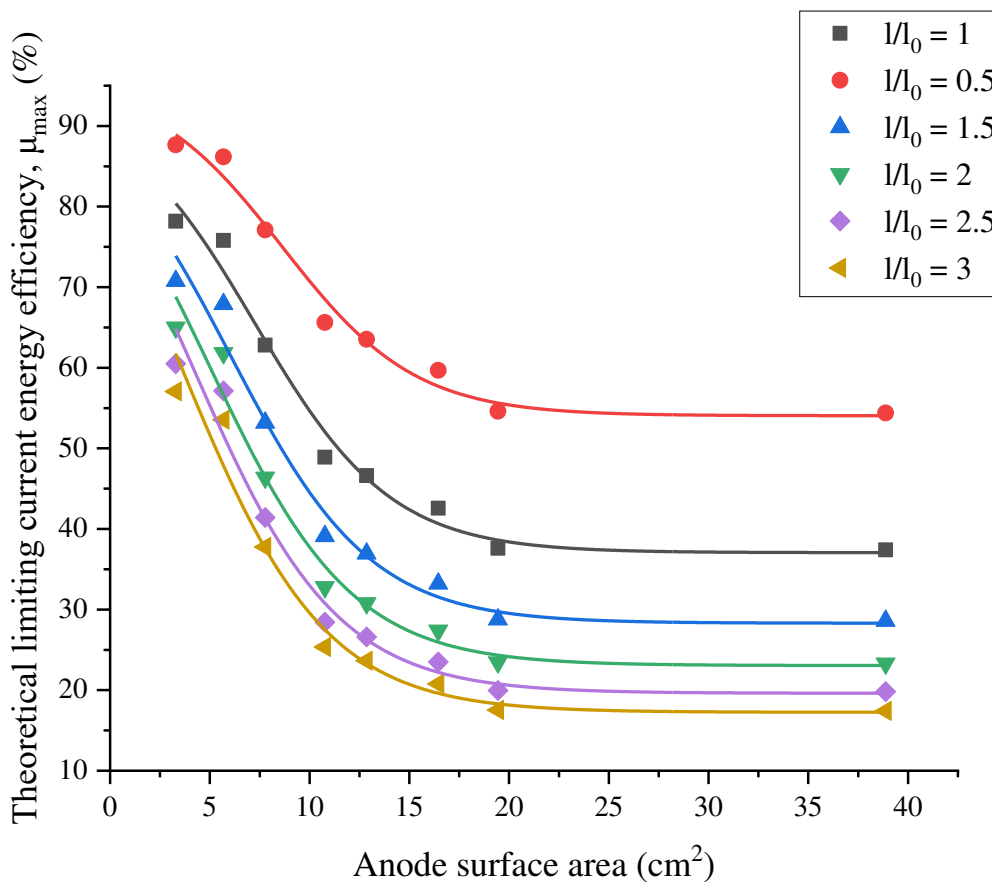


Figure 6-22 Theoretical limiting current energy efficiency changes with increasing anode surface area with varying electrode distance

The results are presented in Figure 6-21 and fitted in the same equation as Equation (6.8). It is noticeable high correlation is achieved in the Boltzmann fit for the case of each electrode distance (statistics analysis results shown in Table 6-6 Coefficients for Boltzmann fit analysis as in Figure 6-21). The results indicate that with increasing the electrode distance the limiting voltage increases.

Similarly, the theoretical limiting current energy efficiency is determined for each case of electrode distance and presented in Figure 6-22. The results for each case are fitted in a Boltzmann equation as Equation (6.9). The corresponding coefficients and statistics analysis are

presented in Table 6-7. It shows that with increasing electrode distance, the theoretical limiting current energy efficiency decreases at each anode surface area level. It is noticed that by reducing the electrode distance from l_0 to $0.5 l_0$, the theoretical level-out energy efficiency, μ_{max}^0 , increases from 37.06% to 56.05% by 51.24%, which is significant but not as much as the increased extend with cutting the anode depth by half, in which case as we discussed in the previous section the value increases by 83.92%.

Figure 6-23 depicts the change of theoretical level-out energy efficiency, μ_{max}^0 , and theoretical half-depth energy efficiency, μ_h , against the relative electrode distance, $\frac{l}{l_0}$. It shows that both μ_{max}^0 and μ_h decreases with increasing electrode distance. The decreasing rate of the former is higher than that of the latter. This suggests that by shortening the electrode distance one can effectively increase the energy efficiency and this effect is more significant at full cathode depth than at the half depth. Another obvious observation is that the by raising the anode to the level of half the cathode depth the theoretical energy efficiency increases dramatically. Therefore, a conclusion can be made from this discussion that one can increase the energy efficiency by pulling the anode up offset to the cathode depth level and reduce electrode distance.

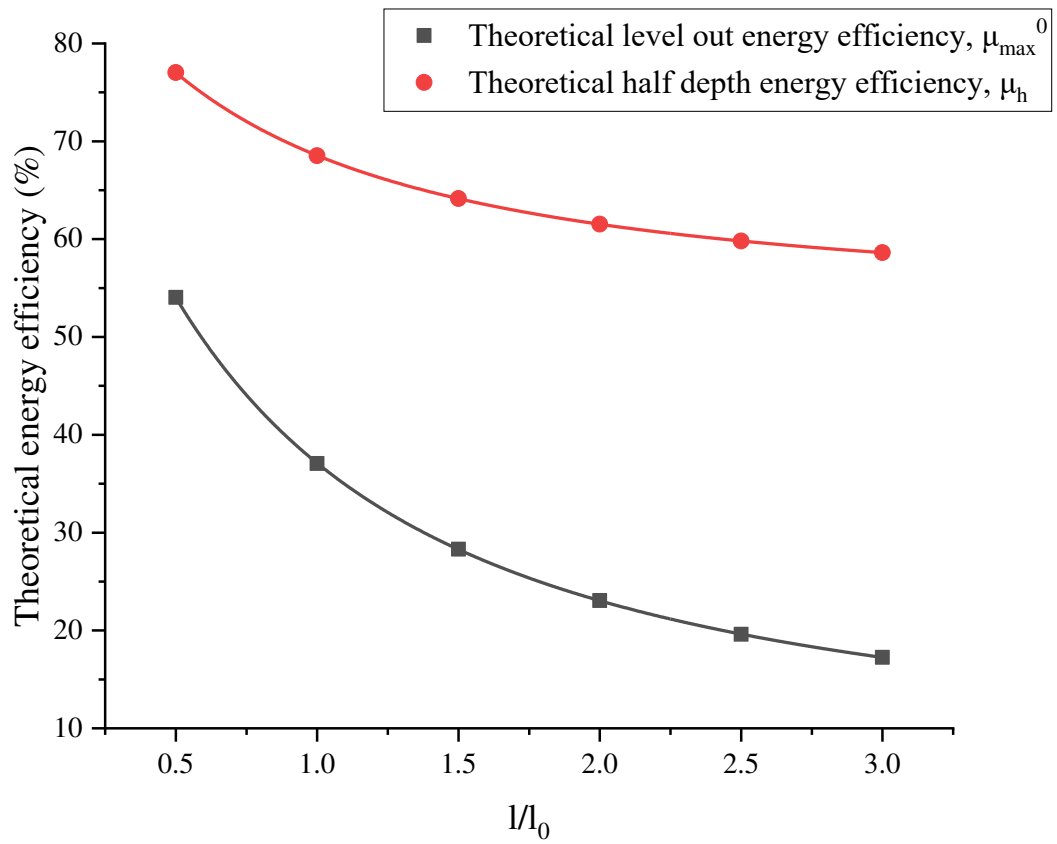


Figure 6-23 Theoretical level-out energy efficiency and theoretical half depth energy efficiency as a function of electrode distance

Table 6-6 Coefficients for Boltzmann fit analysis as in Figure 6-21

No.	$\frac{l}{l_0}$	A1		A2		x0		dx		Statistic
		Value	Standard Error	Value	Standard Error	Value	Standard Error	Value	Standard Error	Adj. R-Square
1	1	2.02387	0.58631	5.43351	0.17876	9.88307	1.53231	3.58693	1.10972	0.99971
2	0.5	2.02211	0.29426	3.7282	0.09012	9.86726	1.5299	3.58967	1.1115	0.99993
3	1.5	2.03226	0.87423	7.14067	0.26467	9.90821	1.53607	3.5825	1.10692	0.99937
4	2	2.04997	1.15632	8.85029	0.34686	9.94145	1.5406	3.57622	1.10311	0.99894
5	2.5	2.07921	1.43104	10.56272	0.42471	9.98138	1.54513	3.56789	1.09835	0.99846
6	3	2.12194	1.69686	12.27798	0.49782	10.0268	1.54874	3.55711	1.09264	0.99794

Table 6-7 Coefficients for Boltzmann fit analysis as in Figure 6-22

No.	$\frac{l}{l_0}$	A1		A2		x0		dx		Statistic
		Value	Standard Error	Value	Standard Error	Value	Standard Error	Value	Standard Error	Adj. R-Square
1	1	93.91308	22.61462	37.06143	1.0468	7.2663 3	3.354	3.41031	1.15815	0.99683
2	0.5	95.92058	10.57704	54.05072	1.03576	8.6360 6	2.34863	3.33109	1.08253	0.99596
3	1.5	94.72282	38.4369	28.30836	1.01252	6.0389 1	4.4811	3.50945	1.23636	0.99717
4	2	97.22443	57.9291	23.05259	0.97356	4.9970 8	5.64053	3.57743	1.30074	0.99733
5	2.5	100.41365	79.81515	19.6152	0.93739	4.1578	6.74129	3.61175	1.34851	0.99741
6	3	103.6445	102.30394	17.25	0.90605	3.5093 3	7.71777	3.62076	1.38145	0.99747

6.4.4 Electrolysis product characterization

Experiment 17 was carried out under the same conditions with Experiment 16 except for the neodymium oxide added during the electrolysis process in this experiment with size ranging from 1 mm to 2mm. Figure 6-24 records the cell voltage information against current for the test. It is shown that the pattern matches with that of Experiment 16 as anticipated. Consistency of the process is proved and the choice of using larger particles is to eliminate the interference from argon injected in the cell which causes inconsistency as shown in the previous study.

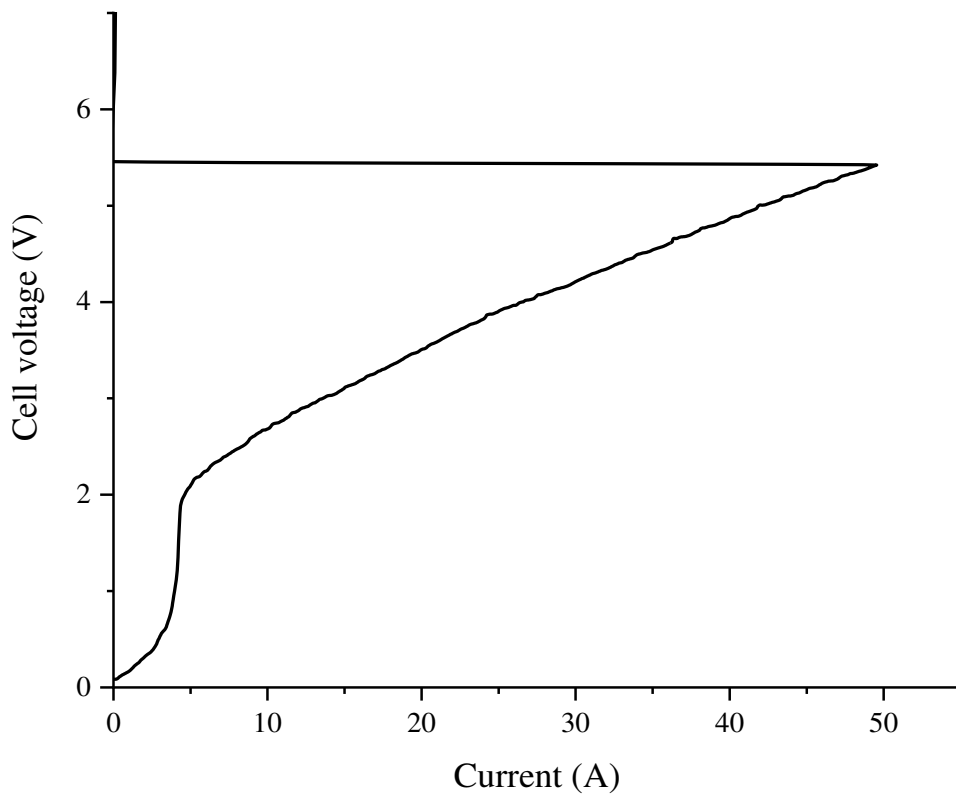


Figure 6-24 Cell voltage changes with increasing current: Exp. 17, oxide particle size - 2mm+1mm

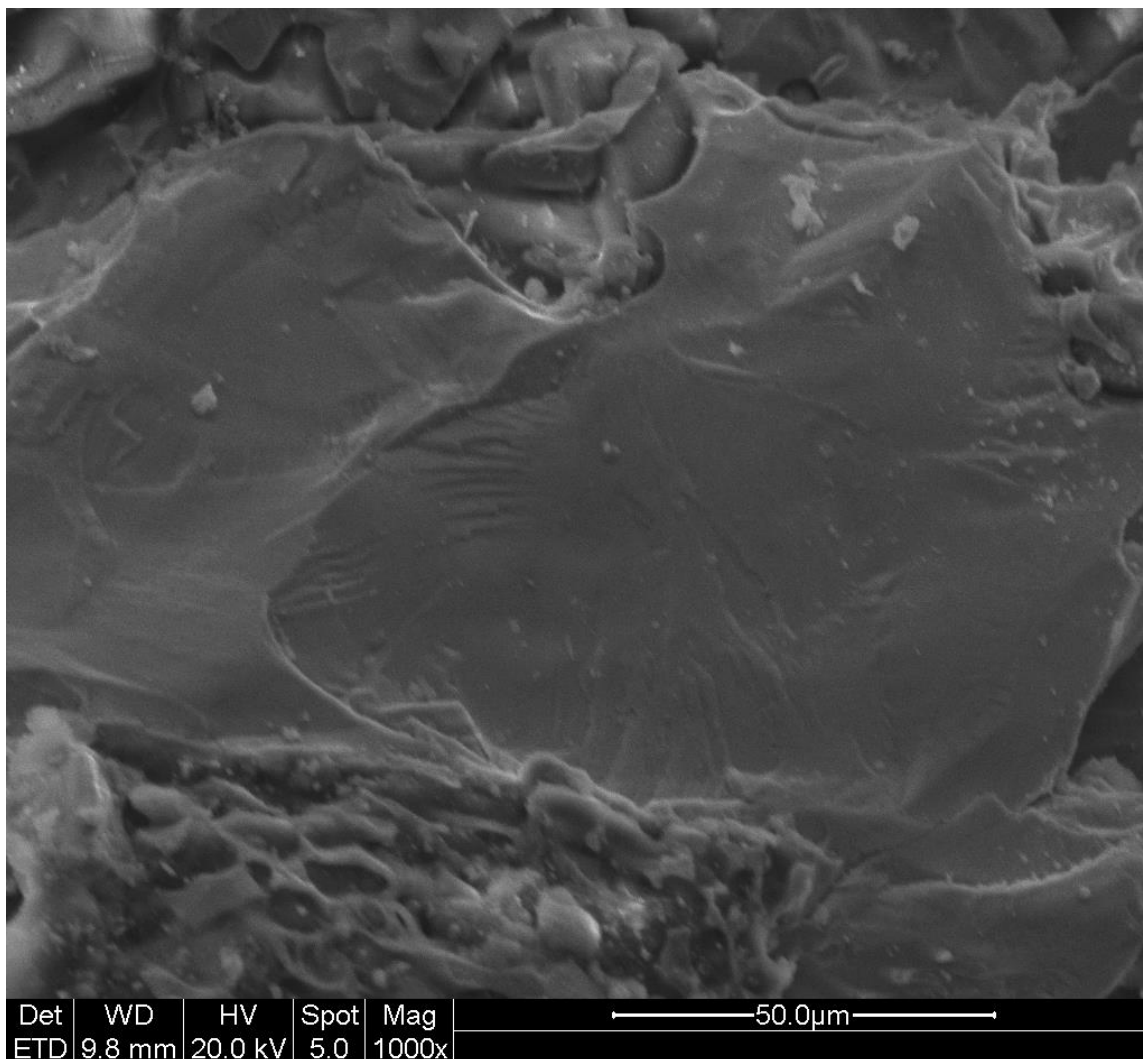


Figure 6-25 SEM image of the metal product from the electrolysis process: 1000X

An experiment with fixed cell voltage (5.2 V) was performed with continuously addition of Nd_2O_3 according to the stoichiometric amount with the assumption of 100% current efficiency. The current throughout the test read about 45 A. The offgas was captured through a syringe for the gas chromatograph test (SRI Instrument model 8610 GC, carrier gas: carrier gas). The GC result indicates three peaks at 1.190 s, 1.310 s, and 4.803 s with intensity counts of 274, 248, and 2.5, respectively. By comparing to the patterns and known components, it is concluded the peaks prove the presence of argon (1.190 s), carbon monoxide (1.310 s) and carbon dioxide

(4.803 s, 0.3717%). No presence of CF_4 or C_2F_6 is shown with the test, which is in agreement with the conclusion that no occurrence of fluoride decomposition under conditions along Line bc.

The metal produced through the electrolysis test was collected for ESEM-EDX. Figure 6-25 is the image of the metal under SEM with magnification of 1000. Figure 6-26 shows the EDX results for the sample and it indicates 100% Nd presence under spot scanning. High purity of neodymium production from the electrolysis is confirmed.

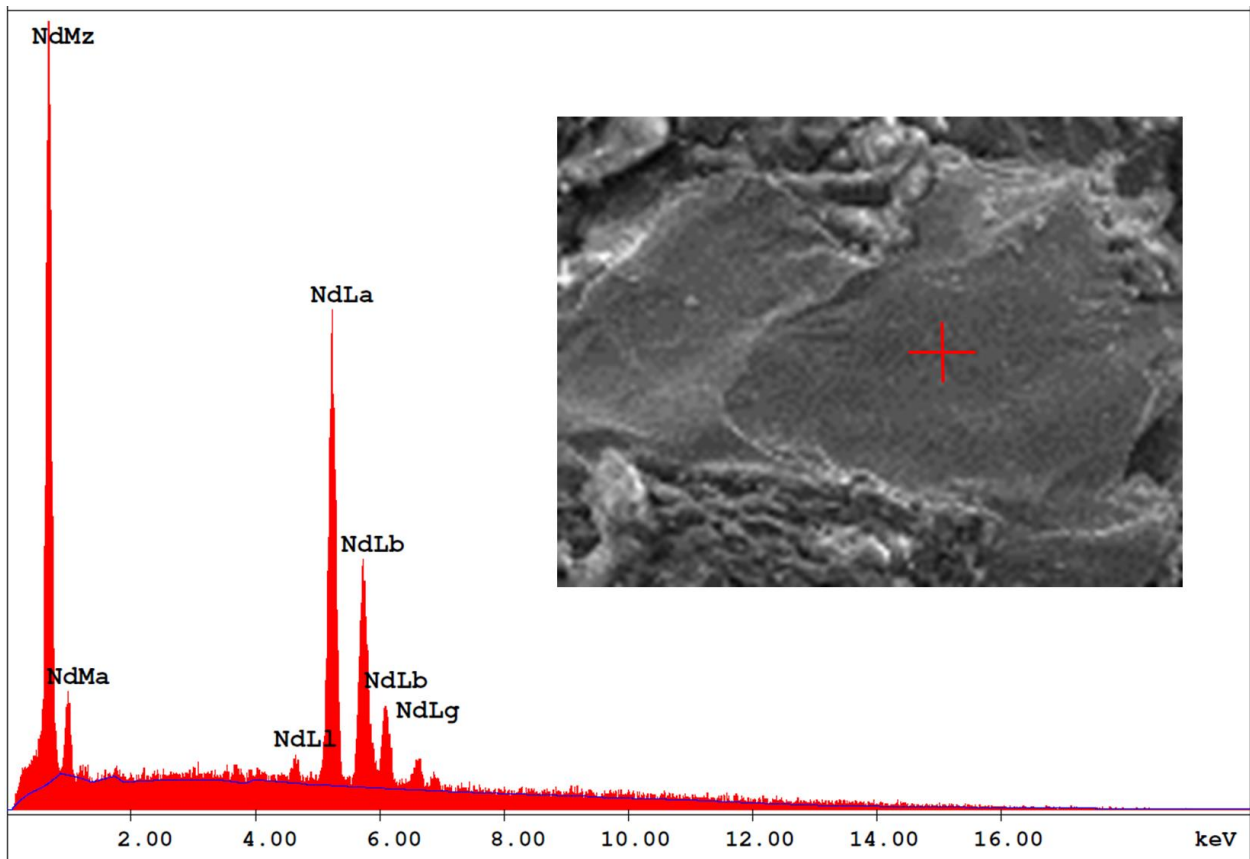


Figure 6-26 EDX analysis result of metal product from the electrolysis process

6.5 Conclusion

In this chapter, an electrolysis cell was built to carry out electrolysis investigations on reducing neodymium oxide in the $\text{NdF}_3\text{-LiF}$ molten electrolyte. Through a series of electrolysis experiments, the mathematical model developed in the previous chapter has been validated and utilized to analyze the experiment results. High purity neodymium metal was electrowon through electrolyzing neodymium oxide in the $\text{NdF}_3\text{-LiF}$ (85 wt% NdF_3) melt at 1050 °C. The results show that the limiting current increases with anode surface area and the linearity of the relationship between two changes with the position of the anode in the melt. It is found that the reciprocal of the geometry term, G , for the cell linearly increases with the anode surface area. A mathematical model has been developed to illustrate the relationship between the limiting voltage and the anode surface area by a Boltzmann equation. The correlation coefficient of the equation is as high as 0.99971. The corresponding parameters are determined based on the cell configuration and the electrolysis conditions. Furthermore, high throughput with high energy efficiency can be achieved by reducing the electrode distance and reduce the depth ratio of anode to cathode.

CHAPTER 7

CONCLUSIONS

This chapter forms the final element of the thesis. It consists of a synthesis of a set of conclusions concerning the electrochemical properties of molten fluoride electrolytes in support of the technological development of neodymium reduction, as well as an in-depth discussion of guidelines to increase energy efficiency and limit PFCs emissions with elevated production capacity for the electrolysis process. At the end of the chapter, recommendations for future work in the field are provided.

7.1 Thesis conclusions

The thesis focuses on two directions to perform fundamental research for neodymium oxide reduction in molten fluoride salts. One is to investigate the physical and electrochemical properties of the fluoride melt. This includes the establishment of a ternary liquidus temperature diagram of the $\text{NdF}_3\text{-PrF}_3\text{-LiF}$ system, the determination of the solubility of neodymium oxide in the fluoride melt, and the measurement of the electrical conductivity of $\text{NdF}_3\text{-LiF}$ salts at different temperatures and compositions. The other direction is to develop an experimentally-validated theoretical model to elucidate the relationship between the cell voltage and current in the electrolysis cell and seek solutions from the scientific standpoint to the two major problems associated with the technology of the oxide-fluoride electrolysis of rare earth metals: low energy efficiency and excessive emissions.

7.1.1 Conclusions regarding the property study

In this research, liquidus temperatures of mixed NdF_3 , PrF_3 and LiF were determined with the technique of differential scanning calorimetry (DSC) and inductively coupled plasma mass spectroscopy (ICP-MS) was used to characterize the composition of the mixture. A ternary

diagram of liquidus temperatures with respect to the $\text{NdF}_3\text{-PrF}_3\text{-LiF}$ system has been constructed. This informs the choice of the experimental temperature range when investigating the properties of the $\text{NdF}_3\text{-PrF}_3\text{-LiF}$ molten salt with a specific composition. Furthermore, the same technique was adopted to estimate the solubility of Nd_2O_3 in the fluoride melt considering at the liquidus state of a fluoride salt containing a small amount of Nd_2O_3 the fluoride salt is considered saturated with the oxide. Compared with other techniques to evaluate the oxide solubility in molten salts, this novel technique requires only small sample amounts and is easy to operate. The results indicate that the presence of NdF_3 in the fluoride salt increases the solubility of Nd_2O_3 even though the solubility of Nd_2O_3 is not high. In this research, it shows that the solubility of Nd_2O_3 in the $\text{NdF}_3\text{-LiF}$ (NdF_3 82.6 wt%) is 3.39 wt% of the total fluoride mass at 1053 °C.

As for the determination of the electrical conductivity of $\text{NdF}_3\text{-LiF}$, a conductance cell with vertically movable electrodes was designed and constructed and reliable electrical conductivity data was collected. The results show that the electrical conductivity of the fluoride melts increases with increasing temperature and LiF content. The electrical conductivities of the molten salt system between 70 and 85 wt% NdF_3 within the range of temperature from 950 °C to 1050 °C range from $4.38 \text{ ohm}^{-1} \text{ cm}^{-1}$ to $6.08 \text{ ohm}^{-1} \text{ cm}^{-1}$. A series of mathematical equations is proposed to estimate the electrical conductivity with high correlation coefficients. The discussion of molar electrical conductivity finds that a linear relationship exists between the natural logarithm of the molar electrical conductivity and that of the charge density of the cations in the melt. Within the investigated conditions this relationship is independent of temperature and determined by the content of NdF_3 . The slope and the intercept for the linear regression changes linearly with the molar mass of the melt. An explanation for this is that the $\text{NdF}_3\text{-LiF}$ salt within the investigated compositions exhibits similar molten salt structure and with increasing NdF_3

content, larger Nd-centered assemblages in the melt. This decreases the mobility of the ions and thus affect the response for the molar electrical conductivity to the change of charge density. Interestingly, the same effect is seen with the analysis of the data for the alkali chloride with the order of KCl, NaCl, RbCl and CsCl as the K-Na-Rb-Cs series represents increasing charge carriers in size. This finding supports the explanation above. An empirical equation is proposed to estimate electrical conductivity for a specific salt.

7.1.2 **Conclusions regarding the electrolysis process**

A mathematical model concerning the change of cell voltage against current in the electrolysis process has been established with the study of thermodynamics and kinetics in the process of electrowinning neodymium in the $\text{NdF}_3\text{-LiF}$ electrolyte. The mathematical equation proposed in this research indicates the relationship between the cell voltage and the current is determined by the following parameters: temperature, chemical potentials of the reaction, activity of the oxide, solubility of the oxide, diffusivity of oxygen-containing ions and neodymium ions, maximum dissolution rate of the oxide, maximum mass transfer rate of the oxide, the geometry of the electrolysis cell and the electrical conductivity of the electrolyte.

Combining the discussions in CHAPTER 5 and CHAPTER 6, a figure is obtained as Figure 7-1 which constitutes three diagrams to illustrate the electrolysis process and provide insights for process optimization. Throughout the discussion it is assumed electrolysis occurs with 100% current efficiency and the resistances caused by the cell circuit connections and the gas bubbles (except for onset of the anode effect). In the discussion of energy efficiency, it is assumed that the cell is thermally self-sustaining, which means the thermal energy released due to the resistance of the melt equals the heat loss throughout the electrolysis process.

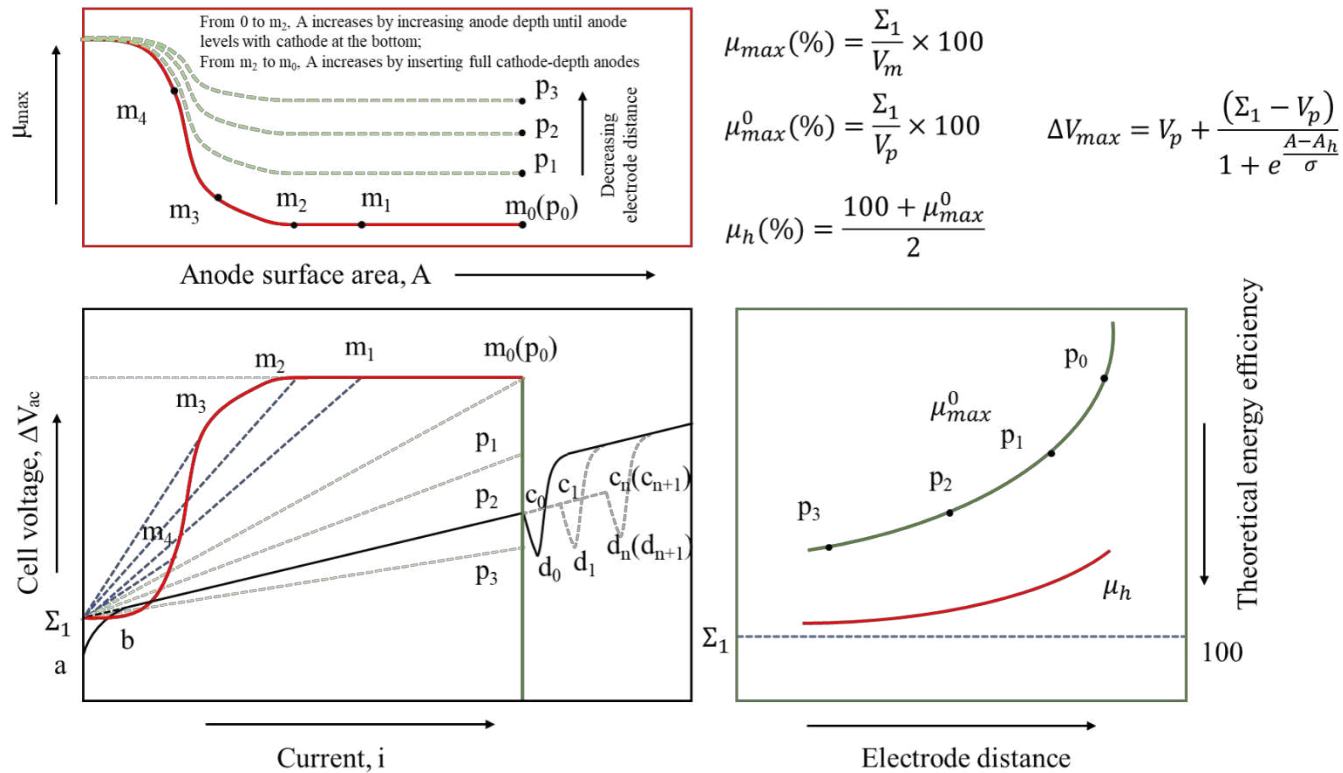


Figure 7-1 Compilation of diagrams for the electrolysis process in molten fluoride based on the discussion in this thesis with assumption of thermally self-sustaining cell. **Bottom left:** black full-line (with grey dash-lines) - line *abcd* represents the typical response of cell voltage to the change of current (from c_0 to c_{n+1} , either increasing the maximum dissolution rate of oxide or increasing the maximum mass transfer rate of oxide in the melt); red full-line – the limiting cell voltage as a function of anode surface area, A , (from m_4 to m_0 , fitted in a Boltzmann equation); navy blue dash-lines – the cell voltage change against current with changing anode surface area and fixed electrode distance (from $\Sigma_1 m_0$ to $\Sigma_1 m_4$, anode surface area decreases linearly related to limiting current); green dash-lines – the cell voltage change against current with changing electrode distance and fixed anode surface area (from $\Sigma_1 p_0$ to $\Sigma_1 p_3$, the electrode distance decreases). **Top left:** the change of the theoretical limiting current energy efficiency, μ_{max} , against the anode surface area, A , regarding various difference electrode distance, l . **Bottom right:** the optimal theoretical energy efficiency, μ_{max}^0 , changes with increasing electrode distance.

The black full-line in the bottom-left diagram illustrates the typical response of the cell voltage to the increase of current and, associated with the grey dash-lines, explains the methods to avoid the decomposition of the fluorides and hence reduce PFCs emissions. As discussed in CHAPTER 5, Point c_0 represents the onset of NdF_3 decomposition, for which the corresponding current is defined as critical current, i_c . If the electrolysis is operated at a current exceeding i_c , PFCs are generated from the decomposition of NdF_3 . Hence the operating current should remain lower than critical current. The optimal condition is to adjust the limiting current to equal the critical current and maximum throughput can be achieved at limiting current without PFCs emissions. To increase critical current, one should either increase the maximum dissolution rate of oxide or increase the maximum mass transfer rate of the dissolved oxide in the melt, or both, if necessary. By doing so, Point c_0 shifts along Line bc.

The red full-line in the bottom-left diagram provides insights for the relationship between the anode surface area within the cathode depth range and the limiting voltage. A proved equation is provided to express this relationship:

$$\Delta V_{max} = V_p + \frac{(\Sigma_1 - V_p)}{1 + e^{\frac{A-A_h}{\sigma}}}$$

where ΔV_{max} is the limiting voltage, V_p is the limiting voltage when the anode levels with the cathode at the bottom, Σ_1 is the non-resistance potential, A is the anode surface area ranging from zero to the corresponding surface area for anode at the cathode depth, A_h is the anode surface area with anode levelling at half cathode depth, and σ is the product of electrode distance, l , and diameter of the anode, D . This equation is experimentally proved in this work.

The lines in the top-left diagram and the line in the bottom-right diagram give a guide for increasing energy efficiency in the electrolysis process. The diagram shows that by reducing the

depth ratio of anode to cathode in the melt and the electrode distance one can effectively increase energy efficiency. The potential of the former is proved to be more significant.

In summary, a clear elucidation of the process optimization for the molten salt electrolysis has been achieved. It is desirable to maximize the production throughput with high energy efficiency and minimal or no PFCs emissions. To avoid the generation of PFCs, the limiting current should be adjusted to be smaller than the critical current at which the decomposition of neodymium fluoride occurs. The critical current can be elevated by increasing the maximum dissolution rate of oxide and the maximum mass transfer rate of the dissolved oxide in the melt. To maximize energy efficiency with high throughput, the electrode distance should be reduced and the ratio of the depth of anode to that of cathode should be reduced.

7.2 Contributions to the knowledgebase

- Systematic study on the electrical conductivity of $\text{NdF}_3\text{-LiF}$ molten salts.
- Establishment of an empirical relationship between electrical conductivity between electrical conductivity and density.
- Development of an experimentally validated mathematical model describing the voltage-current relationship in the molten salt process.
- Explanation in a fundamental level for the fluoride decomposition in the electrolysis process.
- Clarification on the confusion between anode effect and PFCs emissions in the electrolysis process.
- A novel experimental method developed to study the electrolysis process.
- The effect of anode surface area and electrode distance on the molten salt electrolysis of neodymium.

- Terminology introduction of the theoretical limiting current energy efficiency, μ_{max} , the theoretical level-out energy efficiency, μ_{max}^0 , and theoretical half-depth energy efficiency, μ_h , to the energy efficiency study in the electrolysis system.
- Establishment of a mathematically and experimentally proved Boltzmann equation to illustrate the relationship between limiting voltage and anode surface area.
- Illustration of optimizing the electrolysis for high throughput, controlled PFCs emissions, and high energy efficiency at a fundamental level.

7.3 Recommendations for future work

While this work has taken a fundamentals-based approach to understanding the electrolysis of rare earth metals in the molten fluorides, there are a number of opportunities for future research. These include:

- Investigation of the impact of the particle size of the added oxide during the electrolysis process on the values of the critical current.
- Determination of the activity of Nd_2O_3 in the molten fluoride system.
- Exploration of inert anode options for the electrolysis to reduce CO/CO_2 emissions and simplify anode management.
- Mathematical modelling of the kinetics of the anode effect phenomena.
- Investigation of the surface chemistry among the bubble, anode surface and electrolyte and the evolution of the gas bubbles.
- Experimental and computational characterizations of the geometry term in the electrolysis cell with different cell configurations.

REFERENCES CITED

Abbasalizadeh, A., L. Teng, S. Seetharaman, J. Sietsma and Y. Yang (2016). Rare Earth Extraction from NdFeB Magnets and Rare Earth Oxides Using Aluminum Chloride/Fluoride Molten Salts. Rare Earths Industry: 357-373.

Ambrová, M., J. Jurišová, V. Danielik and J. Gabčová (2008). "On the solubility of lanthanum oxide in molten alkali fluorides." Journal of Thermal Analysis and Calorimetry **91**(2): 569-573.

ASTM (2018). Standard test method for melting and crystallization temperatures by thermal analysis.

Boettinger, W. J., U. R. Kattner, K.-W. Moon and J. H. Perepezko (2007). DTA and heat-flux DSC measurements of alloy melting and freezing. Methods for phase diagram Determination, Elsevier: 151-221.

Borges de Lima, I. (2016). Rare Earths Industry and Eco-management. Rare Earths Industry: 293-304.

Borges de Lima, I. and W. L. Filho (2016). Highlights on Rare Earths. Rare Earths Industry: 395-424.

Cassayre, L., T. A. Utigard and S. Bouvet (2002). "Visualizing gas evolution on graphite and oxygen-evolving anodes." Journal of Minerals, Metals and Materials Society **54**(5): 41-45.

Charalampides, G., K. I. Vatalis, B. Apostoplos and B. Ploutarch-Nikolas (2015). "Rare Earth Elements: Industrial Applications and Economic Dependency of Europe." Procedia Economics and Finance **24**: 126-135.

Elliott, L. (2018). "AN ENGINEERING PERSPECTIVE ON RARE EARTH ELEMENTS: A LITERARY INVESTIGATION OF MATERIALS TRANSFORMING CONSUMER TECHNOLOGY AND THE ENERGY INDUSTRY."

Fernandez, V. (2017). "Rare-earth elements market: A historical and financial perspective." Resources Policy **53**: 26-45.

Gloss, A. (1961). "Metals Handbook. Volume 1. Properties and Selection of Metals. Includes a glossary of definitions relating to metals and metalworking, 41 pp." American Society for Metals, Metals Park, Ohio, 8th ed., 1300 pp.

Goldsmith, J., P. Kruesi and N. Masarky (1973). Method for the recovery of rare earth metal alloys, Google Patents.

Goonan, T. G. (2011). Rare earth elements: End use and recyclability, US Department of the Interior, US Geological Survey Reston.

Guo, X., J. Sietsma and Y. Yang (2014). Solubility of rare earth oxides in molten fluorides. 1st European rare earth resources conference, Milos, Greece.

Guo, X., Z. Sun, J. Sietsma, B. Blanpain, M. Guo and Y. Yang (2018). "Quantitative Study on Dissolution Behavior of Nd₂O₃ in Fluoride Melts." Ind Eng Chem Res **57**(5): 1380-1388.

Guo, X., Z. Sun, J. Sietsma and Y. Yang (2016). "Semiempirical Model for the Solubility of Rare Earth Oxides in Molten Fluorides." Industrial & Engineering Chemistry Research **55**(16): 4773-4781.

Haupin, W. E. (2016). Principles of Aluminum Electrolysis. Essential Readings in Light Metals: Volume 2 Aluminum Reduction Technology. G. Bearne, M. Dupuis and G. Tarcy. Cham, Springer International Publishing: 3-11.

Henrie, T. A. (1964). "Electrowinning rare-earth and uranium metals from their oxides." JOM **16**(12): 978-981.

Hu, X., Z. Wang, B. Gao, Z. Shi, F. Liu and X. Cao (2010). "Density and ionic structure of NdF₃-LiF melts." Journal of Rare Earths **28**(4): 587-590.

International, A. (2018). Standard Test Method for Melting And Crystallization Temperatures By Thermal Analysis, West Conshohocken, PA. **E794-06(2018)**.

Janz, G., G. Janz, F. Dampier, G. Lakshminarayanan, P. Lorenz and R. Tomkins (1968). Molten salts: Volume 1. Electrical conductance, density, and viscosity data.

Jenkins, H. W. (1969). "Electrochemical measurements in molten fluorides."

Keller, R. and K. Larimer (1997). Electrolysis of neodymium oxide. Final report for the period August 19, 1991 through February 28, 1997, EMEC Consultants, Export, PA (United States).

Kim, K. B. and D. R. Sadoway (1992). "Electrical Conductivity Measurements of Molten Alkaline-Earth Fluorides." Journal of The Electrochemical Society **139**(4): 1027-1033.

Liu, Q., J. Chen, X. Wei, Z. Zhang, X. Wang, L. Xie, T. Zheng and X. Kong (2000). "Study on the density of NdF₃-LiF-Nd₂O₃ system." Rare Metals and Cemented Carbides(4): 7.

Liu., C. (1987). "3000 kA Neodymium Electrolytic Cell." Industrial Furnace(4): 59-60.

Marks, J. and C. Bayliss (2012). GHG measurement and inventory for aluminum production. Light Metals 2012, Springer: 805-808.

Marks, J., R. Roberts, V. Bakshi and E. Dolin (2000). "Perfluorocarbon Generation during Primary Aluminum Production." Light Metals: 365-372.

Morrice, E. (1964). Electrowinning cerium and lanthanum metals from their oxides, University of Nevada, Reno.

Morrice, E. and T. A. Henrie (1967). ELECTROWINNING HIGH-PURITY NEODYMIUM, PRASEODYMIUM, AND DIDYMIUM METALS FROM THEIR OXIDES. Country unknown/Code not available.

Morrice, E., E. S. Shedd and T. A. Henrie (1968). DIRECT ELECTROLYSIS OF RARE-EARTH OXIDES TO METALS AND ALLOYS IN FLUORIDE MELTS, Bureau of Mines, Reno, Nev. Reno Metallurgy Research Center.

Morrice, E. and M. Wong (1979). "Fused-salt electrowinning and electrorefining of rare-earth and yttrium metals." Min. Sci. Eng. **11**(3): 125-136.

Pang Siming, Y. S., Li Zongan, Chen Dehong, Xu Lihai, Zhao Bin (2011). "Development on Molten Salt Electrolytic Methods and Technology for Preparing Rare Earth Metals and Alloys in China." Chinese Journal of Rare Earth **35**(03): 440-450.

Porter, B. and E. A. Brown (1960). Determination of oxide solubility in molten fluorides, Bureau of Mines. Reno Metallurgical Research Center, Nev.

Pshenichny, R. N. and A. A. Omelchuk (2012). "Interaction of rare-earth oxides with binary molten mixtures of zirconium and alkali metal fluorides." Russian Journal of Inorganic Chemistry **57**(1): 115-119.

Sekiya, A. and S. Okamoto (2010). "Evaluation of carbon dioxide equivalent values for greenhouse gases: CEWN as a new indicator replacing GWP." Journal of Fluorine Chemistry **131**(3): 364-368.

Sharma, R. A. (1987). "Neodymium production processes." JOM **39**(2): 33-37.

Shedd, E. S., M. M. Wong, J. D. Marchant and S. United (1970). Electrowinning misch metal from a treated bastnasite concentrate. [Washington, D.C.], U.S. Dept. of the Interior, Bureau of Mines.

Stefanidaki, E., G. M. Photiadis, C. G. Kontoyannis, A. F. Vik and T. Østvold (2002). "Oxide solubility and Raman spectra of NdF₃-LiF-KF-MgF₂-Nd₂O₃ melts." Journal of the Chemical Society, Dalton Transactions(11): 2302-2307.

Tabereaux, A. T. (1994). "Anode effects, PFCs, global warming, and the aluminum industry." JOM **46**(11): 30-34.

Thoma, R. E. (1975). Phase diagrams of binary and ternary fluoride systems. Advances in Molten Salt Chemistry, Springer: 275-455.

Thomas, R. (2013). Practical guide to ICP-MS: a tutorial for beginners, CRC press.

Thonstad, J., S. Rolseth and R. Keller (2016). On the Mechanism Behind Low Voltage PFC Emissions. Light Metals 2013. B. A. Sadler. Cham, Springer International Publishing: 883-885.

USGS (2019). Rare Earths Statistics and Information 2019.

Van Gosen, B. S., P. L. Verplanck and P. Emsbo (2019). Rare earth element mineral deposits in the United States, US Geological Survey.

Zepf, V. (2016). An Overview of the Usefulness and Strategic Value of Rare Earth Metals. Rare Earths Industry: 3-17.

Zhang, L., X. Wang and B. Gong (2018). "Perfluorocarbon emissions from electrolytic reduction of rare earth metals in fluoride/oxide system." Atmospheric Pollution Research **9**(1): 61-65.

ZHENG, X., W.-h. ZHU, G.-h. PENG, J. LIANG and X.-l. ZHANG (2013). "The Electrical Conductivity of NdF₃-LiF-Nd₂O₃ Molten Salt [J]." China Tungsten Industry **1**.